

# Using 3D SPH to Model the Interactions of Rogue Waves and Floating Tethered Bodies

**David Francis Gunn**

**Bachelor of Engineering (Mechanical) (Hons.)  
Bachelor of Science (Mathematics)**

July 2017

*Thesis submitted in fulfillment  
of the requirements for the degree of*

**Doctor of Philosophy**



Supervisor: Prof. Murray Rudman

Associate Supervisor: Dr. Raymond Cohen

Associate Supervisor: Dr. Paul Cleary

# Using 3D SPH to Model the Interactions of Rogue Waves and Floating Tethered Bodies

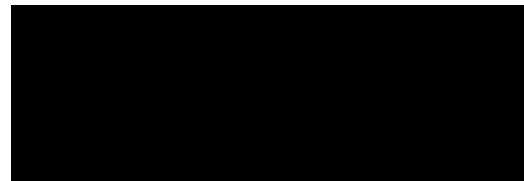
## Copyright Notices

### Notice 1

Under the Copyright Act 1968, this thesis must be used only under the normal conditions of scholarly fair dealing. In particular no results or conclusions should be extracted from it, nor should it be copied or closely paraphrased in whole or in part without written consent of the author. Proper written acknowledgement should be made for any assistance obtained from this thesis.

### Notice 2

I certify that I have made all reasonable efforts to secure copyright permissions for third-party content included in this thesis and have not knowingly added copyright content to my work without the owner's permission.



---

David Francis Gunn

17<sup>th</sup> July, 2017

# Abstract

This research explored the efficacy of using a Smoothed Particle Hydrodynamics (SPH) model as a technique for predicting the motion of a floating tethered body when interacting with a number of wave types, including a rogue wave.

First, a preliminary study established the parameter values required for the SPH model to accurately represent fluid boundaries. This was done by exploring the optimal fluid boundary representations using SPH near a free surface and an object boundary. This was followed by an investigation on the use of a forcing region to generate surface waves.

These preliminary studies were then used to address the following research questions:

- Can SPH accurately model the interaction between surface waves and a floating tethered body, and what is the order of magnitude of the errors?
- How accurately can SPH model a rogue wave?
- What are the physical consequences of a rogue wave impact on a floating tethered body?

The findings of the preliminary studies revealed that an SPH model yielded a high level of agreement between its simulated results with actual experimental measurements, when a sufficient resolution for particle spacing was used.

After confidence in the SPH model was obtained, it was used to model the impact of a large-scale rogue wave on a tethered floating object (in this study, a moored ship). The mass of the ship and the stiffness of the cables were varied to determine what effect these have on the response of the ship to a rogue wave. Pressure sensors were placed on the ship to determine the magnitude of the impact forces at various locations. In additional simulations, it was found that increasing the mass of the ship also increased the risk of green water on the ship's deck. It was also found that the tethering cable's stiffness had little influence in an impact since the tension forces were an order of magnitude smaller than the buoyancy forces. Finally, the wavelength and height of the rogue wave was varied to investigate the effect these had on the moored ship. It was found that the ship could respond adequately to both of these changed conditions without significant green water on the deck. These simulations indicated that SPH modelling is a viable technique for assisting in the design of offshore vessels, with a high level of accuracy.

# Acknowledgments

This thesis would not have been made possible without the help of many people. Firstly, I would like to thank Prof. Murray Rudman and Dr. Raymond Cohen for their guidance and supervision throughout my study. There were countless times that you assisted me with whatever problems I had, both technical and in writing. I would also like to thank Jane Moodie, from the Faculty of Engineering for all of the assistance she has provided me in writing this thesis and other milestone reports throughout my candidature. Additionally, I would also like to acknowledge Dr. Adam Bertran of Splash Editing for the professional assistance he provided in proofreading and editing this thesis.

Secondly, I would like to thank my friends and colleagues, both at Monash University and beyond. In particular, to Jake Tosado for his assistance in the experimental work, without which I am sure would have taken many months longer to accomplish (if at all). Many thanks also to Sam Martin for always providing a welcome distraction from research.

I would also like to thank the Department of Mechanical and Aerospace Engineering, the Faculty of Engineering, and the Commonwealth Scientific and Industrial Research Organisation (CSIRO) for their technical and administrative support given throughout my candidature. Additionally, I would like to thank the Department of Education and Training for the financial support provided as part of the Australian Postgraduate Award given by the Australian Government.

I am indebted to my parents, Iain and Louise, my brother, Tim, and sister, Georgie, for their support and encouragement that they have provided throughout my many years of study.

Finally, I am truly lucky to have met my partner, Yan, during my candidature. Without you the last years of my PhD would have been incredibly stressful and unenjoyable, but you have allowed me to maintain focus and complete my studies. I can only hope that I can support you through your own PhD candidature as much as you have for me. This thesis is dedicated to you.

*David Gunn*

*Department of Mechanical and Aerospace Engineering*

*Monash University*

*17<sup>th</sup> July, 2017*

# Declaration

This thesis contains no material which has been accepted for the award of any other degree or diploma at any university or equivalent institution and that, to the best of my knowledge and belief, this thesis contains no material previously published or written by another person, except where due reference is made in the text of the thesis.



---

David Francis Gunn

17<sup>th</sup> July, 2017

# Contents

<b>Abstract</b>	<b>ii</b>
<b>Acknowledgments</b>	<b>iii</b>
<b>Declaration</b>	<b>iv</b>
<b>Contents</b>	<b>v</b>
<b>List of Figures</b>	<b>viii</b>
<b>List of Tables</b>	<b>xi</b>
<b>1 Introduction</b>	<b>1</b>
<b>2 Literature review</b>	<b>4</b>
2.1 Rogue waves . . . . .	4
2.1.1 Observations of rogue waves . . . . .	5
2.1.2 Theories of generation . . . . .	6
2.1.3 Peregrine breather wave theory . . . . .	7
2.2 Previous studies on the generation and prediction of rogue waves . . . . .	9
2.3 Smoothed Particle Hydrodynamics (SPH) . . . . .	12
2.3.1 Equations of motion for SPH . . . . .	12
2.3.2 Studies of deforming fluid free surfaces using SPH . . . . .	15
2.4 Summary and research questions . . . . .	18
<b>3 Methodology</b>	<b>19</b>
3.1 Experimental equipment . . . . .	20
3.1.1 Monash Wave Tank . . . . .	20
3.1.2 Tethered buoy . . . . .	21
3.1.3 Wave gauges . . . . .	22
3.1.4 Motion capture . . . . .	22
3.2 Smoothed Particle Hydrodynamics method . . . . .	27

3.2.1	Time stepping scheme . . . . .	27
3.2.2	Particle searching optimisation . . . . .	27
3.2.3	Parallelisation . . . . .	28
3.2.4	Boundary model . . . . .	30
3.2.5	Calculating the location of the fluid surface . . . . .	32
3.2.6	Cables in SPH . . . . .	33
<b>4</b>	<b>Using SPH for modelling surface waves</b>	<b>34</b>
4.1	Investigating the boundary and free surface models . . . . .	34
4.1.1	Determining the effect of boundary offset on a partially submerged buoy	35
4.1.2	Determining the effect of boundary offset on a fully submerged buoy .	38
4.1.3	Calculating the free surface location . . . . .	39
4.2	Generating free surface waves using SPH . . . . .	41
4.2.1	Wave generation algorithm . . . . .	42
4.2.2	Determining the particle spacing . . . . .	43
4.2.3	Wave generation calibration . . . . .	44
4.3	Summary . . . . .	48
<b>5</b>	<b>Modelling the interaction between a buoy and a free surface</b>	<b>49</b>
5.1	Oscillatory motion of a spherical buoy . . . . .	50
5.1.1	Vertical oscillation of the buoy . . . . .	50
5.1.2	Horizontal oscillation of the buoy . . . . .	54
5.1.3	Summary . . . . .	55
5.2	Wave Train cases . . . . .	55
5.2.1	Non-dimensionalisation . . . . .	56
5.2.2	Experimental trajectories of the buoy . . . . .	57
5.2.3	Simulated buoy interactions with a wave train . . . . .	59
5.2.4	Cause of the heavy damping . . . . .	66
5.2.5	Stokes wave theory . . . . .	66
5.3	Summary . . . . .	70
<b>6</b>	<b>Modelling Peregrine breather rogue waves with SPH</b>	<b>72</b>
6.1	2D rogue wave simulation . . . . .	72
6.1.1	1 <sup>st</sup> order rogue waves . . . . .	74
6.1.2	2 <sup>nd</sup> order rogue wave . . . . .	79
6.1.3	Summary . . . . .	81
6.2	Ocean Scale Rogue Wave Impacts . . . . .	81
6.2.1	1 <sup>st</sup> order rogue wave impact . . . . .	84
6.2.2	Effect of using a higher cable stiffness . . . . .	90
6.2.3	Effect of additional load . . . . .	90

6.2.4	Coarser resolution . . . . .	93
6.2.5	Increasing the wavelength of the rogue wave . . . . .	95
6.2.6	Simulating the impact of a 2 <sup>nd</sup> order rogue wave . . . . .	97
6.3	Summary . . . . .	100
<b>7</b>	<b>Conclusions</b>	<b>103</b>
<b>A</b>	<b>Motion capture algorithm</b>	<b>107</b>
	<b>References</b>	<b>112</b>

# List of Figures

2.1	Measured wave elevation during the Draupner wave . . . . .	5
2.2	Peregrine breather wave Envelope . . . . .	9
3.1	Schematic of the Wave Tank used . . . . .	20
3.2	The spherical buoy used in the experiments . . . . .	21
3.3	Experimental setup of the buoy at rest . . . . .	22
3.4	Camera views from the four cameras used to record the buoy motion . . . . .	23
3.5	Chessboard Calibration Method . . . . .	24
3.6	Motion Capture Landmarks . . . . .	25
3.7	Motion Capture Markers . . . . .	26
3.8	SPH Cells . . . . .	28
3.9	Speedup of SPH in parallel . . . . .	29
3.10	The boundary normal implementation for modelling boundaries in SPH . . . . .	30
3.11	Boundary particle offsets . . . . .	32
4.1	Effect of $b_{\text{off}}$ on where boundary forces are applied from . . . . .	35
4.2	Partially Submerged buoy . . . . .	36
4.3	The distance of the surface above the sphere centroid ( $\alpha$ ) for the half submerged sphere . . . . .	37
4.4	Radius error of the half submerged buoy compared to the boundary offset . . . . .	38
4.5	Height of the fully submerged buoy above the tank floor, with mean boundary and fluid particle spacings of 10 mm. . . . .	39
4.6	Buoyancy forces on the fully submerged buoy with mean boundary and fluid particle spacings of 10 mm. . . . .	39
4.7	Radius error of the fully submerged buoy compared to the boundary offset. . . . .	40
4.8	The fluid surface compared to the buoy centroid with boundary and particle spacings of 10 mm . . . . .	40
4.9	The effect of the line sensor target value . . . . .	41
4.10	SPH Wave maker schematic . . . . .	42
4.11	Wave train calibration for waves of 1 second period . . . . .	45
4.12	Wave train of 1 second period relative to desired amplitude . . . . .	45

4.13	Wave train calibration for waves of 3 second period . . . . .	46
4.14	Wave train calibration for waves of 7 cm amplitude . . . . .	46
4.15	Wave train calibration for waves of 7 cm amplitude . . . . .	47
4.16	Comparison of waves produced with different forcing factors . . . . .	47
4.17	Comparison of waves produced with different wave maker region lengths . . . . .	48
5.1	The release mechanism for the Vertical Oscillation tests . . . . .	50
5.2	Experimental trajectories of the vertically oscillating buoy . . . . .	51
5.3	Difference of experimental trajectories of the vertically oscillating buoy from the mean trajectory . . . . .	51
5.4	The vertical trajectories of a vertically oscillating buoy. . . . .	52
5.5	A visual comparison of the Vertical Oscillation tests . . . . .	53
5.6	Buoy displacement in the horizontal direction for the horizontal oscillation test.	55
5.7	Wave Train case — Experimental Heave Trajectories . . . . .	57
5.8	Wave Train case — Experimental Surge Trajectories . . . . .	57
5.9	Wave Train case — Surge Trajectories of 1 second period tests . . . . .	58
5.10	Frequency spectra of the 1s wavetrain case with amplitude 5.8 cm . . . . .	60
5.11	Non-dimensionalised heave motion of the buoy in the experiments and simula- tions with a 1 second period wave train. . . . .	61
5.12	Non-dimensionalised surge motion of the buoy in the experiments and simula- tions with a 1 second period wave train. . . . .	62
5.13	Visualisation of the simulated buoy in a 1 s wave train with 10 mm particle spacing	63
5.14	Surge frequency spectrum of the 1 s period simulation . . . . .	64
5.15	Heave frequency spectrum of the 1 s period simulation . . . . .	64
5.16	Non-dimensionalised surge motion of the buoy in the experiments and simula- tions with a 2 second period wave train. . . . .	64
5.17	Non-dimensionalised heave motion of the buoy in the experiments and simula- tions with a 2 second period wave train. . . . .	65
5.18	Non-dimensionalised surge motion of the buoy in the experiments and simula- tions with a 3 second period wave train. . . . .	65
5.19	Non-dimensionalised heave motion of the buoy in the experiments and simula- tions with a 3 second period wave train . . . . .	65
5.20	Regions where different theories of periodic waves apply . . . . .	67
5.21	Surge trajectories in SPH with 2 s period and Stokes generated waves . . . . .	69
5.22	Heave trajectories in SPH with 2 s period and Stokes generated waves . . . . .	69
5.23	Surge trajectories in SPH with 3 s period and Stokes generated waves . . . . .	69
5.24	Heave trajectories in SPH with 3 s period and Stokes generated waves . . . . .	70
6.1	1 <sup>st</sup> order rogue wave 6.24 m from the wave maker . . . . .	75
6.2	1 <sup>st</sup> order rogue wave at various distances from the wave maker . . . . .	76

6.3	1 <sup>st</sup> order rogue wave with refined domain . . . . .	77
6.4	1 <sup>st</sup> order rogue wave using a finer resolution . . . . .	77
6.5	Velocity contours of simulated first order rogue wave . . . . .	78
6.6	2nd Order Rogue Wave 6.24 m from the wave maker . . . . .	79
6.7	2 <sup>nd</sup> order rogue wave at various distances from the wave maker . . . . .	80
6.8	2 <sup>nd</sup> order rogue wave using a finer resolution . . . . .	81
6.9	Arrangement of the three tethering cables on the ship model . . . . .	82
6.10	The domain used for the large scale rogue wave impacts . . . . .	83
6.11	Elevation of the wave heights relative to the still water height . . . . .	83
6.12	The ship in a rogue wave . . . . .	85
6.13	Displacement of the ship in the surge ( $x$ ) and heave ( $y$ ) directions. . . . .	86
6.14	Trajectory of the ship's roll and pitch motions. . . . .	86
6.15	Trajectory of the ship's bow and stern vertical motions, relative to the still water height. . . . .	86
6.16	Locations of the pressure sensors on the ship. . . . .	87
6.17	Pressures at each of the sensor locations . . . . .	88
6.18	Tensions in the ship's cables during a rogue wave impact. . . . .	89
6.19	Cable tensions for the higher stiffness case . . . . .	91
6.20	Buoyancy forces on the ship during a rogue wave impact. . . . .	91
6.21	Heave and surge motion of the heavier ships during the rogue wave impact. . .	92
6.22	Pressure at point 1 (top of the bow) on the heavier ships during a rogue wave. .	93
6.23	Surface elevation of the rogue wave with a mean particle spacing of 2 m. . . . .	94
6.24	Surge trajectory of the ship in a rogue wave with a mean particle spacing of 2 m.	94
6.25	Buoyancy forces on the ship during a rogue wave impact . . . . .	95
6.26	Comparison of pressures at sensor 3 for the 1 m and 2 m particle spacing cases.	95
6.27	Surface elevation of a rogue wave with a longer wavelength. . . . .	96
6.28	Trajectory of the ship in response to the longer wavelength rogue wave impact .	97
6.29	Pressure at sensor 3 during the longer wavelength rogue wave. . . . .	97
6.30	Surface elevation of the simulated first and second order rogue waves. . . . .	98
6.31	Visualisation of the ship responding to a second order rogue wave. . . . .	99
6.32	Trajectory of the ship in response to the second order rogue wave impact . . . .	100
6.33	Tension of the side cables during the second order rogue wave impact . . . . .	100
6.34	Pressure at sensor 3 during the second order rogue wave impact . . . . .	101

# List of Tables

5.1	Wave maker lengths used . . . . .	60
5.2	1st and 2nd order velocity terms in the Stokes waves . . . . .	68
6.1	Properties of the rogue waves generated in experiments . . . . .	73
6.2	Locations of the pressure sensors . . . . .	87

# Chapter 1

## Introduction

Extreme ocean conditions pose significant risk to manmade offshore structures. In the Gulf of Mexico, approximately 10 tropical storms occur each year (Landsea, 2013), subjecting the many offshore vessels, platforms and other structures to extreme weather events, placing them at severe risk of damage. During the year of September 2004 to September 2005, 126 offshore structures were destroyed and another 183 were severely damaged during the hurricanes Ivan, Katrina and Rita (Kaiser et al., 2009).

During these tropical storms, extremely large waves, called rogue waves (or freak or extreme waves) can form. These waves can exert considerable loads on offshore structures, causing significant damage. However, these rogue waves are not limited to tropical storms and can seemingly appear in any weather conditions.

One such rogue wave occurred on February 14, 1982, and impacted the semi-submersible *Ocean Ranger*. The vessel was drilling in the Hibernia Field (about 166 miles east of Newfoundland, Canada) when a storm linked to a major Atlantic hurricane approached. During the stormy conditions, a rogue wave developed and impacted the vessel, causing severe damage and flooding that ultimately led to the vessel's capsize and loss of all 84 crew members (Kjeldsen, 1997).

More recently, an offshore drilling rig in the North Sea was damaged when a rogue wave hit it in December 2015, leaving one person dead and two more injured (Fouche and Adomaitis, 2015). These incidents are just some of the many examples that highlight the need for thorough and accurate design processes when building offshore structures - to ensure the safety of the people on-board and to avoid costly economic implications.

Offshore structure design is, therefore, complex. Designers need to ensure that the vessel can perform its primary function as well as being capable of surviving extreme conditions. However, the response of the structure to extreme conditions cannot be predicted by simple models. This leaves the designer either over engineering the vessel or using sophisticated computational

methods to do such modelling.

Wave impacts have traditionally been analysed by conducting experiments that use scaled models. This process involves manufacturing a scale prototype of a structure and testing it in a wave-making facility to ensure that its design will survive conditions representative of those it would face in the ocean. Provided that the correct scaling was accurate for the key parameters (particularly the Froude number), the experimental analysis provided a good representation of the design's ability to withstand ocean conditions in the actual structure.

The traditional experimental procedure involves a number of design iterations by building scale prototypes and testing each one. These iterations optimise the design and prevents the structure from being over-engineered, and thus more costly to build. However, after a number of iterations the financial and time cost of additional prototypes can outweigh the savings the improved design offers. Consequently, a small number of iterations is preferred.

The complementary approach to experimental methodology is to use Computational Fluid Dynamics (CFD) simulations. This can predict loadings that can be then used in Finite Element Analysis (FEA) software. With computational power rapidly improving and becoming cheaper each year, simulations are becoming more viable as a design technique. Simulations enable designers to test many iterations without the need for expensive prototype construction. They also avoid the need for intrusive measurement equipment, and measurements can be made anywhere on the model. A simulation tool capable of modelling rogue wave impacts on a floating vessel, therefore, would be a valuable asset to offshore structure designers.

However, the non-linear nature and potential for wave-breaking, render simple computational techniques that model surface elevation, such as the Shallow Wave equations, inadequate. Thus a method that fully models the fluid domain is required. The problem is further complicated by the interaction of the free surface with a free moving dynamic object. The modelling technique needs to be able to handle these complex fluid boundary deformations as the waves impact on the floating object.

Many traditional computational methods rely on representing the fluid domain with a mesh (commonly called mesh-based models); however, the generation of the mesh is computationally expensive, so it is not well suited to constantly deforming domains. Consequently, methods that are capable of modelling deforming domains without the need for traditional mesh computations are ideal. The Smoothed Particle Hydrodynamics (SPH) technique is capable of modelling these scenarios.

One of the strengths of the SPH model is the natural modelling of fluid boundaries. The technique has been utilised for modelling dam-breaking problems (Cummins et al., 2012), sloshing problems (Souto-Iglesias et al., 2006), breaking surface waves (Khayyer et al., 2008, 2009), and many others (Doring et al., 2004; Bouscasse et al., 2013; Bašić et al., 2014). This is due to its

meshless Lagrangian formulation that inherently models the fluid boundaries without the need for any special treatment or remeshing (which a traditional mesh-based model would require). However, the use of SPH to model rogue waves is limited to a small number of studies and each has its limitations.

Campbell and Vignjevic (2012) modelled a large wave interaction with a floating buoy, but their simulations did not agree with the experimental results. Rudman and Cleary (2013) modelled a large wave, which they described as a rogue wave, that impacted on a Tension-Leg Platform; however, their method of generating the wave was unrealistic.

Presently, it is unknown how well SPH is able to accurately model a rogue wave impact on a floating vessel. Additionally, there is substantial debate in the oceanography community about how rogue waves are generated, and many theories have been proposed (Laird, 2006). One theory claims “that rogue waves could be related to [solutions] of the underlying evolution equations” (Chabchoub et al., 2011, p. 1), which can be modelled by the Non-Linear Schrödinger equations (NLS). These equations have successfully been used to experimentally model rogue waves (Karjanto and Van Groesen, 2010; Chabchoub et al., 2012a, b). The NLS equations model the surface elevation of the sea state so they cannot be directly used to model the impact of the wave on a vessel. However, they can be coupled with the SPH model to model the generation of a representative rogue wave that then impacts the vessel.

This thesis describes a sequence of studies aimed at verifying the use of SPH in modelling both wave interactions with a floating tethered object, as well as the modelling of a rogue wave and its impact on a floating tethered object. A review of the current literature in wave models (particularly rogue waves), numerical studies of wave impacts, and of SPH will demonstrate the need for validation of the SPH model in modelling rogue wave impacts. Physical experiments performed in the Monash University Wave Tank will be used to provide data of two cases: wave interactions with a floating tethered body, and the generation of rogue waves using the NLS to describe the generation mechanism. The data from these experimental cases will then be used to determine the capabilities and requirements for SPH to accurately model these cases. The SPH model will be used to model a tethered vessel when it is impacted by a rogue wave, again described by the NLS, under a number of different design conditions. The results of these simulations will answer the question of how well the SPH model is able to model rogue wave impacts on a floating vessel. They will also provide guidance on the conditions and parameters required to ensure that the results of the simulations are valid.

# Chapter 2

## Literature review

### 2.1 Rogue waves

Rogue waves, also known as extreme or freak waves, are giant ocean waves that often occur unexpectedly and have been observed in water of any depth. In contrast to tsunamis, where the generation mechanism is well understood (Haugen et al., 2005), oceanographers are uncertain as to how rogue waves are formed. Rogue waves are non-linear in nature, and often break, making analysis of their generation and their effects difficult to assess in a purely theoretical manner. They are therefore typically analysed using small-scale experimental work or by numerical simulations.

Different definitions of rogue waves have been used in a number of studies; however, it is generally considered that the ratio between the rogue wave height ( $H$ ), measured from peak to trough, and the significant wave height ( $H_s$ ),  $H' = H/H_s$ , should be greater than a specific value. In a particular sea state, the significant wave height was defined as the mean wave height of the largest third of waves (with individual wave heights measured from crest to trough). However, there is little agreement in the literature of what value of  $H'$  constitutes a rogue wave. Faulkner (2000) suggested that a rogue wave should be defined by having  $H' \geq 2.4$ , while Clauss (2002) used  $H' \geq 2$  as their definition. Wolfram et al. (2000) defined rogue waves as having  $H' \geq 2.3$  but also added the condition that a rogue wave should be 50% steeper than the significant steepness of the sea state (defined similarly to the significant wave height). The value of steepness used in Wolfram et al. (2000) was defined as the gradient of the wave face. Recently, however, the wave crest criteria,  $H_{crest} > 1.3H_s$ , has become the favoured definition in the rogue wave community (Fernandez et al., 2016).

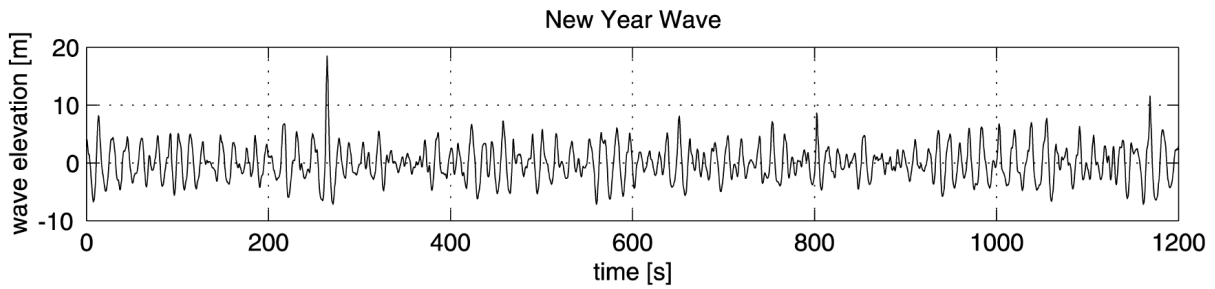


Figure 2.1: Measured wave elevation during the Draupner (or New Year wave) wave, seen at approximately 260 seconds. Reprinted from Clauss (2002), with permission from Elsevier.

### 2.1.1 Observations of rogue waves

Draper (1964, 1971) provided accounts of a number of rogue wave observations by sailors. One such account was the *Weather Reporter* that recorded a wave on September 12, 1961, which exceeded the measurement capabilities of 60 ft (18.3 m). The wave was later (conservatively) estimated to measure 67 ft (20.4 m) from crest to trough.

Faulkner and Buckley (1997) described substantial damage to the liners *RMS Queen Mary* and *RMS Queen Elizabeth* caused by rogue waves in 1942 and 1943 respectively. While transporting United States troops from New York to Great Britain, *RMS Queen Mary* was on the brink of capsizing after it reportedly encountered a steep rogue wave in the north east Atlantic. *RMS Queen Elizabeth* was hit by a breaking rogue wave after it had dipped in the trough that preceded this wave, and was then hit by a second wave. The impact broke the bridge windows that was 90 ft (27.5 m) above the normal water level and caused significant damage to the foredeck. While these waves were not measured, and cannot be confirmed to be rogue waves, their heights were greatly beyond those expected to be encountered, even in stormy conditions.

In 1982, a rogue wave in rough seas struck the semi-submersible *Ocean Ranger* (Kjeldsen, 1997). The rogue wave damaged a portlight and flooded the ballast control room, which was located 8.5 metres above the mean sea level. With the portlight compromised, the subsequent waves were able to cause further flooding to the control room, leading to the eventual sinking of the vessel.

It was not until January 1, 1995, that a rogue wave was detected by a measuring instrument for the first time, with a wave height of almost 26 metres (Haver and Andersen, 2000). This rogue wave impacted the Draupner platform in the North Sea off the coast of Norway, causing substantial damage to the platform. The wave has since come to be known as the Draupner wave or New Year wave. The wave elevation record is shown in Figure 2.1, with the rogue wave event occurring at approximately 260 seconds.

In December 2000, the European Union launched the MaxWAVE project to investigate ship and platform accidents due to severe weather conditions, and to suggest improved design and safety

measures. Rosenthal and Lehner (2005) and Lehner and Rosenthal (2006) stated, on pages 2 and 754 respectively, that “the main tasks performed within the project were

- to confirm the existence of rogue waves and their risk of an encounter. Existing measurements and hindcast modelling were used to better understand the shape and impacts of extreme waves during ship/offshore accidents. Modern measurement techniques were employed to recognise extreme individual waves and their regional probability of occurrence;
- to implement the improved knowledge of freak waves to modern ship design, by involving the two marine communities of marine design and oceanography;
- to develop forecast criteria for rogue waves with the aid of physical, mathematical, statistical and deterministic wave model tests and by that, to improve security for human life;
- to disseminate and exploit the project results by the project members, covering the marine design/operation side, the wave science community, system providers and certifying institutions.”

The project utilised data from the European Space Agency’s satellites, and identified more than ten individual rogue waves in a three week period. This result not only confirmed the existence of rogue waves, but also indicated that rogue waves occurred more often than previously thought. However, neither paper by Lehner and Rosenthal discussed the results in terms of the other goals of the project. Instead they stated that a large step had been taken by the MaxWAVE project in developing a warning criterion against rogue waves for offshore structures (Rosenthal and Lehner, 2005).

### **2.1.2 Theories of generation**

In order to effectively model rogue waves, either experimentally or numerically, an understanding of the generation mechanism is necessary to ensure that accurate models are developed. Laird (2006) outlined three theories of rogue wave generation:

1. constructive interference in a linear superposition of many small waves;
2. the interaction between strong current and an opposing wind field; and,
3. current focusing.

At the time of Laird’s thesis, most attention had been given to the current focusing theory that was first suggested by Peregrine (1976). White and Fornberg (1998) summarised this theory as “in areas of strong current, such as the Agulhas, abnormally large waves could be produced when wave action is concentrated by refraction into a caustic region” (p. 113). That is, the

refraction of waves over a long distance can result in local focusing of wave energy to create a giant peak or trough. White and Fornberg (1998) showed that the theory accurately described the distribution of focus points. This demonstrated that the theory could be used to explain the formation of rogue waves in regions of strong current.

In other regions where strong currents did not occur, linear superposition was the most widely accepted theory. Theoretical techniques for predicting wave amplitudes, particularly rogue waves, from superposition are discussed in Baldock et al. (1996), Kharif and Pelinovsky (2003) (2003), and Kharif et al. (2009). However, non-linearities or breaking were known to influence the actual amplitudes, and this caused them to differ from those predicted by linear superposition.

Another theory, suggested by Henderson et al. (1999), was that the excitation of breather-like solutions of the NLS could trigger the formation of rogue waves. This theory was supported by several studies (Osborne et al., 2000; Calini and Schober, 2002; Karjanto, 2006; Schober, 2006) and has become a commonly proposed mechanism for rogue wave generation.

The Peregrine breather solutions (Peregrine, 1983; Akhmedieva et al., 1985) to the NLS have been used experimentally to model rogue waves. Karjanto and Van Groesen (2010); Chabchoub et al. (2011); Onorato et al. (2013a) all found that the resulting rogue waves closely resembled the measurements in the real ocean. However, modulation instability (the underlying generation mechanism modelled by the breather solution of the NLS (Benjamin and Feir, 1967)), has been shown not to be relevant for real ocean rogue waves (Fedele et al., 2016). Despite this, the Peregrine breather wave theory remains a satisfactory model because the rogue waves produced are representative of real rogue waves (Onorato et al., 2013a). Since this study will be concerned with modelling rogue waves, rather than the fundamental generation mechanisms, the Peregrine breather wave theory is used with confidence that the model waves produced are representative of actual rogue waves.

### 2.1.3 Peregrine breather wave theory

The NLS are a non-linear variant of the Schrödinger equation for describing classical and quantum mechanics. Unlike the original Schrödinger equation, they do not describe quantum states. Peregrine (1983) presented explicit solutions for the NLS, concluding that they provided accurate representations of wave groups, and could produce rogue waves with  $H'$  and  $H_{crest}$  values as large as 3 and 1.5 respectively, satisfying both rogue wave conditions described in Section 2.1.

To describe the evolution of a rogue wave, the NLS (Zakharov, 1968) can be written as

$$i \left( \frac{\partial a}{\partial t} + \frac{\omega_0}{2k_0} \frac{\partial a}{\partial x} \right) - \frac{\omega_0}{8k_0^2} \frac{\partial^2 a}{\partial x^2} - \frac{\omega_0 k_0^2}{2} |a|^2 a = 0 \quad (2.1)$$

where  $\omega_0$  and  $k_0$  denote the angular frequency and wave number of the carrier wave respectively,  $i = \sqrt{-1}$ , and  $a$  is the mean-to-peak amplitude. Often it is more convenient to use the dimensionless form of the NLS:

$$i\psi_T + \psi_{XX} + 2|\psi|^2\psi = 0 \quad (2.2)$$

which is obtained from Eq. (2.1) by rescaling the variables:

$$T = -|\psi_0|^2 \frac{\omega_0}{8} t, \quad X = \left(xk_0 - \frac{\omega}{2}t\right) |\psi_0|, \quad \psi_0 = \sqrt{2}k_0a_0 \quad (2.3)$$

Using these rescaled variables, Eq. (2.2) can be solved to give a class of solutions that satisfy the conditions for a rogue wave. The  $j$ th order solution, also known as the  $j$ th Akhmediev-Peregrine solution, is written in the general form

$$\psi_j(X, T) = a_0 \left[ (-1)^j + \frac{G_j + iH_j}{D_j} \right] e^{2iT} \quad (2.4)$$

where  $G_j$ ,  $H_j$ , and  $D_j$  are polynomials of  $X$  and  $T$ . The function  $\psi_j$  describes the amplitude and phase dynamics of the rogue wave and the amplitude amplification of the rogue wave is  $2j + 1$ . For  $j = 1$  the polynomials are (Peregrine, 1983)

$$G_1(X, T) = 4, \quad H_1 = 16T, \quad D = 1 + 4X^2 + 16T^2 \quad (2.5)$$

and for  $j = 2$  they are (Akhmedieva et al., 1985)

$$G_2(X, T) = 3/4 - (X^2 + 4T^2 + 0.75)(X^2 + 20T^2 + 3/4) \quad (2.6a)$$

$$H_2(X, T) = 2T \left( 3X^2 - 4T^2 - 2(X^2 + 4T^2)^2 - 15/8 \right) \quad (2.6b)$$

$$D_2(X, T) = \frac{(X^2 + 4T^2)^3}{3} + \frac{(X^2 - 12T^2)^2}{4} + \frac{3(12X + 176T^2 + 1)}{64} \quad (2.6c)$$

These solutions generate a rogue wave that has maximum amplitude at  $x = 0$  when  $t = 0$ . The surface elevation  $\eta$  is given by:

$$\eta(x, t) = \text{Real} \left\{ \psi_j e^{i(k_0x - \omega_0t)} \right\} \quad (2.7)$$

The complex phase dynamics of  $\psi_j$  results in a phase shift in  $\eta$ . In practice, this causes the wave envelope to grow at  $X = 0$ , borrowing energy from the surrounding waves, until the peak rogue wave occurs at  $T = 0$ . After which, the extra energy is dispersed back to the surrounding waves. This is shown in Figure 2.2. The shape of the wave envelope over time appears to “breathe in” to form the rogue wave, and then “breathe out” after the rogue wave, giving rise to the “breather wave” name.

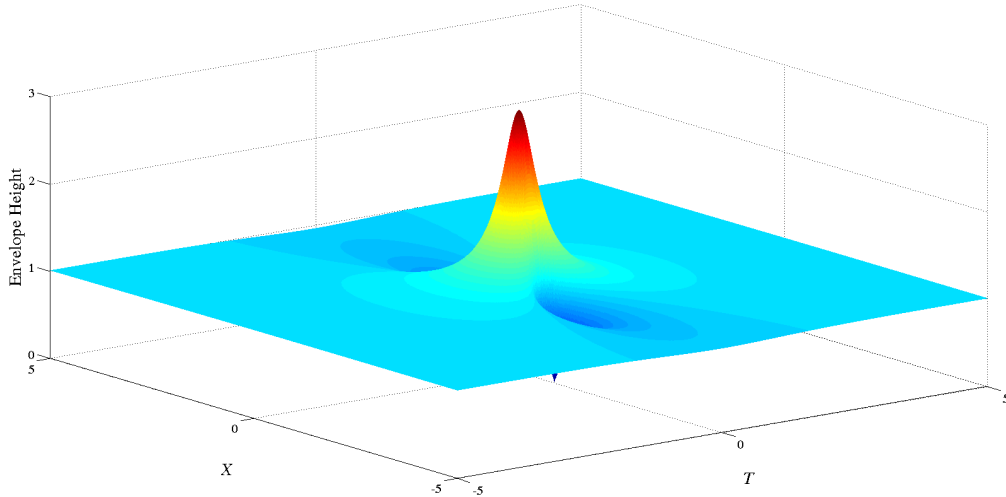


Figure 2.2: The envelope for a Peregrine breather wave of first order.

## 2.2 Previous studies on the generation and prediction of rogue waves

Rogue waves have been studied using physical experiments, as well as with numerical simulations. A number of experimental studies in which rogue waves were generated have been performed by Clauss and colleagues, who used a wave maker-feedback system to generate rogue waves in their wave tanks (Clauss, 2002; Clauss et al., 2003; Clauss and Schmittner, 2007; Fonseca et al., 2010). They used two wave tanks to perform their experiments: a small wave tank (15 m length, 0.3m width, 0.4 m water depth) with a paddle wave maker, and a large wave tank (80 m length, 4 m width, 1.5 m depth) with a piston type wave maker. They were able to demonstrate that a rogue wave could be generated using the wave superposition technique. The wave could then be used to experimentally analyse the interaction of a rogue wave on a scale model (Clauss, 2002). This experimental technique was able to generate data for the interactions of a rogue wave with a floating production, storage and offloading (FPSO) unit (Fonseca et al., 2010). Fonseca et al. (2010) found that the interaction could be numerically modelled with an adequate degree of accuracy using an unspecified in-house code.

The NLS have been used to experimentally model a number of Peregrine-type breather rogue waves, initially observed in the field of optics (Kibler et al., 2010), and then for surface waves (Chabchoub et al., 2011, 2012a, b, 2015). In Chabchoub et al. (2011), a first order Peregrine breather wave was observed – this had previously only been observed in optical fibres and not in surface waves. Their 2012b paper reported on experimentally modelled Peregrine waves up to the fifth order, where the rogue wave height was eleven times larger than the wave height of the carrier wave. Perić et al. (2015) also used the NLS method to model breaking first

order Peregrine waves (the critical steepness factor of 0.15 was exceeded in these cases). They compared these to simulations using a 2D Volume of Fluid (VOF) method. The simulation and experimental results agreed remarkably well, but they reported that the simulations took 4 weeks to complete when running parallel on a 16 core cluster.

The experimental setup of Clauss (2002) was used to generate Peregrine breather type rogue waves by Onorato et al. (2013a). In their experiments, they subjected a scale model of a chemical tanker to a first order Peregrine wave in a sea state equivalent to 10 m wave heights and a rogue wave of nearly 30 metres. The results provided valuable insight into the impact of a rogue wave on a ship. Furthermore, they showed that using NLS breather solitons was an appropriate method for studying the impact of a rogue wave. Numerical simulations of Peregrine breather waves were also performed by Ten and Tomita (2006), who used a Boundary Element Method to model the waves in a numerical wave tank with a high degree of accuracy. They then used the numerical method to study the interaction between the breather waves and random waves, comparing it to the interaction between a soliton and random waves. They concluded that the interaction of the breathers and random waves produced some rogue waves, while the solitons passed through the irregular waves with minimal effect on the soliton envelope profile.

Rogue waves were also generated in a numerical wave tank using a focused wave approach by Fochesato et al. (2007). They used a 3D fully non-linear potential flow model (Brandini and Grilli, 2001; Grilli et al., 2001) that was based on a high-order boundary element method. Unlike Higher Order Spectral (HOS) or Boussinesq models, their model did not break down when the wave overturned. A snake piston wave maker was used to create waves along the piston that would focus at a point to create a single large focused wave. In their study, a comparison with Stokes waves of identical height and wavelength was performed. It was found that the Stokes wave predictions of wave kinematics were less accurate than their method. As Stokes waves were often used to predict rogue waves in the offshore industry, these findings may lead to more accurate methods being adopted and thus improving the design procedures of offshore structures (Corte and Grilli, 2006).

Rogue wave kinematics can also be modelled using a double Fourier series solution, as was shown by Smith and Swan (2002). The method was proposed by Baldock and Swan (1994) and was used by Smith and Swan to model rogue waves, which were then compared to laboratory data. Their findings showed that the method was able to accurately model rogue waves. They then compared the double Fourier series method to a number of known solutions, including Stokes 5<sup>th</sup> order solutions and linear random wave theory, finding the method provided more accurate predictions of wave kinematics. Using the method, they established that the nonlinear wave-wave interactions were important, and that the waves were highly dependent on the depth.

The HOS technique, originally proposed by West et al. (1987) and Dommermuth and Yue (1987), was also used by Ducroz et al. (2007) to predict the grouping of rogue waves in

a sea state. They were able to numerically produce a large number of 2D rogue waves. They found that certain locations were subjected to multiple rogue wave events while others observed few or no rogue waves. While the method is promising for developing a generation theory for rogue waves, it is less practical for modelling an object floating on the surface, as the object will disrupt the potential function used.

Schellin et al. (2011) showed that a Reynolds-Averaged Navier-Stokes based numerical model could be used for analysing rogue waves, particularly in load analysis. They used an undisclosed mesh-based CFD technique (which solved the Reynolds-Averaged Navier-Stokes equations) to simulate a rogue wave impacting on a Jack-Up platform. They found that the technique predicted overturning moments when the platform was subject to critical wave impact loads. Their results were verified against the experimental studies reported by El Moctar et al. (2004) and Schellin and El Moctar (2007). The method was reported to achieve accurate predictions of wave loads from a rogue wave, and in very reasonable time frames. However, it should be noted that the Jack-Up platform model was assumed to remain rigid, since pillars attached it to the ocean floor, so there was no domain deformation. For a floating platform that is able to move, the method may not be appropriate and may require significant modifications.

Westphalen et al. (2012) investigated the stability of two numerical techniques for modelling rogue waves: a finite volume method and a control volume finite element method. They studied the capabilities of each technique in modelling wave-wave interactions, and wave interactions with a horizontal or vertical cylinder, comparing the model projections to experimental measurements in each case. Both numerical methods were able to accurately model the surface elevations of the waves, as well as the forces on the cylinders. The researchers drew no conclusions about which method was superior; rather they stated that the methods were powerful tools for design, especially when run in parallel, and were able to predict highly non-linear wave interactions.

Zhao and Hu (2012) and Zhao et al. (2014) developed a 2D Constrained Interpolation Profile (CIP)-based method for modelling a rogue wave impact on a floating structure, and experimentally validated their code. In the experiments, they observed an inverted T-shaped object with 3 degrees of freedom under the impact of a rogue wave. They replicated the experiment numerically in 2D, finding that the CIP-based method was able to model the impact with reasonable accuracy.

Birkholz et al. (2015) sought to study the predictability of rogue wave events to determine if an advanced warning model could be developed. They analysed time series data for a number of observed rogue wave events in optics, and in the ocean. Firstly, they looked at the spatial profile of a laser beam reported by Birkholz et al. (2013) and then a rogue wave measured at the output of a fiber supercontinuum (Solli et al., 2012). Finally, they analysed surface height recordings by the Draupner oil platform on January 1 and January 19 in 1995 (Haver and Karunakaran,

1998; Haver, 2004). They found “the predictability of rogue waves is [limited] and may only suffice for last-second warnings” (p. 4).

The studies discussed here highlight that generating a rogue wave for analysis purposes is within the capabilities of researchers. However, the impact of a rogue wave on a floating object has only been performed experimentally, or in 2D simulations. To study these rogue wave impacts numerically, the numerical techniques presented here need to be improved, or an alternative modelling technique needs to be developed.

A number of numerical studies of rogue waves have been performed; however, modelling a deforming boundary, such as a breaking free surface or when an object moves through the domain, is still a challenging problem that occurs when studying rogue wave impacts. One method that is able to model the wave and boundary interactions is Smoothed Particle Hydrodynamics (SPH).

## 2.3 Smoothed Particle Hydrodynamics (SPH)

SPH is a meshless Lagrangian method that models problems using moving interpolation points, called particles. These particles are able to move separately from each other so they can be used to naturally model complex boundary deformations. The method was first proposed by Gingold and Monaghan (1977) for modelling astrophysical problems. Monaghan (1994) then adapted SPH for use in fluid dynamics studies. An overview of this method is presented here.

### 2.3.1 Equations of motion for SPH

The formulation of SPH (Monaghan, 2005; Cummins et al., 2012) begins with the Dirac delta identity:

$$f(\mathbf{r}) = \int_{\Omega} f(\mathbf{r}') \delta(\mathbf{r} - \mathbf{r}') d\mathbf{r}' \quad (2.8)$$

where  $f(\mathbf{r})$  is a function of the position vector  $\mathbf{r}$ , and  $\delta(\mathbf{r} - \mathbf{r}')$  is the Dirac delta function. If the function  $f$  represents a property of the fluid, then this identity can be used to interpolate a continuous fluid from the particles. However, since SPH is a discrete method, this identity cannot be used for such a purpose. Replacing  $\delta$  with a smoothing function approximation,  $W(\mathbf{r} - \mathbf{r}', h)$ , where  $h$  is the support dimension, or smoothing length, then Eq. (2.8) becomes:

$$f(\mathbf{r}) \approx \int_{\Omega} f(\mathbf{r}') W(\mathbf{r} - \mathbf{r}', h) d\mathbf{r}' \quad (2.9)$$

The function  $W$  is usually chosen to be an even function and it is required to satisfy a number of conditions: the unity condition, the Delta function property, and the compact condition. These

conditions are expressed as:

$$\int_{\Omega} W(\mathbf{r} - \mathbf{r}') d\mathbf{r}' = 1 \quad (2.10a)$$

$$\lim_{h \rightarrow 0} W(\mathbf{r} - \mathbf{r}', h) = \delta(\mathbf{r} - \mathbf{r}') \quad (2.10b)$$

$$W(\mathbf{r} - \mathbf{r}', h) = 0 \text{ when } |\mathbf{r} - \mathbf{r}'| > 2h \quad (2.10c)$$

A problem arises with Eq. (2.9) in that it requires the property function  $f$  to be known over the entire support region of  $W$  (where  $W$  is non-zero). Since SPH uses particles to represent the fluid, the function  $f$  is known only at the discrete particle locations. If the sub-domain around a particle  $j$  (denoted  $\Omega_j$ ) is considered, the function  $f(\mathbf{r}')$  and  $W(\mathbf{r} - \mathbf{r}', h)$  can be replaced by  $f_j = f(\mathbf{r}_j)$  and  $W(\mathbf{r} - \mathbf{r}_j, h)$  over the entire sub-domain. If this is done for the sub-domains around all of the particles then Eq. (2.9) becomes

$$\begin{aligned} f(\mathbf{r}) &\approx \sum_j \int_{\Omega_j} f_j W(\mathbf{r} - \mathbf{r}_j, h) d\mathbf{r}' \\ &= \sum_j f_j W(\mathbf{r} - \mathbf{r}_j, h) \int_{\Omega_j} d\mathbf{r}' \\ &= \sum_j V_j f_j W(\mathbf{r} - \mathbf{r}_j, h) \end{aligned} \quad (2.11)$$

where  $V_j$  is the volume represented by particle  $j$ . The volume is calculated from the mass and density,  $V_j = m_j/\rho_j$ , giving the value of the property function as

$$f(\mathbf{r}) = \sum_j \frac{m_j}{\rho_j} f_j W(\mathbf{r} - \mathbf{r}_j, h) \quad (2.12)$$

Note that the approximation notation has been dropped in Eq. (2.12). The gradient of the property  $f$  can be approximated by taking the gradient of Eq. (2.12), yielding:

$$\nabla f(\mathbf{r}) = \sum_j \frac{m_j}{\rho_j} f_j \nabla W(\mathbf{r} - \mathbf{r}_j, h) \quad (2.13)$$

A number of kernels are available, but in this project the Wendland (1995) kernel will be used. Preliminary simulations using other kernels showed that ‘‘particle clumping’’ occasionally occurred where two particles would move close together (within  $0.5\delta x$ ) and remain close for long periods of time. It has been reported that the Wendland kernel eliminates this particle clumping (Capone et al., 2007; Robinson, 2009). The Wendland kernel is defined as:

$$W(\mathbf{r} - \mathbf{r}', h) = \frac{7}{85.336\pi h^3} \begin{cases} \left(2 - \frac{r}{h}\right)^4 \left(1 + \frac{2r}{h}\right) & \frac{r}{h} \leq 2 \\ 0 & \frac{r}{h} > 2 \end{cases} \quad (2.14)$$

where  $r = |\mathbf{r} - \mathbf{r}'|$ ,  $h = h_f \delta x$ ,  $\delta x$  is the mean particle separation, and  $h_f = 1.2$  is used in this study based on the results of Cummins et al. (2012).

In a fluid free surface, a density discontinuity exists at the free surface in reality. However, using Eq. (2.12) to update the density of a particle in the simulations would lead to a smoothed density that drops from the fluid density to zero across the interface. To avoid this, Monaghan (1994) instead used a mass continuity equation (written in SPH as Eq. (2.15c)) in the equations of motion:

$$\frac{d\mathbf{r}_i}{dt} = (1 - \epsilon)\mathbf{v}_i + \epsilon \sum_j \frac{m_j}{\rho_j} \mathbf{v}_j W(\mathbf{r}_i - \mathbf{r}_j, h) \quad (2.15a)$$

$$\frac{d\mathbf{v}_i}{dt} = \mathbf{F}_i - \sum_j m_j \left( \frac{P_i}{\rho_i^2} + \frac{P_j}{\rho_j^2} + \Pi_{ij} \right) \nabla W(\mathbf{r}_i - \mathbf{r}_j, h) \quad (2.15b)$$

$$\frac{d\rho_i}{dt} = \sum_j m_j (\mathbf{v}_i - \mathbf{v}_j) \cdot \nabla W(\mathbf{r}_i - \mathbf{r}_j, h) \quad (2.15c)$$

where  $0 \leq \epsilon \leq 1$  is the XSPH term introduced by Monaghan (1992). This keeps the particles orderly in the absence of viscosity and is chosen as 0.5 in this research.  $\mathbf{F}_i$  is the sum of the external forces on particle  $i$ ,  $P_i$  is the pressure of particle  $i$ , and  $\Pi_{ij}$  is the viscous term given by

$$\Pi_{ij} = \frac{\xi}{\rho_i \rho_j} \cdot \frac{4\mu_i \mu_j}{\mu_i + \mu_j} \cdot \frac{(\mathbf{v}_i - \mathbf{v}_j) \cdot (\mathbf{r}_i - \mathbf{r}_j)}{|\mathbf{r}_i - \mathbf{r}_j|^2 + \beta^2} \quad (2.16)$$

where  $\xi = 5.75$  for the Wendland kernel, and  $\beta$  is a small parameter that ensures singularities are avoided when  $|\mathbf{r}_i - \mathbf{r}_j| = 0$  (typically  $\beta = 0.01\delta x$ ). The pressure terms ( $P_i$  and  $P_j$ ) in Eq. (2.15b) are given by the weakly compressible equation of state:

$$P_i = P_0 \left[ \left( \frac{\rho_i}{\rho_0} \right)^\gamma - 1 \right] \quad (2.17)$$

where  $\gamma$  is chosen to equal 7 (Cleary, 1998),  $\rho_0$  is the reference density (chosen as 1000 kg/m<sup>3</sup> for water), and  $P_0$  is the overall dynamic pressure scale given by

$$\frac{\gamma P_0}{\rho_0} = c_s^2 \quad (2.18)$$

where  $c_s$  is the speed of sound. The value of the speed of sound also influences the time step by

$$\delta t = \frac{\text{CFL} \cdot h}{c_s + \frac{2\varepsilon\mu}{h\rho}} \quad (2.19)$$

where CFL is the Courant-Friedrichs-Lewy condition, chosen to be 0.5 (Cummins et al., 2012). The speed of sound in Eq. (2.18) is chosen to be at least ten times larger than the maximum characteristic speed in the simulation, ensuring that the relative density fluctuations are small ( $< 1\%$ ) and the fluid is close to incompressible (Monaghan, 1994).

### **2.3.2 Studies of deforming fluid free surfaces using SPH**

The SPH technique has been used by a number of researchers for analysing wave motions. For example, Lo and Shao (2002) simulated a solitary wave running up onto a shoreline using the SPH technique, coupled with a turbulence model based on the Smagorinsky (1963) eddy viscosity. They reported adequate results prior to wave break, though they stated that the turbulence model required further improvements.

SPH has also been used to simulate fluid-structure interactions by Doring et al. (2004) and Oger et al. (2006), who performed a number of water entry simulations of various shapes. Their simulations gave good agreement with experimental results and they concluded that SPH was able to satisfactorily model their water entry tests. The technique has also been used for modelling sloshing inside a tank (Souto-Iglesias et al., 2006), as well as dam-break impacts (Cummins et al., 2012). All of these studies demonstrate the ability of SPH to model complex free surface profiles, even when the wave or surface is interacting with an obstacle or moving body.

The Monaghan method is also referred to as the “Weakly Compressible SPH” method since small variations in the fluid density are permitted. A fully incompressible version of the SPH method, called Incompressible SPH (ISPH), was proposed by Cummins and Rudman (1999). They found that the ISPH method modelled incompressible flows more accurately and efficiently than the SPH method. However, they found error accumulation in the density field due to the angular momentum not being conserved, which limited the viability of their version of the ISPH method.

Despite this, the ISPH method was used by Khayyer et al. (2008) to model the water surface in breaking waves. In their method, they revised the formulation of viscosity to conserve angular momentum exactly, and they used a correction matrix to guarantee that the gradient of the velocity field was correct. They found that the new technique was able to more accurately model the water surface during a number of different breaking waves than previous iterations of the ISPH method. The technique with revised viscosity formulation was then used by Khayyer et al. (2009) to model the pressures during a number of wave impacts. They found that their variant of the SPH technique could accurately predict the pressure during a wave impact on vertical walls. This technique was again used by Gotoh et al. (2014) to model violent sloshing flows, and they found that the conservation of angular momentum enhancements made to the

ISPH method produced more accurate predictions of the sloshing induced impact pressures.

Sloshing problems have also been investigated by Rafiee et al. (2012), who compared the normal SPH method, ISPH, and a Gogunov-type SPH method (GSPH). In their study, they compared three SPH methods to experimental results and demonstrated the capabilities of the methods to predict the impact pressures during sloshing. The SPH and ISPH methods were shown to possess significant high-frequency oscillations, however the SPH method possessed significantly more noise. In contrast, the GSPH method had considerably less noise in the measured pressures, but the peak force was under-predicted by 30% to 40%. They also performed a convergence study on the three methods, finding that the GSPH method possessed the greatest convergence rate. However, in their report, they did not make any general recommendations from this finding.

SPH has also been used to model green water effects and ship flooding by Le Touzé et al. (2010). In their study, they observed the green water effects on a scale model FPSO (length 3.5156 m, width 0.7188 m, weight 649 kg) with a series of waves, and compared the deck water height predicted from both 2D and 3D SPH to an experimental case (Yang et al., 2007). The ship's motion in simulations was prescribed to match the recorded motion in the experiments. In 2D, the predicted deck water height was comparable to that observed in the experiments; however, in 3D, the water height was predicted to be up to a factor of 2 times larger than in the experiments. The researchers attributed this discrepancy to the 50% larger particle spacing used in the 3D simulation. In addition to this error, it was likely that the prescribed ship's motion would differ from how the ship would respond if its motion were allowed to respond to a dynamic sea state. Furthermore, the draught of the ship was 77% of the ship's moulded depth. This is much larger than the typical draught for an FPSO, and consequently, this ship was highly susceptible to green water effects.

Researchers at the Ecole Centrale de Nantes have been working on models using SPH (Shadloo et al., 2015). Of particular note is the work of Guilcher et al. (2013) on modelling the impact of breaking waves on a rigid wall. Guilcher and colleagues found that these types of violent impacts often induce large forces on the wall or structure due to air entrapment or cavitation effects, both of which can be difficult to numerically model. In their work, they found that a two-phase fluid compressible SPH model was able to reasonably estimate the forces due to the breaking wave impact. Le Touzé et al. (2013) investigated the pressure distributions in the standard SPH model, finding that the commonly reported high-frequency pressure oscillations were linked to the fluid domain eigenfrequencies. To reduce these pressure oscillations they implemented a higher order SPH model, which yielded improvements in the pressure field accuracy, but also increased the CPU costs and the conservation of energy was no longer intrinsically guaranteed.

Rogue waves have also been studied using SPH in a small number of studies. Patel et al.

(2009) and Campbell and Vignjevic (2012) utilised the SPH technique for studying the effect of rogue waves on structures in the ocean. Both studies reported on a number of validation tests involving object equilibrium orientation and rising cylinder cases. In each case comparing their results to the Volume of Fluid numerical results presented in Fekken (2004). They showed that the simulations were able to predict the overall equilibrium position of the objects; however, the errors in the amplitudes and periods of oscillation were not discussed. Additionally, the researchers of both studies discussed an impacting case of a helicopter sub-floor structure on a body of water. The results of which were significantly different to experimental data. The researchers explained that direct comparisons were difficult as the experimental model was not fully rigid, and that air was not modelled in the simulations. They explained that the differences they observed were consistent with the behaviour observed in other studies, citing the thesis of de Vuyst (2003) for justification; however, more accurate simulations are required before confidence in their method can be achieved.

The application of the rogue waves are where the papers of Patel et al. (2009) and Campbell and Vignjevic (2012) differed. Patel et al. (2009) simulated a rogue wave impact on a simplified ocean tanker, reporting that the SPH technique had potential for determining ship performance under the effect of rogue waves or high wave sea states. Campbell and Vignjevic (2012) analysed the impact of a rogue wave on a buoy that was moored to the sea bed. They reported that the SPH technique could be extended to model the wave loading of floating structures under extreme waves. Both the Patel et al. (2009) and Campbell and Vignjevic (2012) studies were limited to a single processor as their solver method was not implemented for parallel processing. Consequently, the resolution in their studies was restricted so the simulations could be completed without excessive runtimes. At such coarse resolutions, it was difficult to determine whether the poor results were due to the SPH technique or to the coarse resolution.

Rudman and Cleary (2013, 2016) also performed an analysis of a rogue wave impact on a Tension Leg Platform (TLP). The results they obtained highlighted the potential for SPH to be utilised in platform design. However, to generate their rogue wave they used a momentum source that moved through the domain at a prescribed speed, and was then switched off shortly before the TLP. This resulted in a released bulk of water impacting the TLP which is not representative of a real wave. The subsequent platform motions did appear to be well predicted, and information on the motion and mooring cable tensions were obtained. However, due to the unrealistic wave used, caution must be taken when using these results.

The studies of SPH presented in this chapter highlight a key strength of the method: that SPH is capable of modelling complex free surfaces, as well as fluid interactions with moving boundaries and objects. When studying a rogue wave impact on a floating tethered body, both the free surface and its interaction with a potentially moving boundary are important. Therefore, SPH is a promising method for accurately modelling these kinds of impacts. However, the SPH method has not specifically been verified for modelling a rogue wave. Since these waves are

complex in nature, it is important to ensure that they can be modelled accurately. Furthermore, the study of a floating object interacting with a free surface using SPH has only been verified to be accurate for 2D flows, and not 3D flows. When designing a vessel or offshore structure to survive a rogue wave impact, a 2D interaction would not be sufficient. As such, the SPH method needs to be verified for 3D interactions.

## 2.4 Summary and research questions

From the review of the literature presented here, it is clear that rogue waves are a serious threat to ships, vessels and other offshore structures operating at sea. Rogue waves have been studied both experimentally and numerically; however, only experimental and 2D numerical studies have been used to model a rogue wave impact on a vessel. The 3D numerical models that have been studied have only been used to predict the generation of a rogue wave, but the methods were not used for predicting an impact.

A review of studies using SPH found that it was clearly capable of modelling complex free surface waves, as well as their interaction with both solid and moving rigid objects. However, SPH has only been proven to be capable of modelling wave and floating object interactions in 2D. Further research is needed to explore the accurate modelling of wave interactions in 3D. In addition, the studies that modelled a rogue wave impact using SPH were limited, either by poor resolution or generation methods that were not realistic. Therefore, the SPH method needs further investigation into its efficacy of accurately modelling both the interaction between surface waves and floating objects and a rogue wave.

The literature on rogue waves revealed that there were a number of possible generation mechanisms for these waves. However, a representative wave could be used for modelling the impact on a vessel without introducing significant errors. The NLS were shown to be capable of producing waves that were representative of a unidirectional rogue wave, making them a viable option for modelling rogue waves both experimentally and by SPH modelling.

Further research is also needed to explore if SPH is capable of accurately modelling a rogue wave impact on an offshore structure. This research aims to answer the following questions:

1. Can SPH accurately model the interaction between surface waves and a floating tethered body, and what is the order of magnitude of the errors?
2. How accurately can SPH model a rogue wave described by the NLS?
3. What are the physical consequences of a rogue wave impact on a floating tethered body (in particular, a moored ship)?

The following chapters now address these research questions.

# Chapter 3

## Methodology

The main aim of this study is to investigate the efficacy and accuracy of an SPH model for predicting the interaction between a floating tethered body (a moored ship in this study) and a rogue wave. A review of the literature showed that little or no quantitative experimental data was available on the interaction between fluid free surfaces and floating tethered bodies. Furthermore, the SPH method has not previously been used to simulate Peregrine breather type rogue waves. Therefore, rigorous validation against experimental results is required before confidence in the method can be found. This study uses the following methodology to validate this confidence.

A set of three initial experiments will investigate the efficacy and accuracy of SPH in modelling:

- the oscillation of a tethered, spherical buoy on the surface of a body of water;
- the motion response of the same buoy to a sinusoidal wave train; and,
- the generation of first and second order rogue waves.

The SPH results from these three experiments will be compared to experimental data. This can then be used to verify the confidence of the SPH method for specific situations. These experiments not only indicate the factors and parameters required to obtain accurate simulations, but could also provide confidence in the results of other similar simulations without experimental comparisons.

If confidence in the SPH model is established, then it will be used to model a rogue wave impacting a floating tethered ship. The advantage of performing simulations at full scale is that the accuracy of real-world dimensionless numbers (such as Reynolds and Froude numbers) is guaranteed.

If the SPH model is verified as an accurate numerical method for modelling both rogue waves and wave-structure interactions, an offshore structural designer could gain greater confidence

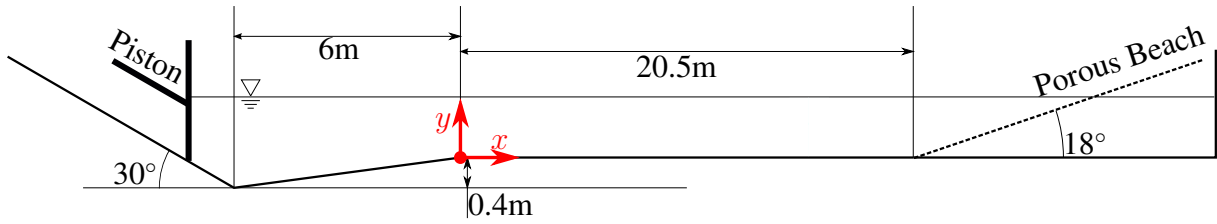


Figure 3.1: Schematic of the Wave Tank used. This section view is along the central plane of the tank. The red dot and axes represent the position of the coordinate system origin. Not to scale.

that the physics were being modelled just as accurately as it were in the experimental method; and in real-life scenarios.

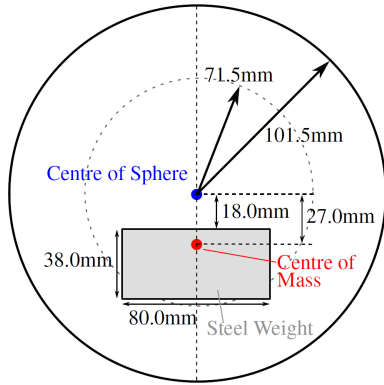
## 3.1 Experimental equipment

This section presents the experimental equipment that were used in the various experiments of this study.

### 3.1.1 Monash Wave Tank

The experiments performed in this study were conducted in the Monash Wave Tank. The tank is a 1 m wide flume that extends for approximately 35 m. A side view schematic is presented in Figure 3.1. A hydraulically driven, piston-type wave generator is present at the left end of the tank, which moves parallel to a 30° sloped floor. Following the piston region, the tank floor inclines upwards by 0.4 m over 6 metres. The tank floor is then flat for the next 20.5 m of the tank. This is the working section of the tank. A porous, wave damping beach is placed into the tank, commencing at the end of the working section. The beach extends upwards at an angle of 18° and the end wall of the tank is located shortly after the beach has risen 2 metres above the floor.

For all of the experiments and simulations, the  $x$ -coordinate is defined in the lengthwise direction of the tank (toward the beach and away from the piston), the  $y$ -coordinate in the upwards vertical direction, and the  $z$ -coordinate across the tank ('out of the page' with respect to Figure 3.1). The origin of the coordinate system is set so that  $x = 0$  is at the start of the working section,  $y = 0$  is at the floor of the working section, and  $z = 0$  is at the mid-plane of the tank ( $z = \pm 0.5$  corresponds to the side walls). The coordinate system origin is shown in Figure 3.1 by the red axes. A water depth of 80 cm, measured in the working section, was used in each of the test experiments.



(a) Cross section schematic of the buoy. The buoy and steel disk are cylindrically symmetric about the vertical line of symmetry.



(b) The octant pattern painted on the buoy

Figure 3.2: The spherical buoy used in the experiments

### 3.1.2 Tethered buoy

A spherical tethered buoy was used in the experiments performed in this study. It was constructed to have a mass of 1.745 kg and radius of 101.5 mm. The buoy was made from a hollow sphere of high density expanded polystyrene (density of  $29.5 \text{ kg/m}^3$ ) with 40 mm thickness. To ensure that the centre of mass was located below the centroid (guaranteeing a stable sitting orientation in the water) a 38 mm thick steel disk of 40 mm radius was placed in the lower half of the buoy, shown in Figure 3.2a. This steel disk provided the majority of the mass to the buoy and offset the centre of mass to 27.0 mm below the centroid. The moment of inertia matrix about the centre of mass was calculated using a CAD (SolidWorks) software representation of the buoy to be:

$$I = \begin{bmatrix} 1.735209 & 0 & 0 \\ 0 & 1.776363 & 0 \\ 0 & 0 & 1.735209 \end{bmatrix} \times 10^{-3} \text{kg} \cdot \text{m}^2 \quad (3.1)$$

The buoy was painted with a black and white octant (Figure 3.2b) pattern to improve visibility in the motion capture process. Additional markers were added to the white sections to provide more tracking points, and thus more reliable processing, and is discussed in Section 3.1.4.

Offshore structures in deep water can be tethered by cables that, due to their length, are noticeably elastic. In order to represent a similar scenario, the buoy was tethered to the tank floor using a cable (1 mm diameter) and spring (stiffness  $k = 30.88 \text{ N/m}$ ) system shown in Figure 3.3. A coil spring was required at the laboratory scale as the cable length is not sufficient to be noticeably elastic. The coil spring, however, could create significant additional damping when expanding or contracting while underwater, making it potentially difficult to incorporate into the SPH model. Consequently, a pulley system was used near the tank floor that allowed

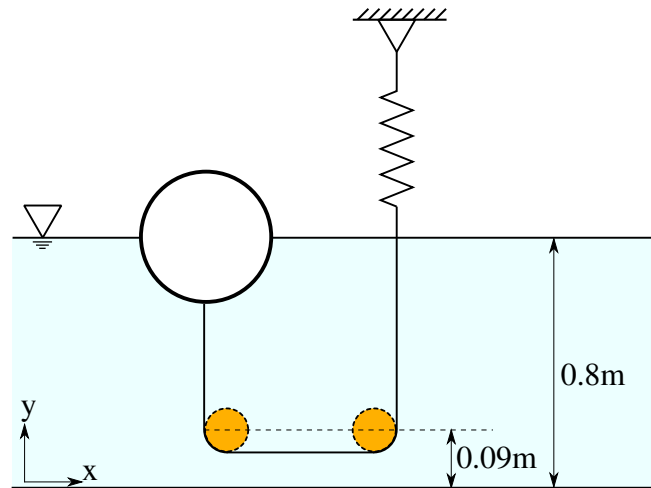


Figure 3.3: Schematic of the experimental setup with the floating tethered buoy at its resting position. Note that the figure is not to scale.

the spring to be located above the water. The length of the cable and spring pre-tension were set so the resting position of the buoy is half-submerged.

### 3.1.3 Wave gauges

Four gauges were used in the experiments to measure the surface profiles as a function of time at four locations. The gauges consisted of a pair of vertical wires that varied in resistance as they became more or less submerged. The signal measured from the gauges was recorded and converted to a wave height. The gauges were calibrated before each test to ensure that the conversion from electrical signal to surface elevation was accurate. Each calibration gave a linear relationship between the signal and wave height, though the offset varied between calibrations. This was due to the different ambient conditions between experiments, and difficulty in placing the gauges in the water at exactly the same height as previous experiments.

### 3.1.4 Motion capture

Motion capture software was used to measure the trajectory of the buoy in the experiments. The software, SwiMCap (developed at CSIRO), utilised multiple synchronised camera views to determine the 3D location of an object in the fields of view.

In the experiments, the cameras were located above the water surface and looked down at the buoy. In this way, no refraction effects were present except for lens distortion. To take this into account, the camera calibration for such cases were performed *ex-situ*. Each camera used in the experiment was calibrated using OpenCV to determine the intrinsic parameters (such as the focal length, principal point, and distortion factors). A chessboard pattern, shown in



Figure 3.4: Camera views from the four cameras used to record the buoy motion. The red light used to synchronise timing is seen in each image at the end of the pole.

Figure 3.5, was used to perform this calibration. The intrinsic parameters were then combined with landmarks in the view to determine the cameras extrinsic properties (i.e., location and orientation) precisely.

### 3.1.4.1 Cameras

Four Sony HDR-CX220E video cameras were used to record the buoy motion in the experiments. The cameras were placed at four locations around the buoy to allow a motion tracking technique to be used to determine the 3D coordinates of the buoy's centroid. For the experiments, all cameras were set to the same quality settings, including a frame rate of 50 frames per second. The shortest period of oscillation observed through the experiments was 0.6 s, or 30 frames, so the frame rate was deemed to be satisfactory. During the experiments, a red light (see Figure 3.4) was flashed in the field of view of all cameras, allowing the cameras to be synchronised during post-processing.

### 3.1.4.2 Camera calibrations

For each camera, the intrinsic and extrinsic properties that described the transformation from laboratory coordinates  $(x_l, y_l, z_l)$  to pixel coordinates  $(u, v)$  needed to be known to provide estimates of the marker's position. The transformation between laboratory and pixel coordinates

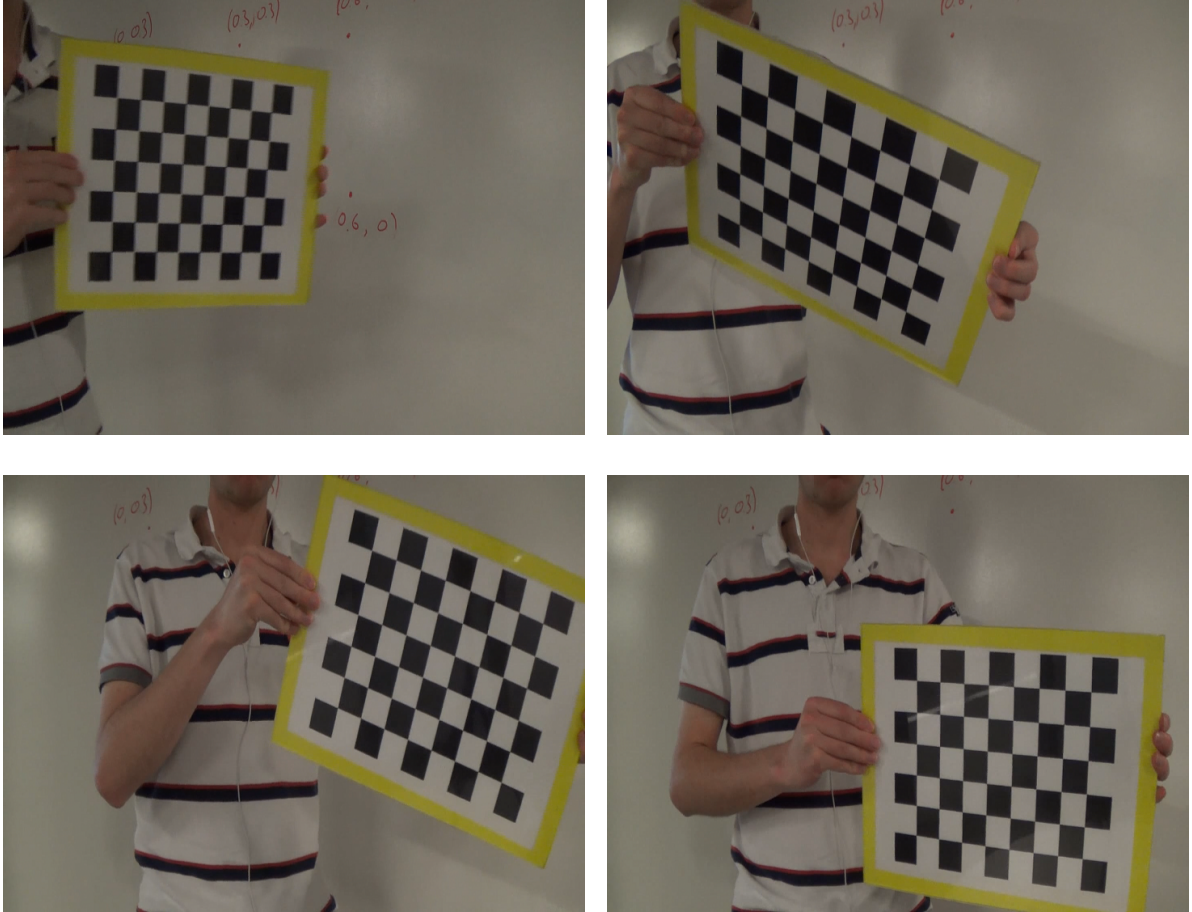


Figure 3.5: In the calibration method a chessboard pattern is moved in front of the camera in a range of positions and orientations. The calibration software used the distortion of the pattern to determine the intrinsic properties of the camera.

is given by the following:

$$\begin{bmatrix} uw \\ vw \\ w \end{bmatrix} = C \begin{bmatrix} x_l \\ y_l \\ z_l \\ 1 \end{bmatrix} \quad (3.2)$$

where  $w$  is a scaling factor,  $C = A [R T]$ ,  $A$  is the  $3 \times 3$  intrinsic parameter matrix (camera, lens, and other distortions), and  $R$  and  $T$  are the extrinsic parameters describing the rotational and translational transformations between laboratory coordinates and 3D camera coordinates. A checkerboard pattern calibration was used to determine the values for matrix  $A$  of each camera. The checkerboard was placed in front of the camera at different positions and slopes, and each image was inputted into an OpenCV calibration application. Example images of this process are shown in Figure 3.5.

Once camera calibration was complete, mapping of the wave tank was undertaken. Numerous landmarks were marked on the walls of the tank. Their laboratory coordinates were known exactly. The cameras were placed so that there were as many landmarks in the view as possible to

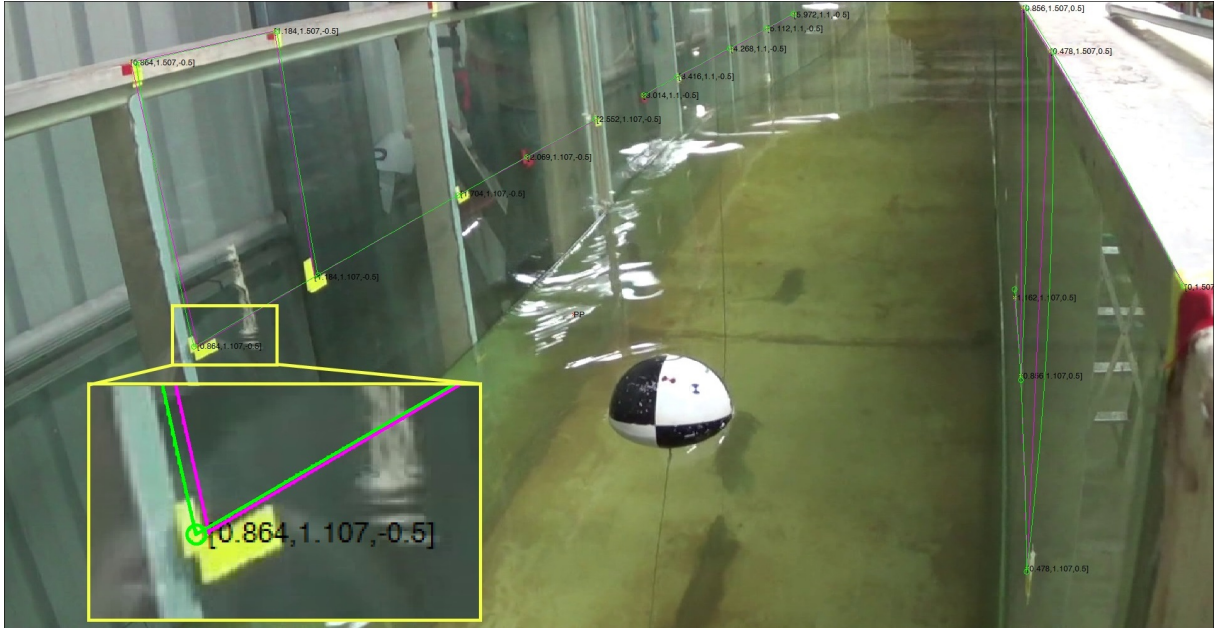


Figure 3.6: Locating the landmarks in the field of view. The vertices of the pink lines indicate the location of the landmark on the screen. The green lines are a reprojection of the pink lines, giving a visual indication whether the calibration is accurate or not. A zoomed view has been edited into this image showing a landmark at  $(x, y, z) = (0.864, 1.107, -0.5)$ .

ensure the extrinsic properties were more accurately obtained. The landmarks were then identified in the camera view and used to determine the  $[R T]$  matrix using the OpenCV calibration application. Figure 3.6 shows the locations of some of the landmarks. These are identified by the inside corners of the L shapes for landmarks partway up the wall, and by the edge between the red and yellow tape at the top of the wall.

In the motion capture process, the pixel coordinates of a point can be known for a single view, but this single view is not sufficient to determine the point's laboratory coordinates. This is because  $C$  is a  $3 \times 4$  matrix and so it cannot be inverted, thus finding  $(x_w, y_w, z_w)$  from a single known pixel coordinate using Eq. (3.2) is impossible. In fact, an infinitely long line of points will satisfy the equation for that camera since there are fewer data points than there are unknowns.

To identify the location of a particular marker, it must be visible in at least two camera views so that the lines of possible points intersect. However, potential errors can be introduced in the calibration process, such as human error for example, when the user identifies the  $(u, v)$  coordinates (i.e., inaccurate clicking on the markers in the software). Therefore, a least squares method was used to estimate the laboratory coordinates of the point that was closest to the lines of possible solutions. The full derivation of the least squares algorithm used is included in Appendix A. If the lines of possible solutions are parallel, or close to parallel, then the least squares method can fail to find an accurate solution, if one is found at all. In practice, if more than two cameras can view the marker then an estimate can be validated. If only two cameras

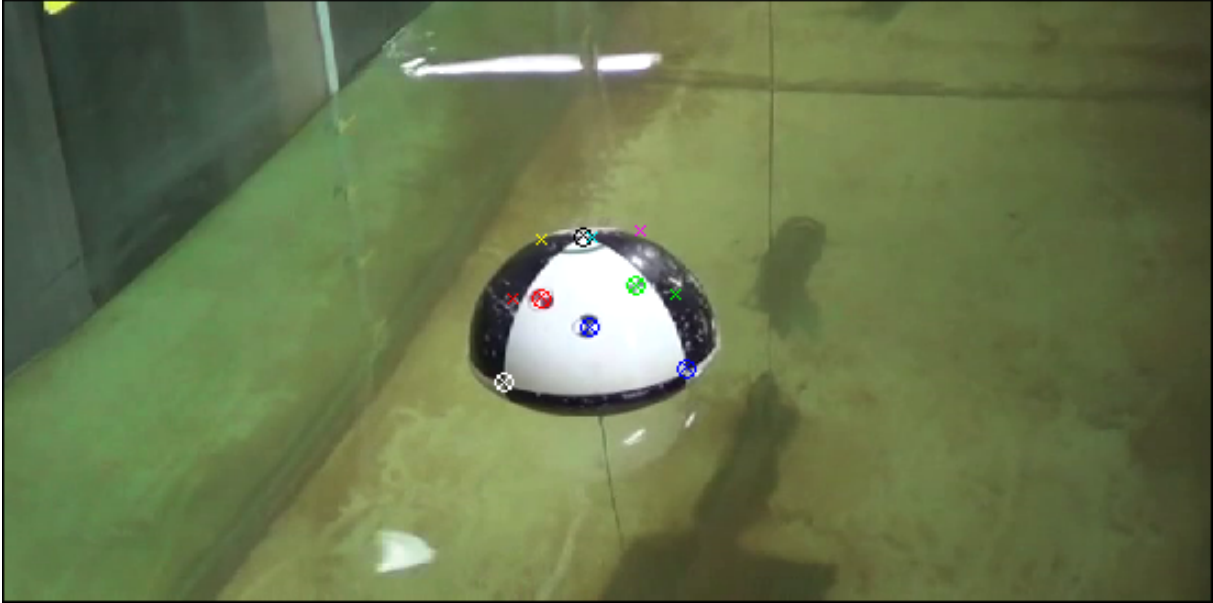


Figure 3.7: Identification of the markers on the surface of the buoy. Six of the 11 markers are visible in this frame and are marked with a circle. The crosses represent the estimated marker location based on this camera and other cameras where the marker was visible and are included in views where the marker was not present (e.g. the yellow marker is not visible in this view but its estimate is included here). Only 8 identifier colours were available, so blue, green and red are repeated.

viewed the marker, then an estimate could be found if the marker was sufficiently far from the other camera in both views.

### 3.1.4.3 Tracking the buoy

A total of 11 markers on the upper hemisphere of the buoy were tracked during the experiments: 3 markers in each of the white octants, and the 5 intersections of black and white octants. Figure 3.7 shows an example view of the buoy in one of the experiments, with 6 markers present in the particular view. Since the markers are on the surface of a sphere of known radius,  $R_T$ , the location of the sphere's centroid can be calculated by defining a function:

$$f_E(\mathbf{x}) = \sum_i (|\mathbf{x} - \mathbf{x}_i| - R_T)^2 \quad (3.3)$$

where  $\mathbf{x}_i$  is the calculated position of marker  $i$ . The function  $f_E$  essentially tries to fit a sphere of radius  $R_T$ , centred at  $\mathbf{x}$ , to the set of marker locations and returns an estimate of the error. The MATLAB function `fminsearch` was then used to find the location of the centroid  $\mathbf{x}$  that minimised the error of the sphere fit.

## 3.2 Smoothed Particle Hydrodynamics method

This section presents the mathematical formulation of the SPH methodology used in this study.

### 3.2.1 Time stepping scheme

The equations of motion (Eq. (2.15)) were integrated in time using a predictor-corrector scheme. In this scheme, the predictor step utilises a standard Euler scheme to project a time step using the current time step's rates of change. This is summarised by:

$$\bar{\mathbf{v}}^{n+1} = \mathbf{v}^n + \delta t \mathbf{a}^n \quad (3.4a)$$

$$\bar{\mathbf{r}}^{n+1} = \mathbf{r}^n + \delta t \mathbf{v}^n \quad (3.4b)$$

$$\bar{\rho}^{n+1} = \rho^n + \delta t D^n \quad (3.4c)$$

where  $\mathbf{a}$  and  $D$  denote the rates of change of velocity and density in Eq. (2.15b) and Eq. (2.15c) respectively. The superscript  $n$  refers to the time step, while the overbar denotes the predicted next time step values. The predicted rates of change of velocity and density at the next time step ( $\bar{\mathbf{a}}^{n+1}$  and  $\bar{D}^{n+1}$ ) are calculated via Equations (2.15b) and (2.15c) using  $\bar{\mathbf{v}}^{n+1}$ ,  $\bar{\mathbf{r}}^{n+1}$  and  $\bar{\rho}^{n+1}$ . The predicted values are then corrected by

$$\mathbf{v}^{n+1} = \mathbf{v}^n + \delta t \bar{\mathbf{a}}^{n+1} \quad (3.5a)$$

$$\mathbf{r}^{n+1} = \mathbf{r}^n + \delta t \bar{\mathbf{v}}^{n+1} \quad (3.5b)$$

$$\rho^{n+1} = \rho^n + \delta t \bar{D}^{n+1} \quad (3.5c)$$

### 3.2.2 Particle searching optimisation

The kernel function has a compact support region of  $2h$ , meaning that if the distance between particles  $i$  and  $j$  is more than  $2h$  then  $W$  will equal 0. When the domain contains a large number of particles farther than  $2h$  apart, then the summations in the equations of motion will perform a large number of unnecessary calculations. Performing these meaningless calculations is time-consuming, so a searching algorithm was employed to check whether a particle could potentially have an influence. The entire domain was divided into a grid of cells of width  $2h$ , with an integer number of cells in each dimension.

Figure 3.8 shows an example particle in a particular cell with its radius  $2h$ . This particle may only influence other particles in neighbouring cells that fall within this radius. At each time step, the cell that each particle is contained in is determined, then the summations in the equations of

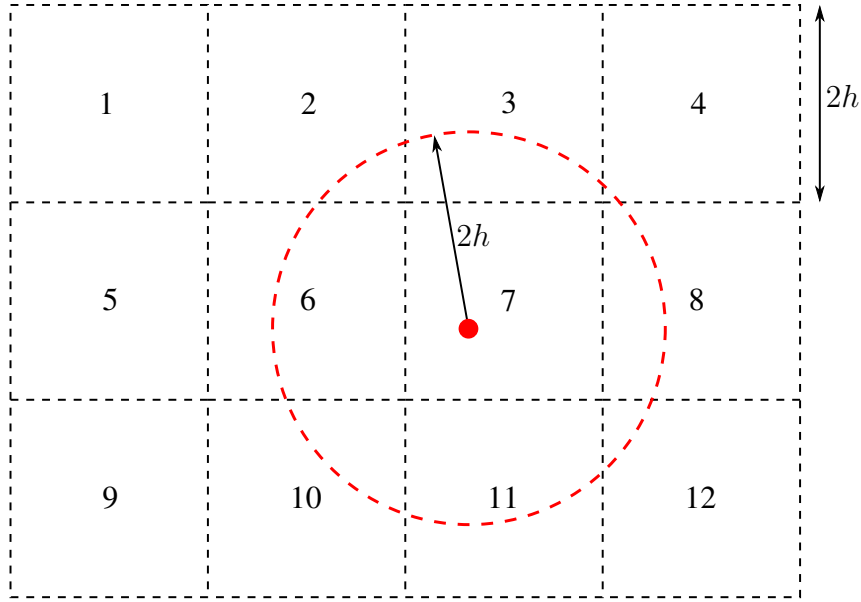


Figure 3.8: SPH domain subdivision cells. A particle may only be influenced by a particle in a neighbouring cell, so particle summations ignore particles in cells more than one step away

motion only refer to particles that are in a  $3 \times 3$  (in 2D) or  $3 \times 3 \times 3$  (in 3D) neighbouring grid. In Figure 3.8, the red particle in cell 7 has a compact support region (the dashed circle) that can potentially reach the neighbouring cells, but cannot reach cells 1, 5, or 9 so the particles in these cells were not included in calculations.

### 3.2.3 Parallelisation

All of the simulations performed in this thesis were conducted on the CSIRO Accelerator Cluster, also known as the Bragg cluster. The cluster consisted of 128 Dual Xeon 8-core E5-2650 Compute Nodes (i.e., a total of 2048 compute cores) with 128 GB of RAM, 500 GB SATA storage and FDR10 InfiniBand interconnect. The cluster also had GPU capabilities, however, the SPH code used in this thesis was not constructed for use on GPUs, so only CPUs on the cluster were used. However, the SPH code used is a shared memory code, so it was limited to using a single node, or a maximum of 16 cores.

To take advantage of the multiple cores available on each node, an OpenMP implementation was used in the code. This was because it was simple to implement from an original serial code base and did not require complex domain decomposition. An internal study conducted by CSIRO on the speedup effects had been performed (Cummins, private communication), and is shown in Figure 3.9. The study made use of a 3D Dam Break with 770,000 particles. The speedup,  $S$ , was defined by taking the ratio between the wall time for a single processor and the wall time for multiple processors:

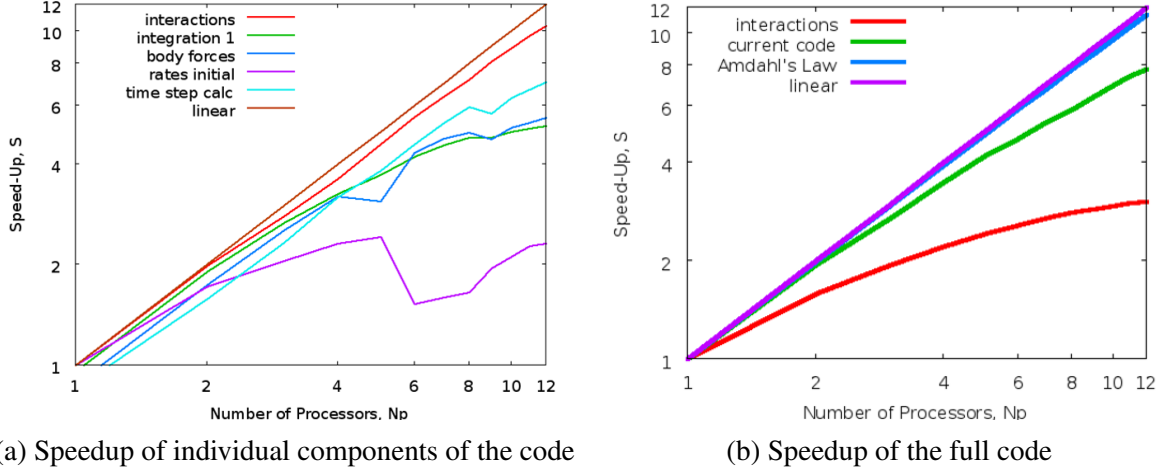


Figure 3.9: Speedup from performing the SPH code using multiple processors in parallel. Figures provided by Cummins (obtained with permission via private communication).

$$S = \frac{\text{time}(Np = 1)}{\text{time}(Np)} \quad (3.6)$$

The time here discounts the time spent in the setup and completion phases of the simulation. Note that this study was performed on an older cluster which had 12-core nodes, and no data was available for the speedup of 16 cores on which the majority of simulations in this study were actually run.

The study found that the particle interactions had the greatest speedup when implemented in parallel (shown in Figure 3.9a). This was useful since approximately 70% of the wall clock time was spent calculating the interactions between SPH particles when a serial SPH code was used. Conversely, the calculation of the rates of change had the least speedup but only 3.5% of the wall clock time was spent performing these calculations.

Figure 3.9b shows the speed up effects for the entire code when implemented in parallel. A special code where only the particle interactions are performed in parallel was also included in this plot and was shown to have significantly less speedup for large numbers of processors. When 12 processors were used, parallelising the interactions only yielded a speedup of approximately 3, but if all components were parallelised then the speedup was approximately 8.

The speedup curves all indicated that further improvements could be made if more than 12 cores were used. However, for smaller simulations (i.e., significantly fewer particles) the speedup obtained by using more cores decreased due to the overheads of the parallelisation becoming proportionally more significant. For these types of simulations, the maximum number of cores on the Bragg cluster was not used. Where fewer than 16 cores were used in the simulations performed in this thesis, the number of cores used will be explicitly stated.

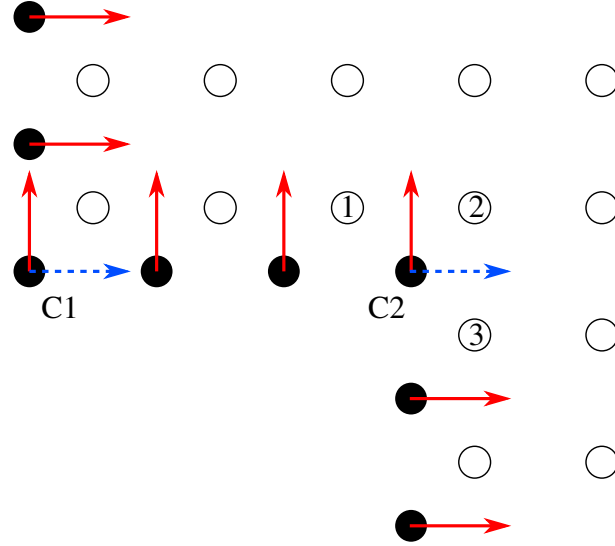


Figure 3.10: The boundary normal implementation for modelling boundaries in SPH. Each of the boundary normals exerts a repulsive force on the fluid particles (white) preventing them from penetrating the layer of boundary particles. Corners C1 and C2 are modelled using multiple normals.

## 3.2.4 Boundary model

### 3.2.4.1 Boundary model

One of the strengths of SPH is the natural modelling of the interaction between fluid particles and boundaries, such as objects and walls. SPH models these boundaries by using both particles and the equations of motion that provide the interaction between the particles. However, there are a number of boundary treatments that could be used. Cummins et al. (2012) discussed two of these methods in some detail: boundary normals and ghost particles. Although the ghost particle boundary treatment showed improved wave reflection modelling, the boundary normal treatment was used in this study for two reasons. Firstly, it was difficult to set up ghost particles for complex geometries, such as acute corners. Secondly, it was straightforward to determine the normal and tangential components of the force on the objects.

The boundary normal method models the boundaries by defining a vector at each particle that is perpendicular to the boundary surface. The boundary is modelled as a single layer of particles and exerts a repulsive force on the fluid particles that approach the boundary particles in the direction of the boundary normals, preventing the fluid particles from penetrating the boundary. Figure 3.10 shows the black boundary particles with their normals represented as arrows, and the fluid particles as the white filled circles. The normal force acting on the fluid particle  $i$  from boundary particle  $k$  takes the form of:

$$\mathbf{F}_{ik} = \frac{0.01c_s^2m_i}{h}B(\mathbf{r}_{\parallel})S(\mathbf{r}_{\perp})\hat{\mathbf{n}}_k \quad (3.7)$$

where  $\mathbf{r}_\perp$  represents the perpendicular distance between the particles parallel to the normal vector  $\hat{\mathbf{n}}_k$  (i.e. perpendicular to the boundary surface), and  $\mathbf{r}_\parallel$  is the distance between the fluid and boundary particle parallel to the boundary surface. The boundary potential term  $S$  is written:

$$S(q) = \begin{cases} \left[ \left( \frac{sd}{s+2} \right) \frac{1}{q} \right]^s & 0 \leq q \leq \left( \frac{sd}{s+2} \right) \\ \left( \frac{s+2}{2d} \right)^2 (q-d)^2 & \left( \frac{sd}{s+2} \right) \leq q \leq d \\ 0 & \text{otherwise} \end{cases} \quad (3.8)$$

where  $q = \mathbf{r}_\perp \cdot \hat{\mathbf{n}}_k/h$ ,  $s$  is typically set to 8, and  $d$  determines how far away from the wall boundaries the wall force was felt. This value was typically chosen to be 1. The function  $B$  smooths the force tangentially to ensure a constant total force from the boundary particles on a fluid particle as it travels parallel to a row of boundary particles:

$$B(\mathbf{r}_\parallel) = \begin{cases} 1 - \frac{|\mathbf{r}_\parallel|}{\delta x} & 0 \leq |\mathbf{r}_\parallel| \leq \delta x \\ 0 & |\mathbf{r}_\parallel| > \delta x \end{cases} \quad (3.9)$$

Note that  $S$  is 0 if the fluid particle is behind the boundary normal (for example, particles 1 and 3 to the dashed and solid normals respectively in Figure 3.10). Consequently, the corner boundary particles (C1 and C2 in Figure 3.10) require an extra normal to prevent fluid particles from getting too close to the boundary particle. For example, without extra normals fluid particle 3 in Figure 3.10 could approach C2 from the lower right direction and the solid normal would not repel the particle. If the particle is very close to the corner when it passes the boundary and begins to observe the normal force, the value of  $q$  would be very small resulting in a large and unrealistic value of  $S$ . Using the extra normal prevents the particle from approaching the corner boundary particle. When a particle is “in-front” of multiple normals to the same boundary particle, such as particle 2 to corner particle C2, the normal is converted to a single effective normal that points directly toward the fluid particle.

### 3.2.4.2 Boundary offset

The smoothed particle nature of SPH introduces some uncertainty when determining the exact edge of a boundary, be it an object or wall boundary or fluid domain boundary. The most intuitive method is to define boundary particles on the physical boundary. However, a particle represents a region of mass centred at the particle’s location with radius of approximately  $\delta x/2$ , so for the fluid very close to the physical boundary to be represented, the fluid particle should be able to approach within one particle spacing of the boundary. The boundary potential term, Eq. (3.8), becomes nonzero when a particle is within a distance  $dh$  from the boundary particle

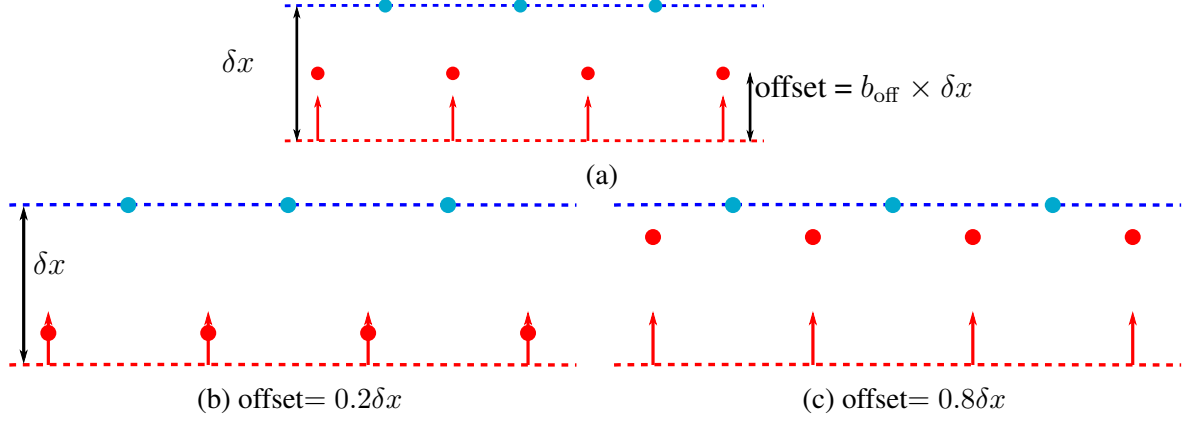


Figure 3.11: The  $b_{\text{off}}$  parameter is used to alter the distance  $r_{\perp}$ . (b) Smaller values of  $b_{\text{off}}$  force fluid particles (blue) away from the boundary particles (red) sooner, while (c) larger values allow the fluid particles to get closer to the boundary particles.

( $dh = 1.2\delta x$  in this study) and results in the fluid particles remaining approximately one particle spacing away from the boundary under most circumstances.

To allow the fluid particles to approach within one particle spacing of the boundary, an offset is applied to where  $r_{\perp}$  is measured from. This effectively pushes the boundary particles back into the body. The boundary offset is controlled by a parameter,  $b_{\text{off}}$ , that allows the offset to be modified. The offset is determined by setting:

$$\mathbf{r}_{\perp}^* = \mathbf{r}'_{\perp} + b_{\text{off}}\delta x\hat{\mathbf{n}}_k \quad (3.10)$$

where  $\mathbf{r}'_{\perp}$  is the perpendicular distance to the original boundary particle location and  $\mathbf{r}_{\perp}^*$  is the perpendicular distance used for defining  $q$  in Eq. (3.8).

Some examples of the effect of  $b_{\text{off}}$  are shown in Figure 3.11, where the offset boundary is represented by a red dotted line below the red boundary particles, and the blue fluid particles are kept approximately one particle spacing from the offset boundary. A detailed study on the effect of  $b_{\text{off}}$  is presented in Section 4.1.

### 3.2.5 Calculating the location of the fluid surface

As mentioned in Section 3.2.4.2, there is some uncertainty in determining the location of the fluid surface, so an approximation is required. The approximation uses the particle density at a location,  $\xi(\mathbf{r})$ , which is defined by:

$$\xi(\mathbf{r}) = \sum_i \frac{m_i}{\rho_i} W(|\mathbf{r} - \mathbf{r}_i|, h) \quad (3.11)$$

and assumes that the fluid surface is located where the particle density equals a specified number,  $\xi_t$ .

To determine the location where the number density equals  $\xi_t$ ,  $\xi$  is calculated at  $\mathbf{r} = (x_l, \eta, z_l)$  where  $x_l$  and  $z_l$  are the  $x$  and  $z$  coordinates of the location where the user wishes to measure the surface elevation, and  $\eta$  is the  $y$ -coordinate at the top of the SPH domain. If  $\xi$  is less than  $\xi_t$ ,  $0.1\delta x$  is subtracted from  $\eta$  and  $\xi$  is recalculated. When  $\xi$  is greater or equal to  $\xi_t$ , linear interpolation with the previous point is employed to obtain an estimate of the fluid surface location.

### 3.2.6 Cables in SPH

The cable and spring system is modelled in SPH by defining a force which mimics a linear spring acting at a specific point on the buoy. The ends of the cable are specified: one in the local coordinates of the object, and another in the global coordinates. The initial length of the cable and a spring stiffness are also specified. During the simulation, the distance between the two points is calculated, and a force is exerted on the object. This force is based on the stiffness of the cable and its extension from the cable's initial length. When the distance between the points is equal to or less than the initial length of the cable, no force is applied.

Since the force is calculated based on the two end points, there is no need for the pulley system. The end of the cable that should attach to the pulley is defined with an endpoint directly below the centre of the buoy (when at equilibrium) and 9 cm above the floor (equivalent to where the cable touches the front pulley in the experiments).

# Chapter 4

## Using SPH for modelling surface waves

There are two major technical issues in the SPH method that have implications for the undertaking and interpretation of the results. An investigation into these is required before the main body of simulation work can be done. This chapter discusses these the investigations into these issues.

Some uncertainty exists in the exact location of the boundaries of the fluid domain. This is due to the kernel estimation used by SPH to model the sphere of influence of each particle. A number of assumptions can be made about how these locations are modelled. For example, one such assumption was the boundary offset discussed in Section 3.2.4.2. In the first section of this chapter, the effect that these modelling assumptions may have when determining the location of the fluid surface and solid boundaries are investigated.

In the main body of simulations, surface waves will be produced using SPH and compared to experimentally produced waves. However, replicating the entire domain in SPH requires an infeasibly large number of particles, that include modelling parts of the domain that are not critical to the experiments undertaken in this study. In the second section of this chapter, an alternative method of generating surface waves is investigated to reduce the required domain size and the number of particles.

### 4.1 Investigating the boundary and free surface models

The particle nature of SPH allows the method to naturally model deforming fluid domains, but it also introduces uncertainty in the location of fluid boundaries. These uncertainties arise because an SPH particle represents a non-uniform distribution of mass around its centre that has influence on a region of radius  $2h$ . Consequently, a density gradient is observed at fluid boundaries rather than the discontinuity that exists in reality. For the fluid free surface, the uncertainty in fluid boundary means that the free surface location is approximate.

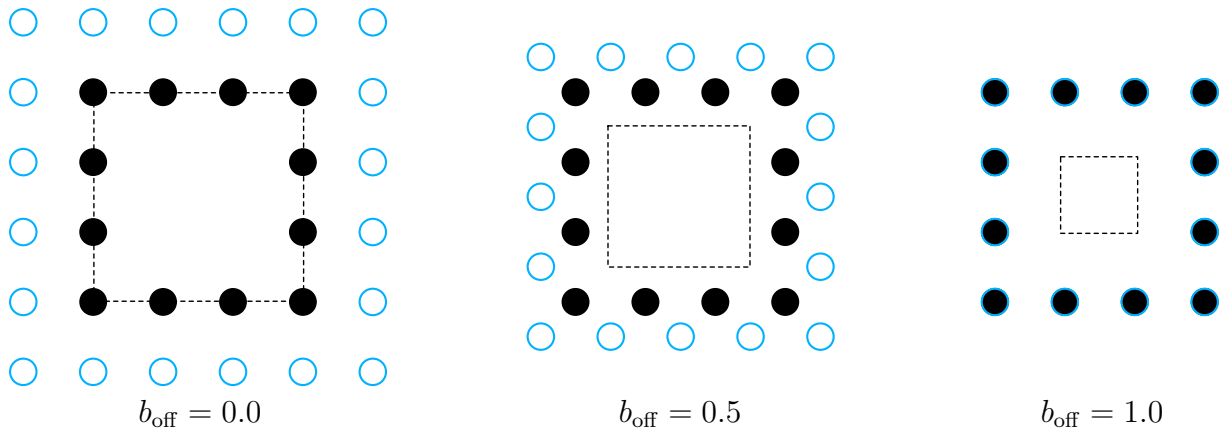


Figure 4.1: Effect of  $b_{\text{off}}$  on where boundary forces are applied from. The solid black dots are the object particles that are located on the desired boundary. The dashed lines indicate where the offset boundary is, and thus where the boundary forces on the blue fluid particles are applied from.

In this section, the boundary normals and method for calculating the free surface are investigated to determine how to accurately model physical boundaries. To do this, an untethered spherical object that matches the buoy described in Section 3.1.2 is simulated in a tank of water with various values for  $b_{\text{off}}$  (introduced in Section 3.2.4.2). When  $b_{\text{off}}$  is changed, the effective size of the sphere will change too, since the forcing on the fluid particles is measured from different locations. Figure 4.1 shows the boundary offset for three different values of  $b_{\text{off}}$ . The dashed lines indicate the offset forcing locations. The forcing on the hollow blue fluid particles keeps them approximately one particle spacing away from these forcing locations. A  $b_{\text{off}}$  of 0.0 keeps the fluid particles farther away from the boundary than when  $b_{\text{off}}$  is 1.0, and consequently the apparent size of the object is larger when the forcing is not offset. Since the buoyancy force is related to the volume of displaced fluid, these changes in apparent object size will cause variation in its buoyancy.

Each simulation was run until the untethered buoy came to rest at its equilibrium position. Two mean fluid particle spacings (5 and 10 mm) and three mean boundary particle spacings (2.5, 5, and 10 mm) were tested. Cases where the boundary particle spacing was greater than the fluid particle spacing were not tested because the fluid particles in these cases were finer than the boundary particles and could leak in to the buoy resulting in non-physical results.

#### 4.1.1 Determining the effect of boundary offset on a partially submerged buoy

The first boundary offset test simulated a spherical buoy floating partially submerged in a body of water. SPH particles were defined on the surface of a sphere of radius 0.1015 m to match the buoy used in the experiments. To ensure that the buoy was half submerged when at equilibrium,

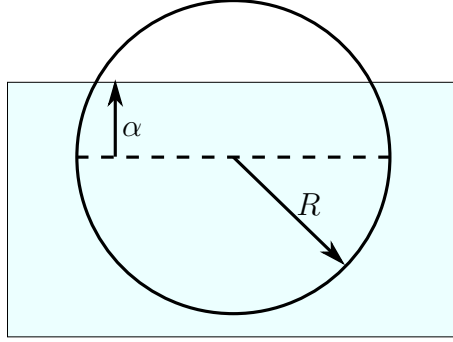


Figure 4.2: A partially submerged buoy. The dashed line indicates the height of the buoy centroid and  $\alpha$  is the vertical distance to the surface from the centroid.

the mass of the buoy was set to be equal to the mass of water that half the buoy would displace (2.19 kg).

The simulated tank of water was 0.4m wide in the  $x$  and  $z$  directions, and 0.2 m deep ( $y$ ). These tank dimensions allowed at least 10 particle spacings between the edge of the buoy and the tank wall or floor. For each combination of fluid and boundary particle spacings tested,  $b_{\text{off}}$  was varied between 0.0 and 0.6. By varying  $b_{\text{off}}$ , the effective radius of the buoy was increased or decreased, changing the buoyancy force on the buoy and thus the height that the buoy sat in the water when at equilibrium.

When the buoy was partially submerged, the volume of displaced water is given by the volume integral:

$$\begin{aligned} V(R, \alpha) &= \int_{-R}^{\alpha} \pi \left( \sqrt{R^2 - x'^2} \right)^2 dx' \\ &= \frac{\pi}{3} (2R^3 + 3R^2\alpha - \alpha^3) \end{aligned} \quad (4.1)$$

where  $R$  is the radius of the sphere, and  $\alpha$  is the distance of the fluid surface above the sphere centroid (negative when the surface is below the centre of the buoy). The surface location was calculated using the method described in Section 3.2.5 at 8 points surrounding the sphere and then averaged. Knowing the submerged volume as a function of  $\alpha$  and  $R$ , the buoyancy force can be calculated as:

$$\begin{aligned} B(R, \alpha) &= \rho g V(R, \alpha) \\ &= \frac{\rho g \pi}{3} (2R^3 + 3R^2\alpha - \alpha^3) \end{aligned} \quad (4.2)$$

The buoyancy and weight forces were the only two forces acting on the buoy at equilibrium, so the buoyancy should equal  $B_0 = 21.4839$  N. In the simulations, the surface height and vertical position of the sphere could be calculated, allowing  $\alpha$  to be easily calculated. Consequently, the

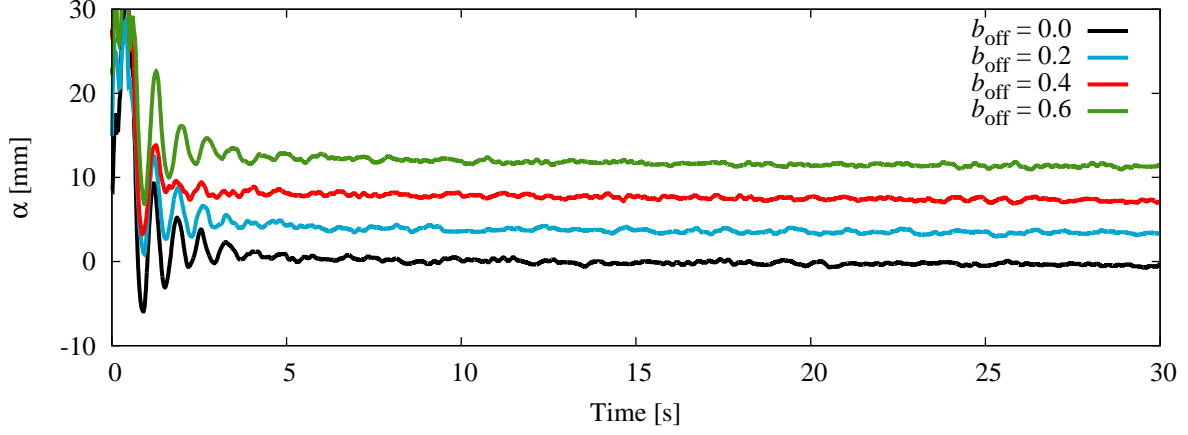


Figure 4.3: The distance of the surface above the sphere centroid ( $\alpha$ ), with mean boundary and fluid particle spacings of 10 mm. The initial disturbance was due to the fluid particles distributing themselves into a minimal energy state.

effective radius,  $R_e$ , can be calculated by solving:

$$\begin{aligned} B(R_e, \alpha) - B_0 &= \frac{\rho g \pi}{3} (2R_e^3 + 3R_e^2 \alpha - \alpha^3) - B_0 \\ &= 0 \end{aligned} \quad (4.3)$$

The effective radius can then be compared to the ‘true’ radius,  $R_T = 0.1015$ , to obtain a measure of the error:

$$\varepsilon_R = \frac{R_e - R_T}{\delta x} \quad (4.4)$$

This value of  $\varepsilon_R$  represents how much larger than expected the buoy was as a fraction of  $\delta x$ . Scaling by  $\delta x$  was chosen because  $b_{\text{off}}$  influenced the size of the buoy in proportion to  $\delta x$ .

A typical example is shown in Figure 4.3, with 10 mm mean boundary and fluid particle spacings. After a transient period, the results settled to a statistically stationary value after 10 seconds, so  $\alpha$  was calculated by taking the average after this time. Eq. (4.3) was then used to determine the effective radius,  $R_e$ , and Eq. (4.4) was used to determine the radius error for each curve.

The values of  $\varepsilon_R$  as a function of  $b_{\text{off}}$  are plotted in Figure 4.4. The plot shows that using  $b_{\text{off}}$  of approximately 0 gives an effective radius equal to the true buoy radius. This value indicates that no boundary force offset from the object particles should be set. Furthermore, the relationship between  $b_{\text{off}}$  and  $\varepsilon_R$  was 1 to 1, which was expected from the mathematical definitions of  $b_{\text{off}}$  and  $\varepsilon_R$ . The spread of the lines was quite consistent, with only the 10 mm boundary spacing simulation deviating significantly from the rest. This was likely due to insufficient resolution to accurately model the spherical nature of the buoy.

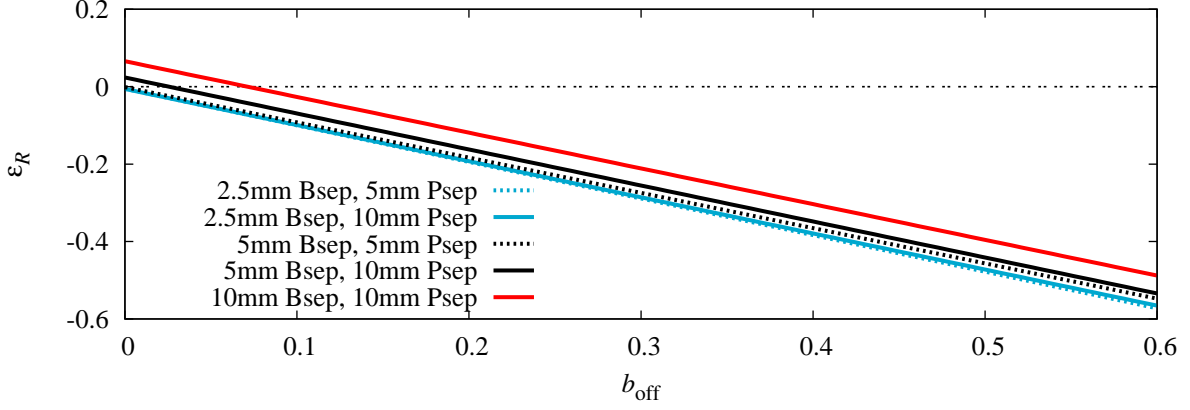


Figure 4.4: Radius error of the half submerged buoy compared to the boundary offset

#### 4.1.2 Determining the effect of boundary offset on a fully submerged buoy

In the second set of simulations, the buoy was attached to a stiff spring to keep it fully submerged. A water depth of 0.4 m was used, and the buoy centroid was initially located 0.2 m above the tank floor. The spring stiffness and length were defined to theoretically keep the buoy at its initial height. As the buoy was no longer partially submerged, the volume and effective radius were easier to calculate. The buoyancy force is related to the object radius by:

$$B = \rho g V = \frac{4\rho g \pi R^3}{3} \quad (4.5)$$

To obtain a value for the effective radius, only the buoyancy force needed to be determined from the simulation. Eq. (4.5) was then used to determine the effective radius of the buoy.

Figures 4.5 and 4.6 respectively show the trajectory and buoyancy forces on the fully submerged buoy with mean boundary and fluid particle spacings of 10 mm. The buoy trajectories shown in Figure 4.5 reached an equilibrium position around the 5 second mark. As before, the calculated effective radius was then used to determine the radius error  $\varepsilon_R$ . The radius error was plotted against  $b_{\text{off}}$  in Figure 4.7 for the fully submerged cases. The plot shows that  $b_{\text{off}} = 0.5$  is the optimal value, which contradicts the results from the half submerged case where  $b_{\text{off}} = 0.0$  was optimal.

An important difference between the two sets of simulations was that in the half-submerged case, the fluid surface played an important role in determining the effective radius of the buoy, while in the fully submerged case it was not required to be calculated. In the half submerged case with  $b_{\text{off}} = 0.0$ , the centroid of the sphere was predicted to be at the same height as the fluid surface. Figure 4.8a shows that in the  $b_{\text{off}} = 0.0$  test, the fluid surface was just above the top layer of particles. However, since there was some uncertainty in the calculation of the surface location, the fully submerged cases were more reliable. If, indeed, a  $b_{\text{off}}$  of 0.5 should be

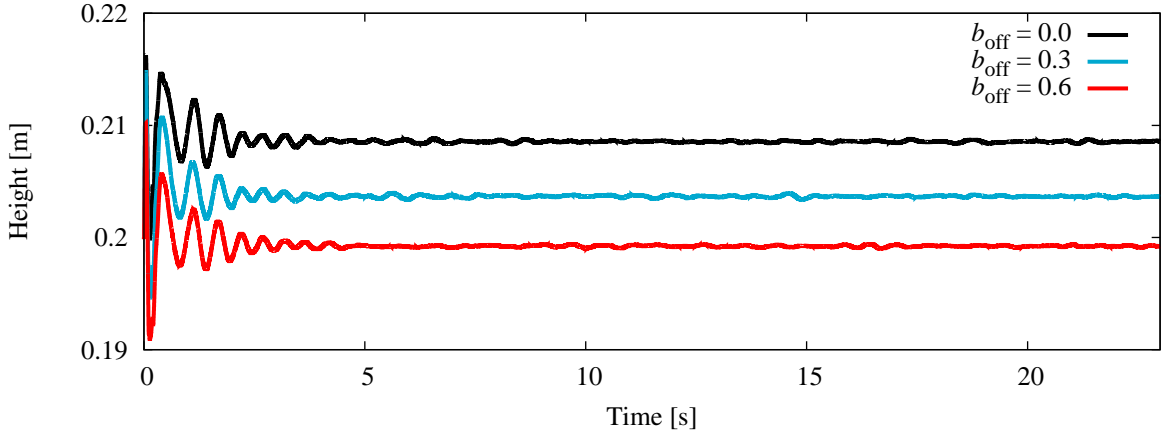


Figure 4.5: Height of the fully submerged buoy above the tank floor, with mean boundary and fluid particle spacings of 10 mm.

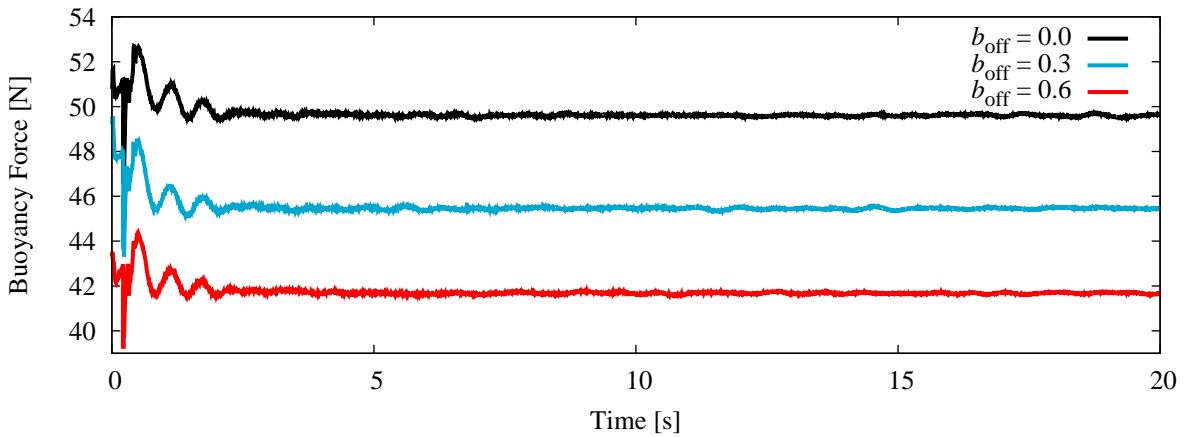


Figure 4.6: Buoyancy forces on the fully submerged buoy with mean boundary and fluid particle spacings of 10 mm.

used, then the calculation of the fluid surface location would be inaccurate. Figure 4.8b shows that when  $b_{\text{off}} = 0.6$  the centroid sits slightly lower in the water than when  $b_{\text{off}} = 0.5$ . This indicates that the surface height was below the top few layers of particles. However, since the later studies will involve objects on the surface of the water, the uncertainty in the free surface location needed to be investigated to ensure that the surface was calculated correctly, and that any errors associated with the calculation were quantified.

### 4.1.3 Calculating the free surface location

In the method used to estimate the surface height (introduced in Section 3.2.5), the value of the particle density target,  $\xi_t$ , was arbitrarily to be 0.4. By changing its value, the estimate of the fluid surface location can be modified. Consequently, a short study was performed to determine the value of  $\xi_t$  that ensured that the optimal  $b_{\text{off}}$  for both the half and fully submerged cases

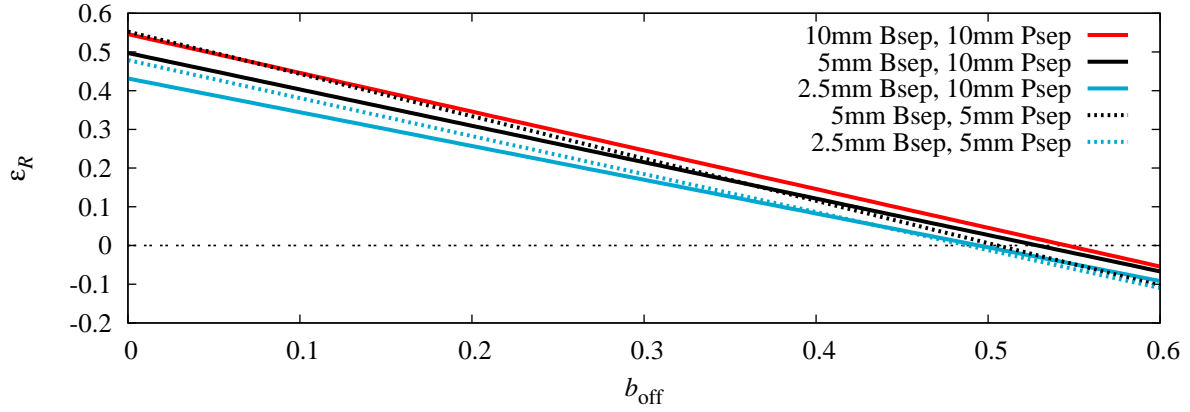


Figure 4.7: Radius error of the fully submerged buoy compared to the boundary offset.

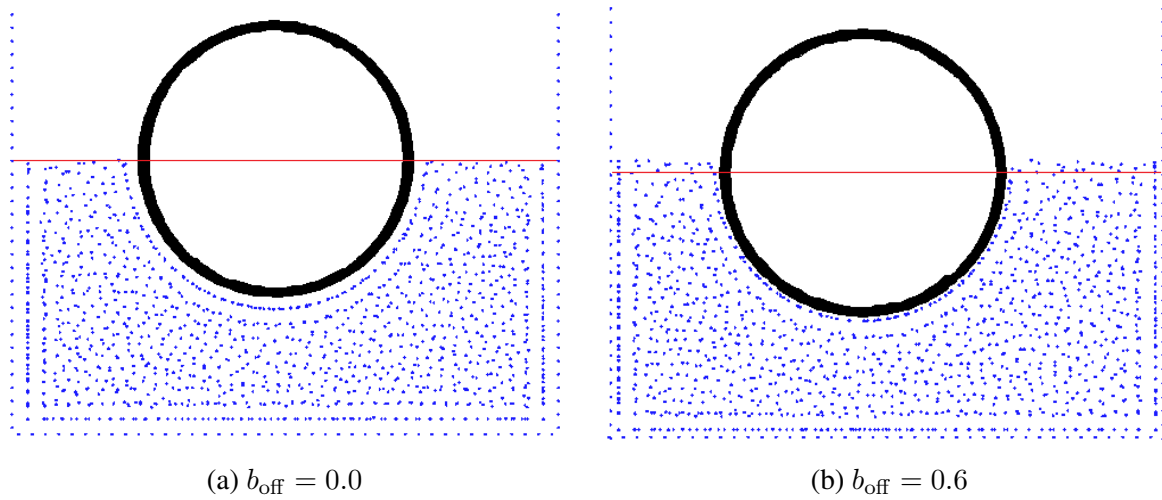


Figure 4.8: The fluid surface compared to the buoy centroid with boundary and particle spacings of 10 mm. The red line indicates the height of the centroid.

were in agreement. The half-submerged cases were repeated, using  $b_{\text{off}} = 0.5$  because that was predicted in the fully submerged case. Thus, the value of  $\xi_t$  used to predict the fluid surface location was varied to estimate which value provided the best agreement.

As in the half submerged cases, the effective radius was calculated from  $\alpha$  using Eq. (4.3) and the radius error was determined. The variation in  $\varepsilon_R$  with  $\xi_t$  is shown in Figure 4.9 for particle spacings of 5 and 10 mm, with  $b_{\text{off}} = 0.5$ . It was observed that the two curves with  $b_{\text{off}} = 0.5$  both gave zero radius error when  $\xi_t$  was approximately 0.8, irrespective of the particle resolution. From this, it was determined that a value of 0.8 should be used for  $\xi_t$ , rather than the default value described in Section 3.2.5.

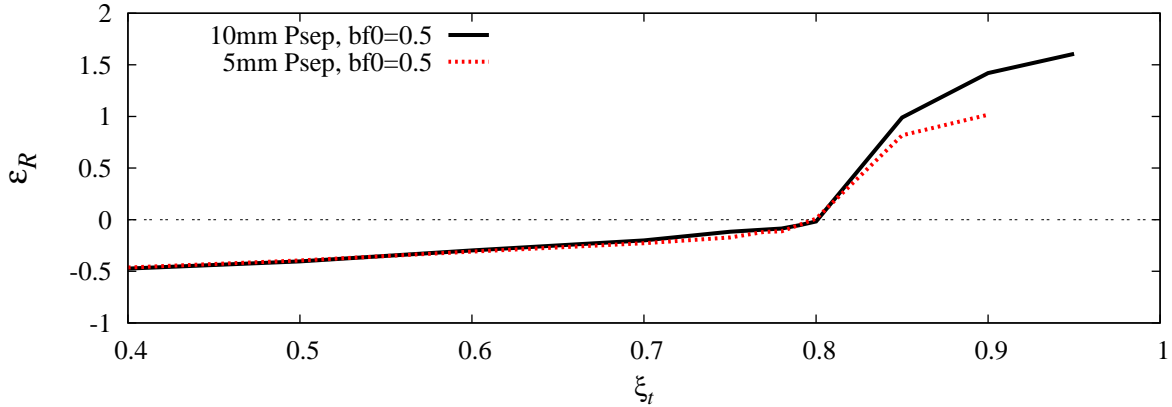


Figure 4.9: The effect of the particle density target value,  $\xi_t$ , on the estimated radius error.

## 4.2 Generating free surface waves using SPH

Generating surface waves in a wave tank simulation can be performed in a number of ways. Experimentally a piston can be used to displace the fluid at one end of the wave tank which creates surface waves that propagate along the tank. It is a simple task to replicate this piston generation method in SPH by simulating the entire tank. However, a common modelling issue is the number of particles required to perform the simulation can cause the simulation to become computationally expensive to resolve. To model the entire wave tank used in the experiments in 3D SPH would require approximately 32 million particles at a coarse particle spacing of 10 mm, and over 250 million particles at 5 mm particle spacing. Furthermore, there is nothing of interest at the end of the tank far from the piston, so resources are wasted modelling the full tank.

To reduce the number of particles, the length of the SPH domain can be shortened to cut out the unimportant regions, and artificial damping zones can be introduced to prevent reflected waves from influencing the results. However, the development region between the piston and the analysis section still needed to be modelled, and the damping zone length should be greater than the wavelengths of the waves generated (approximately 8 m for a wave with a 3 second period). This indicates that the smaller domain would still require 16 m of the tank to be modelled (a reduction of 60%), which still requires a large number of particles in 3D SPH.

An alternate method of wave generation is to utilise a spatially varying momentum source, or wave maker region. In this region, a velocity field is specified and a force applied to SPH particles inside that is a function of the deviation from the desired velocity. Since a piston is not required, it is possible to allow the end walls of the domain to be periodic and the waves to continually re-enter the domain. To ensure a continuous wave train across the domain, the length of the domain must be an integer number of wavelengths. This has the added benefit that waves entering the wave maker region will be in phase, so that the fluid particles will have

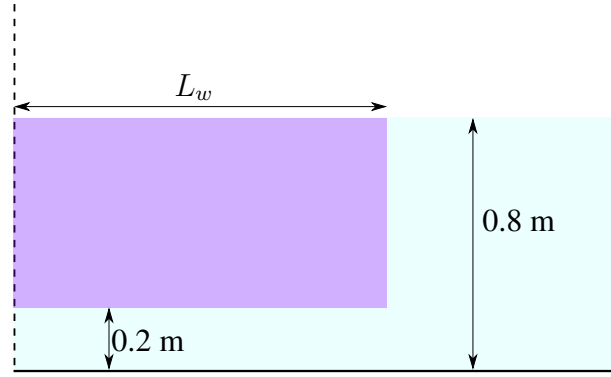


Figure 4.10: The wave maker region shown as purple and the periodic boundaries by dashed lines. The wave maker region length,  $L_w$ , is an input parameter. Note that the figure is not to scale.

velocities close to the specified velocity field, and require little or no artificial forcing. However, it does require the velocity field to be known analytically so it is not suitable for all types of waves (for example the NLS breather solutions discussed in Section 2.1.3 cannot be produced using this wave maker region).

In the simulations, the length of the forcing region,  $L_w$ , does not span the entire  $x$  domain because it must leave a space for the waves to freely interact with any floating objects that were to be studied. This region was also not set to span the entire  $y$  domain, rather it started at a short distance above the floor and stopped at the mean surface level (see Figure 4.10). This was to ensure that the particles near the floor or free surface crests were not forced normally to either the floor layer or the surface.

#### 4.2.1 Wave generation algorithm

The general methodology for wave generation was given in Rudman and Cleary (2016), and a brief description of the method is included in this section. To generate the waves a velocity field of the fluid is required. The velocity field chosen here is given by the intermediate depth linear water wave solution (Young, 1999):

$$v_x = \frac{agk}{\omega} \frac{\cosh ky}{\cosh kd} \cos \psi \quad (4.6a)$$

$$v_y = \frac{agk}{\omega} \frac{\sinh ky}{\cosh kd} \sin \psi \quad (4.6b)$$

$$v_z = 0 \quad (4.6c)$$

where  $a$  is the wave amplitude (mean-to-peak),  $g$  is gravitational acceleration,  $k$  is the wave number ( $= 2\pi/\lambda$ ),  $\omega$  is the angular frequency ( $= 2\pi/\tau$ ),  $d$  is the depth to the mean surface level, and  $\psi = kx - \omega t$ .

The wave maker region aims to force the fluid particles within it toward a velocity given by Eq. (4.6). To do this, a force is applied to the particles in the region that is proportional to the difference between the specified velocity,  $\mathbf{v}_c = (v_x, v_y, v_z)$ , and the particle velocity,  $\mathbf{v}_i$ :

$$\mathbf{F} = 10^\kappa \mu_i \frac{\mathbf{v}_c - \mathbf{v}_i}{\rho_i} \quad (4.7)$$

where  $\kappa$  represents the forcing factor of the wave maker region (an input parameter) that determines how strongly the fluid particles are controlled to match the specified velocity field. In practice, the period,  $\tau$ , is specified and the wave number,  $k$ , (and hence the wavelength  $\lambda$ ) is calculated using the dispersion relationship:

$$\omega^2 = gk \tanh kd \quad (4.8)$$

In this study, the period was the desired input variable, so Eq. (4.8) was solved for  $k$  using the Newton-Raphson root-finding technique, and the length of the SPH domain is set to be an integer multiple of the corresponding wavelength. Consequently, for waves of different desired periods, SPH simulations with different domains were required.

## 4.2.2 Determining the particle spacing

An issue with using a periodic domain arises from the particle searching algorithm described in Section 3.2.2. The length of the domain in the periodic domain, denoted in this section as  $L$ , is required to be divided into an integer number of cells,  $n$ :

$$L = n \cdot 2h = 2n \cdot h_f \cdot \delta x \quad (4.9)$$

Furthermore to ensure fluid continuity over the periodic boundary the length must also be an integer number of particle spacings,  $m$ :

$$L = m \cdot \delta x \quad (4.10)$$

Combining Eq. (4.9) and Eq. (4.10) gives:

$$m = 2n \cdot h_f \quad (4.11)$$

In this study,  $h_f = 1.2$ , thus  $m = 2.4n$ .

To ensure that  $m$  was an integer, in Eq. (4.11)  $n$  must be a multiple of 5 ( $n = 5p, p \in \mathbb{N}$ ). Therefore, from Eq. (4.9),  $L = 10p \cdot h_f \cdot \delta x$ . Given that  $L$  was set to be an integer number of

wavelengths and  $p$  was also an integer,  $\delta x$  needed to be specially calculated by first determining:

$$p = \left\lfloor \frac{L}{10 \cdot h_f \cdot \delta x^*} \right\rfloor \quad (4.12)$$

where  $\delta x^*$  is the desired particle separation and the  $\lfloor \rfloor$  brackets indicate the floor/round-down operation. The exact particle spacing  $\delta x$  could then be calculated as:

$$\delta x = \frac{L}{10 \cdot p \cdot h_f} \quad (4.13)$$

### 4.2.3 Wave generation calibration

The waves generated in Rudman and Cleary (2016) were created by moving the wave generator region through the domain, adding momentum to the fluid particles so that they matched the region's velocity. The region was then disabled, which released the collected particles as a large wave to crash over their structure. Although the method here is similar to Rudman and Cleary's, it is different in two aspects.

Firstly, the region here is not moving, and secondly we prescribed a velocity field that varied over time. Previously, the linear water wave solutions have not been used in SPH to define a velocity field, and there was a need to ensure that the approach generated waves that agreed with the desired waves.

If the forcing region was implemented appropriately then the imposed velocity field should, in theory, provide a wave of exactly the amplitude and period specified. However, the effect that the input parameters (forcing factor,  $\kappa$ , and the region length,  $L_w$ ), and the specified wave amplitude and period, have on the generated wave needed to be understood. Consequently, a number of simple calibration tests were performed to test the sensitivity of the generated waves to the four inputs.

These tests were performed using 2D SPH simulations of a wave tank, with water depth of 0.8 m. A period of either 1 or 3 seconds was used for the wave generation throughout these simulations. For the 1 s waves the SPH domain was 4.67 m long (three wavelengths), while for the 3 s waves, the domain length was 7.90 m (one wavelength). The desired particle spacing was 10 mm, but was modified by the process in Section 4.2.2 to be 10.24 mm for the 1 second period tests, and 10.13 mm for the 3 second period tests.

The first case performed here investigated how well the wave maker approach was able to generate waves for different input amplitudes. A forcing factor of 6.5 was used and the wave maker region was 1 m long. Three input amplitudes of 7, 9, and 11 cm were simulated for each of the two periods (1 and 3 seconds). Figures 4.11 shows the free surface elevation for the different input amplitudes in the case of the 1 second wave, while Figure 4.12 shows the same

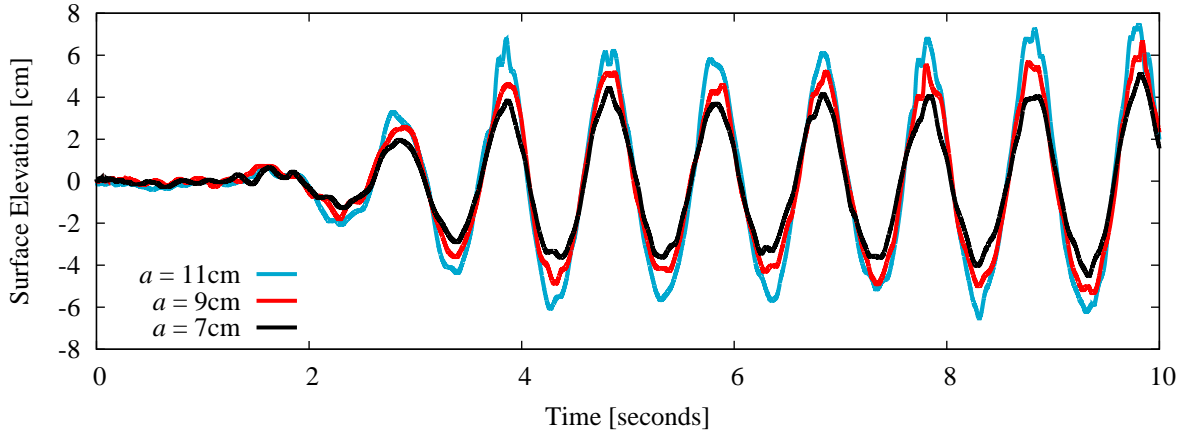


Figure 4.11: Comparison of waves produced with various input amplitudes at a period of 1 second. The legend indicates the specified input amplitude,  $a$ , for the simulation.

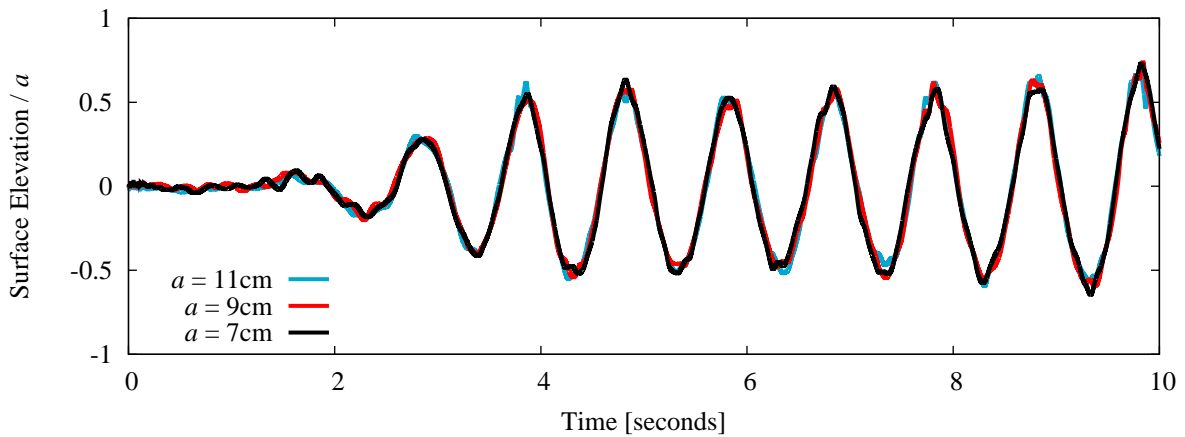


Figure 4.12: Comparison of waves produced with various input amplitudes at a period of 1 second, relative to the desired wave amplitudes. The legend indicates the specified input amplitude,  $a$ , for the simulation.

waves relative to the specified amplitude. Figure 4.13 shows similar results for the 3 second period wave, although the amplitudes are closer to the desired amplitude. From the plots, it could be observed that all of the waves have smaller resulting amplitudes in SPH simulations than those specified by the input amplitude, and the amplitude of the resulting wave was linearly related to the desired amplitude.

In SPH, the fluid particle spacing was an important parameter that influenced the accuracy of the simulation. To observe the effect that the particle spacing had on the generated wave, additional simulations were performed for each wave period using a particle spacing of 5 mm, and specified wave amplitude of 7 cm. After modification, the final particle spacings were 5.05 mm and 5.03 mm for the 1 and 3 second periods respectively. Figures 4.14 and 4.15 indicate that the amplitude of waves generated in a 5 mm particle spacing fluid domain do not differ significantly from the waves generated in a 10 mm particle spacing domain for either the 1 or 3 second period waves. There is, however, some noise in the 10 mm particle spacing

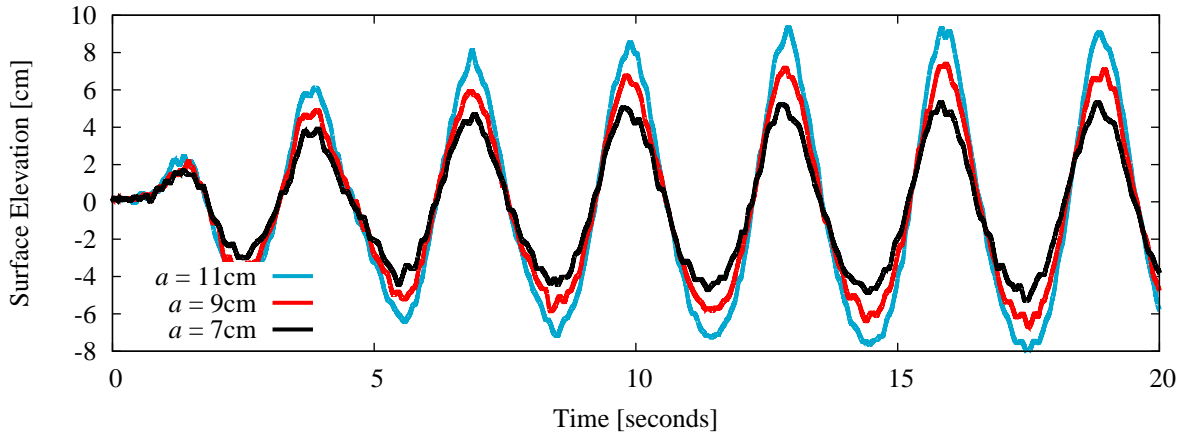


Figure 4.13: Comparison of waves produced with various input amplitudes at a period of 3 seconds. The legend indicates the specified input amplitude,  $a$ , for the simulation.

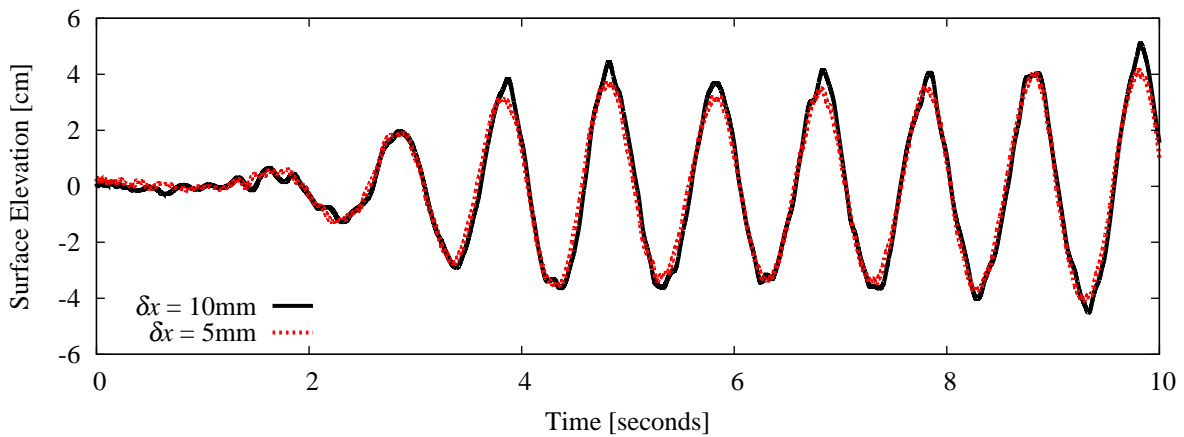


Figure 4.14: Comparison of waves produced at different particle spacings. The waves here have a specified wave amplitude of 7 cm and period of 1 second. The legend indicates the particle spacing.

simulations that was less prevalent in the 5 mm particle spacing simulations.

The forcing parameter,  $\kappa$ , was assigned a value of 6.5 by default. Larger values amplified the magnitude of the forces in the wave maker region, causing the fluid particles to match the specified velocity field more quickly. Figure 4.16 shows the surface elevation of a number of wave trains generated with an amplitude of 7 cm and period of 1 second at a particle spacing of 10 mm, but with varying values of  $\kappa$ . For larger  $\kappa$  values, the amplitudes of the generated waves exceeded the desired amplitude. Additionally, large values of  $\kappa$  increased the magnitude of the forces applied to the fluid particles, which could result in smaller time-steps and longer simulation runtimes.

Finally, a number of simulations were performed to investigate the effect of the length of the wave maker region on the amplitude of the generated waves. The generated waves were specified to have an amplitude of 7 cm and period of 1 s, and a forcing factor of 6.5. Three simulations

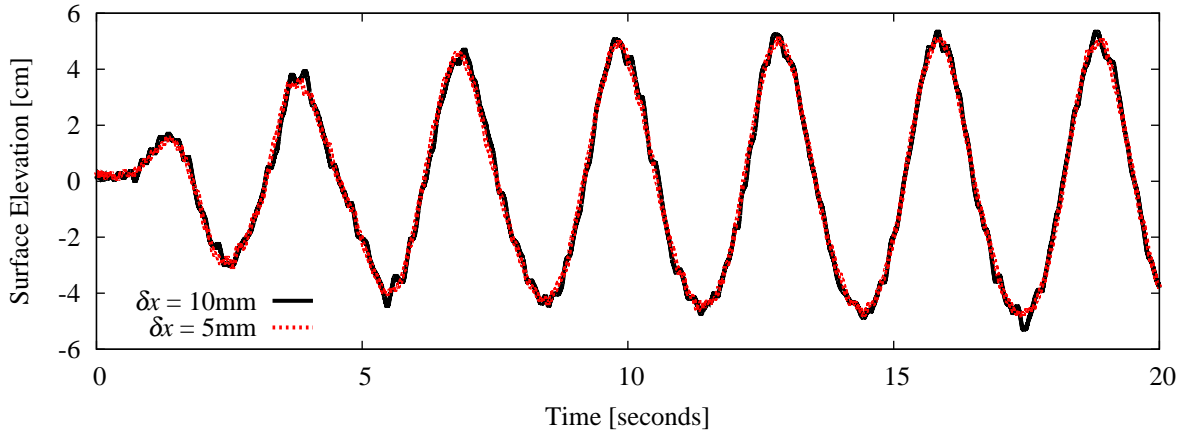


Figure 4.15: Comparison of waves produced at different particle spacings. The waves here have a specified wave amplitude of 7 cm and period of 3 second. The legend indicates the particle spacing.

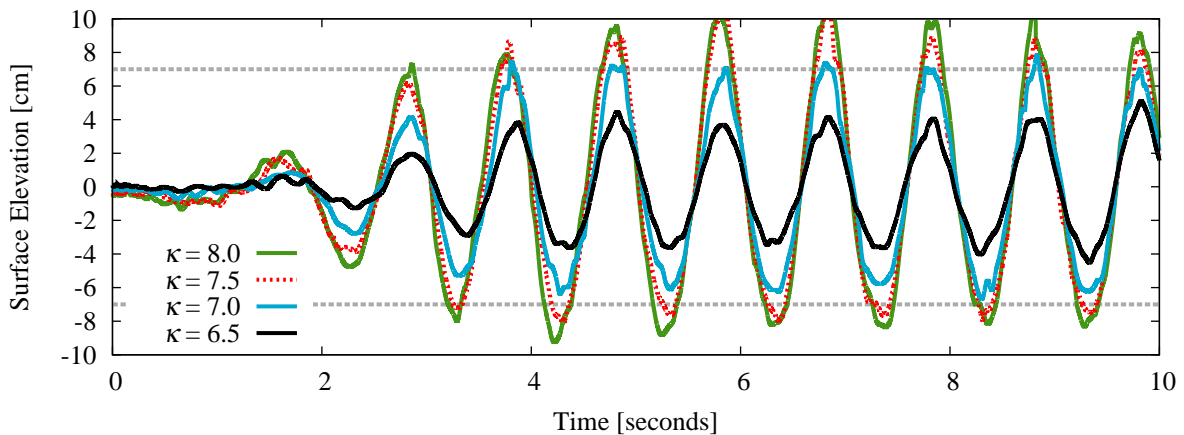


Figure 4.16: Comparison of waves produced with different forcing factors. The waves here have a specified wave amplitude of 7 cm and period of 1 second. The legend indicates the forcing factor used, and the horizontal dashed lines indicate the desired limits of the surface elevation (i.e., amplitude of 7 cm).

using wave maker lengths of 1.0, 1.5 and 2 m were compared, and the results are shown in Figure 4.17. The waves produced by the longer wave makers were slightly larger in amplitude. This could be attributed to the additional time that the waves spent in the wave maker region.

From these simulations, it was clear that the specified size of the wave maker and forcing factor have an influence on the waves generated. Ideally, longer wavemaker regions should be used so larger forcing factors are not needed. In summary, the forcing factor appeared to have a more significant influence on the amplitude of the generated waves than the wave maker length.

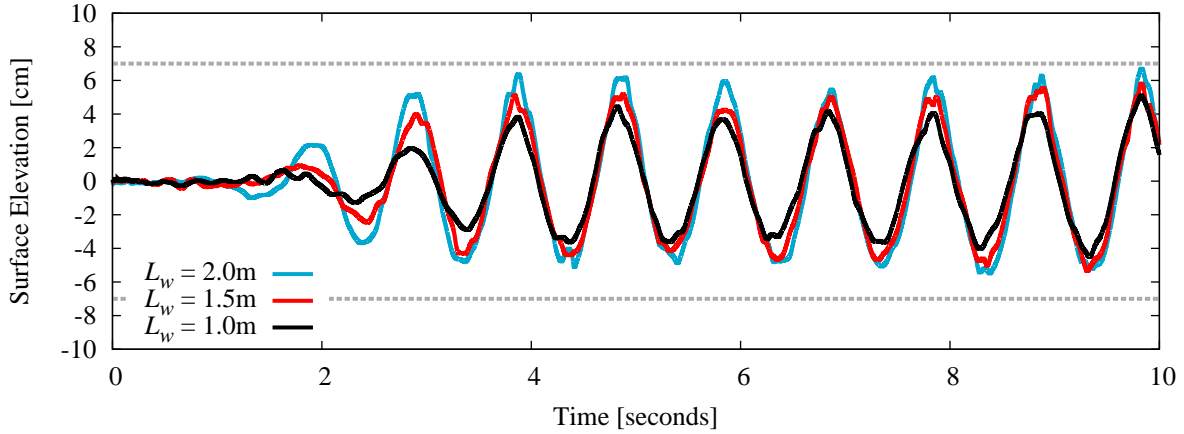


Figure 4.17: Comparison of waves produced with different wave maker region lengths. The waves here have a specified wave amplitude of 7 cm and period of 1 second. The legend indicates the length of the wave maker region, and the horizontal dashed lines indicate the desired limits of the surface elevation (i.e., amplitude of 7 cm).

### 4.3 Summary

In summary, two investigations on the two major technical issues in SPH have been presented and discussed. The first investigation explored the key parameters for determining object boundaries and free surface locations, and the second explored an alternate method for producing free surface waves. Regarding the boundary and free surface models, the optimal boundary offset value,  $b_{\text{off}}$ , for object and wall boundaries was found to be 0.5 (equivalent to half a particle spacing) and the free surface location was the point where the number density,  $\xi_t$ , was 0.8.

When producing surface waves using a forcing region, the length of the region and its degree of control have the most significant influence on the waves produced. In future work, it is recommended that a forcing factor of  $\kappa = 7.0$  be used, and the maximum allowable length of the wave maker region is used.

The primary limitation of this method of generating free surface waves was that it required the velocity field to be known as a function of time and space. For simple sinusoidal wave trains, the velocity field is well known, and this method is able to accurately generate surface waves, but for more complex waves, additional measurements or calculations may be required to obtain the velocity field. Later in this study, a Peregrine breather wave will be considered; however, only the surface elevation will be defined and the velocity field is not explicitly known. Consequently, the forcing region method described here cannot be used to model those types of waves. Instead, these waves must be modelled using a similar to experiments, such as using a piston to generate the waves.

## Chapter 5

# Modelling the interaction between a buoy and a free surface

A number of SPH studies have investigated free surface interactions with a boundary. Of these, only a few explored wave interactions with floating tethered bodies. One such study explored the interaction of a large wave on a tethered body Rudman and Cleary (2013, 2016), but they did not provide any comparisons to experimental data to verify their results. Other studies by Patel et al. (2009) and Campbell and Vignjevic (2012) simulated a floating body in a series of waves using SPH. While both studies provided verification of their method, the comparisons were done with 2D simulations, and therefore cannot be readily applied to 3D models without further research.

The existing validation work on SPH in other applications (i.e., sloshing or dam break problems) provides some support for the validity of using SPH to model a tethered buoy. However, the data required for validation tests at larger scales, such as full scale offshore structures, is difficult or impossible to obtain. Validation tests of these applications at smaller scales would provide better evidence to support simulations at large scales and can give an estimate of the errors.

In this chapter, two validation cases will be explored, comparing experiments to matching SPH simulations. In the first, a tethered spherical buoy is displaced from rest in one of two directions (vertically underneath the fluid surface, or horizontally along the surface) and is then allowed to return to its equilibrium position. For the second case, the tethered buoy is impacted by a wave train. These simple validation studies provide an understanding of the requirements needed to produce an accurate prediction of a floating tethered object interacting with a free surface. Additionally, they will provide an estimate of the degree of accuracy associated with the simulation. This will allow rules-of-thumb to be obtained that relate this estimate of accuracy to particle spacing (and other input parameters).

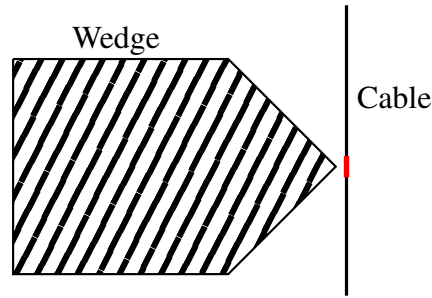


Figure 5.1: The release mechanism for the Vertical Oscillation tests. The red mark on the cable is pressed against the point of the wedge to ensure that the release height remains consistent between repetitions.

## 5.1 Oscillatory motion of a spherical buoy

The first validation case investigated the vertical and horizontal oscillations of a tethered spherical buoy (described in Section 3.1.2) when released from a non-equilibrium. These experiments were then reproduced in SPH simulation to investigate the capability of SPH to predict the buoyancy, drag, and spring forces on the buoy, and to understand what is required to obtain accurate results.

### 5.1.1 Vertical oscillation of the buoy

Using the setup described in Section 3.1.2, the spherical buoy was pulled under the surface, completely submerged, and then released to return to a rest position. The cable was pulled and pressed against a fixed wedge above the tank, as shown in Figure 5.1. A mark on the cable (shown in the figure as a red mark) identified the location where it would be pressed against by the point of the wedge. This ensured a consistent release position in each run of the experiments. The cable was then released and the resulting vertical oscillation trajectory of the buoy was measured using the motion tracking method (discussed in Section 3.1.4). The experiment was repeated six times and the results were averaged.

The trajectories of the six runs are shown in Figure 5.2 to be very consistent. For the first oscillation, the six experiments were nearly identical, and slight differences could be seen at the troughs of each oscillation. After the third trough, the differences became more noticeable.

The differences from the mean trajectory (see Figure 5.3) show that the individual trajectories were all within 3 mm of the mean until after the fourth peak. Compared to the range of the initial oscillation, each experiment repetition had a maximum error of less than 3% of the initial peak motion.

Since the buoy was oscillating through the surface, the submerged frontal drag area was con-

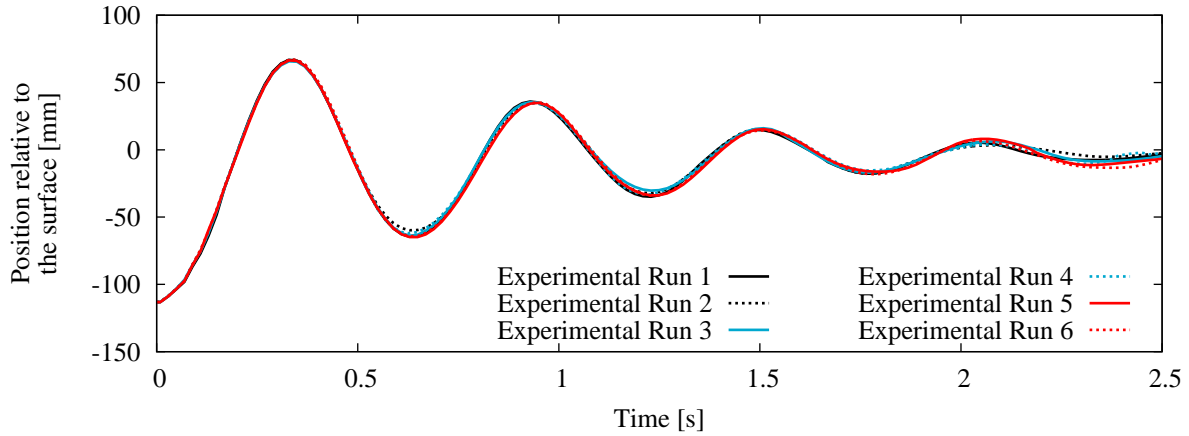


Figure 5.2: Experimental trajectories of the vertically oscillating buoy

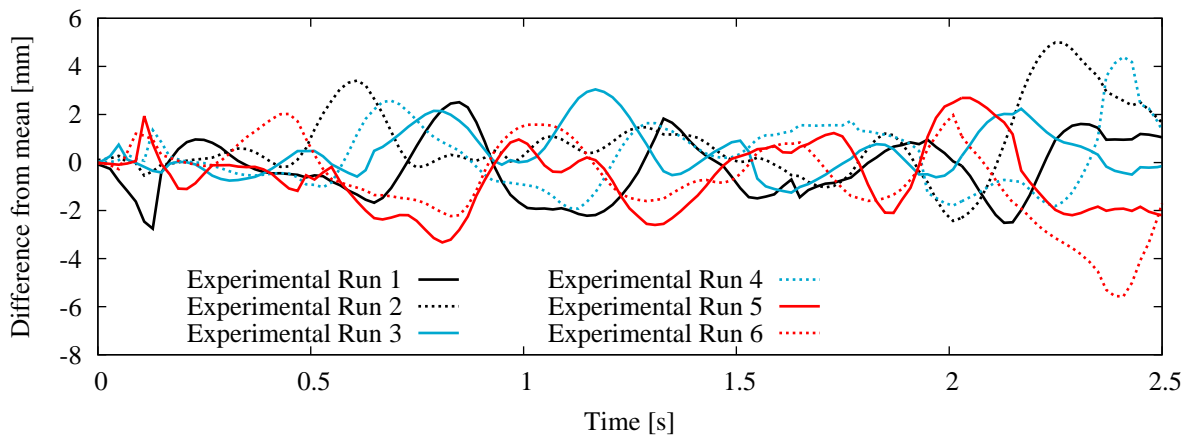


Figure 5.3: Difference of experimental trajectories of the vertically oscillating buoy from the mean trajectory

stantly changing as the buoy moved, so estimating a natural frequency using simple theories was difficult. To obtain an estimate of the natural frequency of oscillation the period between the peaks of the buoy's trajectory was measured. A mean period of 0.6 seconds was measured from the peaks in Figure 5.2, which was equivalent to a natural frequency of 1.67 Hz.

The experiments were reproduced using SPH simulations with different particle spacings: 10 mm, 5 mm, and 2.5 mm, equivalent to approximately 20, 40, and 80 particle spacings across the buoy diameter. The buoy was placed at the same initial depth as the experiments with the same spring stiffness and initial extension. The simulations were performed in a  $1 \text{ m} \times \text{m}$  wide tank in order to reduce the total number of particles, and hence computational expense.

Figure 5.4 shows a comparison between the vertical trajectories of these simulations and the experimental mean. With a particle spacing of 10 mm the agreement was poor. The amplitude of the first oscillation was in error by 35%, and the period had approximately 15% error.

A time sequence of images from the first oscillation are shown in Figure 5.5, where a side view

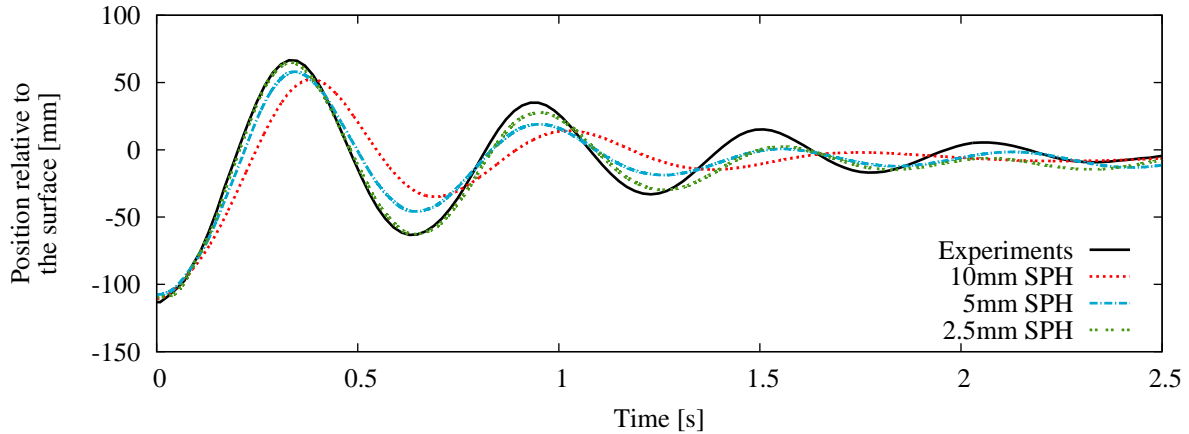


Figure 5.4: The vertical trajectories of a vertically oscillating buoy.

of the experiments are provided on the left, and a slice through the 10 mm particle spacing simulations was taken at  $z = 0$  (with slice thickness of 10 mm). The frame at  $t = 0.2$  s was the closest to when the buoy is half submerged in the initial rise, the frame at  $t = 0.4$  s was the closest frame to the buoy's peak position, and the frame at  $t = 0.7$  s was the closest frame to when the buoy is at the first trough of its motion. The buoy's position from  $t = 0.0$  to  $0.4$  s shows reasonable agreement between the experiments and simulations, but at  $0.7$  s the buoy had penetrated deeper into the water in the experiments. Some fluid particles were observed to still be on top of the buoy at  $0.2$  s, and at  $0.4$  s the simulation predicted that there was a crest against the bottom of the buoy that was absent in the experiment.

Refining the particle spacing to 5 mm (also shown in Figure 5.4) improved the period agreement significantly (to within the experimental variation expectations) and the amplitude error decreased to 15%. Further refinement to 2.5 mm showed that the amplitude was within 2% and the period remained within experimental variation. However, each of the simulations showed amplified damping of the motion beyond the first oscillation. This was greater than expected.

An internal report by CSIRO has shown that particle disorder in the vicinity of an oscillating object can dissipate significant amounts of energy (Cleary, private communication) and that this was the most likely cause of the additional damping observed in these simulations.

It was clear that improving the particle resolution gave significantly better results. However, the 2.5 mm particle spacing simulation (the buoy diameter was approximately 80 particles) required in excess of 50 million particles for this small test case. However, this simulation required over 11 weeks of wall-time using 12 processors and 48 GB of memory. The computational expense at such resolution was infeasible for most applications, and larger simulations become impractical even for research purposes until computing hardware developments have been made or massive parallel versions of the code are developed.

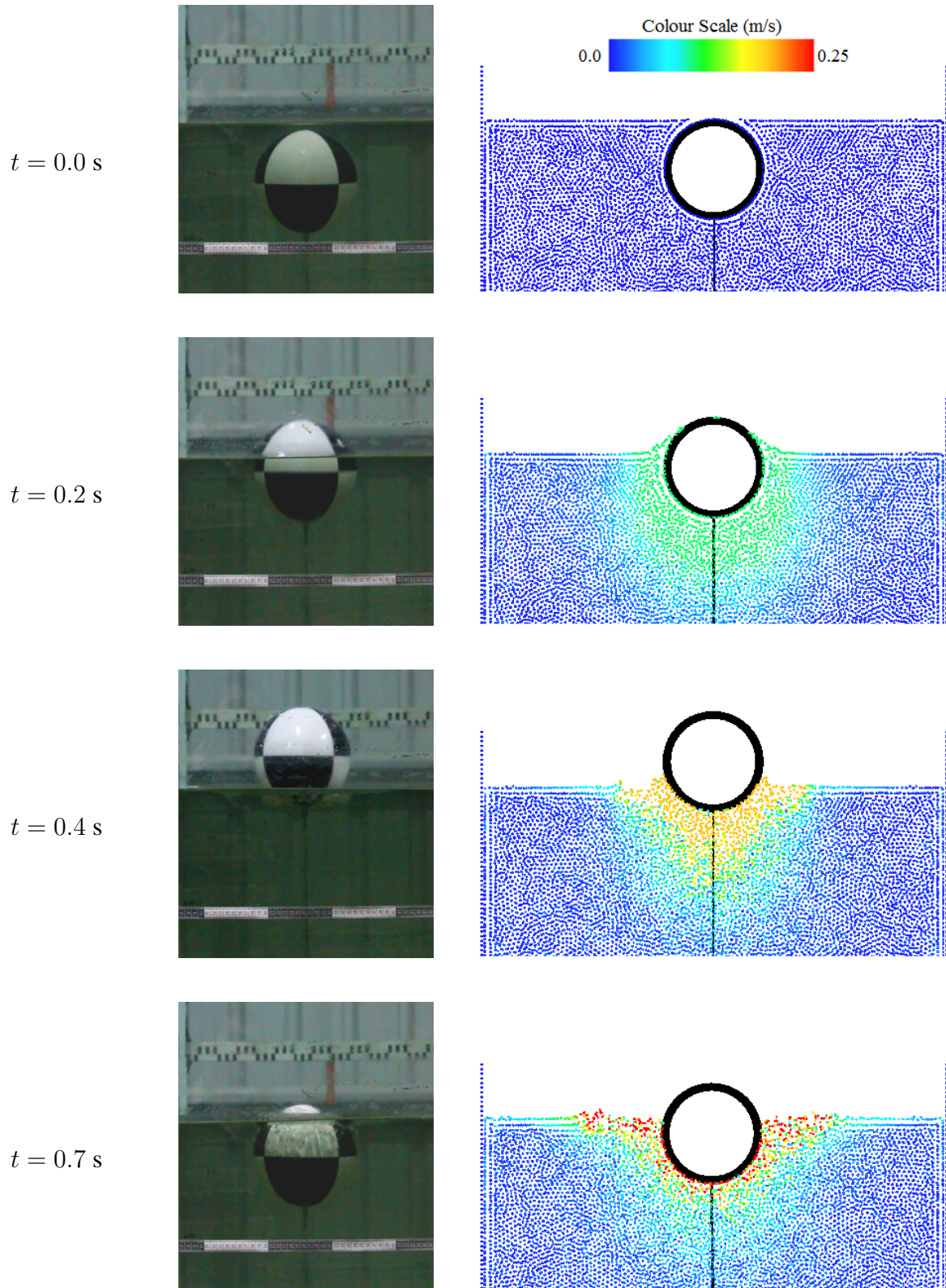


Figure 5.5: A visual comparison between the experiments (left) and simulations with 10 mm particle spacing (right) for the Vertical Oscillation tests. The simulation particles have been coloured based on velocity magnitude (blue is 0 m/s, red is greater than 0.25 m/s).

### 5.1.2 Horizontal oscillation of the buoy

A second oscillation test case was performed, displacing the buoy horizontally rather than vertically. Using the same setup, the buoy was pulled approximately 0.5 m horizontally across the surface of the water. The buoy was then released and allowed to freely return to its equilibrium position. The point of release was, however, inconsistent as no apparatus for ensuring consistency was developed, resulting in a mean starting position of  $50.8 \pm 2.0$  cm from its equilibrium position. As in the vertical oscillation tests, the mean trajectory of the buoy was measured across 6 runs. The variance of the starting position caused the amplitude of oscillation to increase or decrease according to how far the buoy was initially offset, but negligible effect was observed on the period of oscillation.

Two SPH simulations were performed, one with 10 mm particle spacing, and another with 5 mm particle spacing. In these simulations, a domain of length 2 m, width 1 m, and fluid depth of 0.8 m was modelled. Since the domain had been doubled compared to the vertical oscillation tests, there were double the number of particles. Furthermore, these tests required simulation times of at least 12 seconds (nearly 5 times as long), so these simulations required approximately 10 times as much wall-time to sufficiently complete. For these reasons, the 2.5 mm particle spacing was omitted from this test case as it was infeasible given the computational constraints.

The mean trajectory in the experiments, and the simulated trajectories using SPH are shown in Figure 5.6. For a mean particle spacing of 10 mm, the motion was quickly damped out, indicating that, like the vertical tests, the damping was over predicted by SPH. For the 5 mm particle spacing simulation, the amplitude of the initial oscillation was in very good agreement, but the amplitude of the first peak was approximately 15% in error. This magnitude of error, resulting from the damping, was consistent with the errors observed in the vertical oscillation tests for the same particle spacing. If the 2.5 mm particle spacing simulations were feasible to perform, it could be hypothesised that the errors would improve to 2%, as was observed in the vertical oscillation case.

The time to the first peak was in good agreement for all of the tests performed. However, the numerical damping in the SPH simulations caused the following troughs and peaks to become out of phase. Again, it could be hypothesised that the period of oscillation would improve at finer resolutions. As in the vertical case, the time between the peaks of the experimental trajectory, as well as the time between troughs, were measured. The average period was found to be 5.2 seconds, corresponding to a frequency of oscillation of 0.19 Hz.

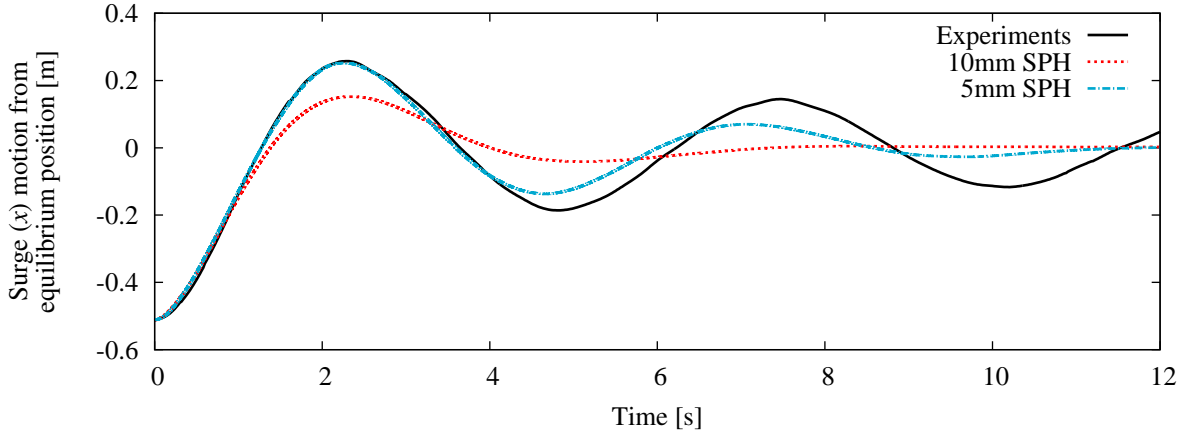


Figure 5.6: Buoy displacement in the horizontal direction for the horizontal oscillation test.

### 5.1.3 Summary

In the two oscillation cases explored here, it was apparent that additional numerical damping was present in the simulations. At finer particle resolutions, the numerical damping decreased significantly. For the coarsest resolution test, where the particle spacing was  $1/20^{\text{th}}$  of the buoy diameter, the amplitude of the initial oscillation was approximately 35% in error in both directions of motion. When the particle spacing was reduced to  $1/40^{\text{th}}$  of the diameter, this error decreased to 15%. At the finest resolution tested,  $1/80^{\text{th}}$  of the diameter, the amplitude error was only 2%, however, this test was only conducted for the vertical oscillation. The computational expense involved in the  $1/80^{\text{th}}$  test is significant, and this, therefore, limits its feasibility for using this resolution in future applications. In summary, coarser particle spacings can be used in future simulations as long as the magnitude of error for these spacings are duly considered in the analysis of the simulations. A particle spacing of  $1/40^{\text{th}}$  of the body diameter appears to be a reasonable compromise between accuracy and computational expense, and leads to errors of the order of 15%.

## 5.2 Wave Train cases

While the simple oscillation tests were useful for determining how well SPH can model the interaction with the fluid surface, the final goal of modelling a rogue wave interaction with a tethered ship requires that the interaction between simple waves and the buoy be validated. To perform these validations and interactions with the buoy, the Monash Wave Tank was used to generate single frequency wave trains with periods of either 1, 2, or 3 seconds in water of 80 cm depth. The experimental results are then compared with SPH simulations. The 1 second period wave was chosen as it provided waves that were classified as deep water waves ( $kd > \pi$ ), while the 2 and 3 second period waves provided intermediate depth waves ( $\pi/10 < kd \leq \pi$ ). A

shallow water wave would require a wavelength of 16 m, or a period of 5.8 seconds, and this would require very long stroke lengths of the piston in the experiments. Additionally waves of this length need a 16 metre long SPH domain, which was currently infeasible (as discussed in Section 4.2). Consequently, the 3 second period wave is the longest wavelength used here, and it provided  $kd \approx \pi/5$ , which was reasonably close to a shallow wave.

The wave trains interacted with the buoy setup (Figure 3.3), located 1.5 metres from the piston end of the working section (see Figure 3.1). The same spring was used as in the previous experiments (with stiffness of 30.88 N/s), and the untensioned length was set to ensure that the buoy was half submerged when at rest. The motion tracking technique was applied to measure the response of the buoy to the waves.

### 5.2.1 Non-dimensionalisation

Young (1999) gave the following formula for the trajectory of fluid particles in linear waves based on linear wave theory. The position of a fluid particle,  $(\chi, \zeta)$ , measured from the mean position  $(x, y)$  was given by:

$$\chi = \frac{agk \cosh ky}{\omega^2 \cosh kd} \cos(kx - \omega t) \quad (5.1a)$$

$$\zeta = \frac{agk \sinh ky}{\omega^2 \cosh kd} \sin(kx - \omega t) \quad (5.1b)$$

where  $a$  is the mean-to-peak wave amplitude. Using the dispersion relationship,  $\omega^2 = gk \tanh kd$ , and measuring particles on the surface (i.e.,  $kd = ky$ ), these equations became:

$$\chi = \frac{a}{\tanh kd} \cos(kx - \omega t) \quad (5.2a)$$

$$\zeta = a \sin(kx - \omega t) \quad (5.2b)$$

For small values of  $kd$ ,  $\tanh kd \approx kd = 2\pi d/\lambda$ . Consequently, we choose to non-dimensionalise the measured trajectories by the coefficients of  $\cos$  and  $\sin$  in Eq. (5.2):

$$x^* = \frac{(x - x_e)d}{a\lambda} \quad y^* = \frac{y - y_e}{a} \quad t^* = \frac{t - t_0}{\tau} \quad (5.3)$$

where  $(x_e, y_e)$  is the resting position of the buoy,  $a$  is the amplitude of the incident wave train,  $\tau$  is the wave period, and  $t_0$  is the time that the first fully developed crest reaches the buoy. There is no motion in the  $z$  direction, and thus it is not considered.

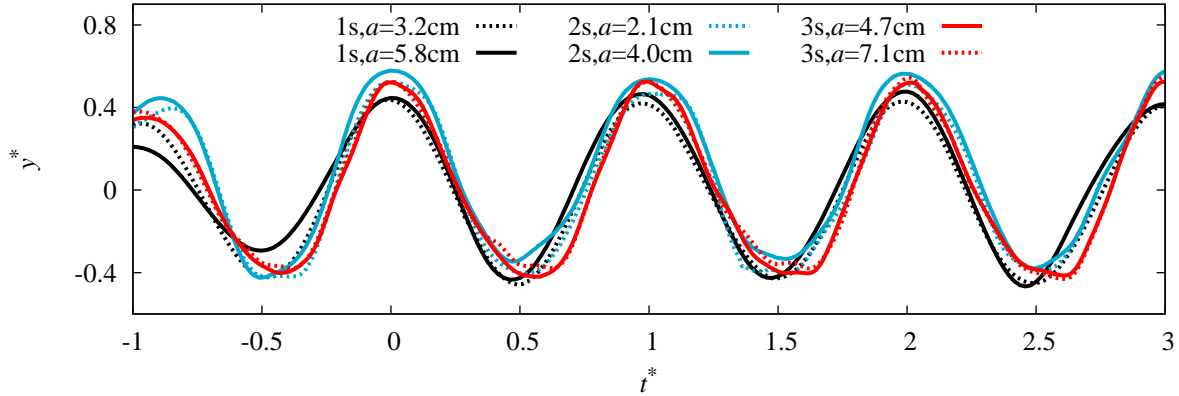


Figure 5.7: Non-dimensionalised heave trajectories of the buoy centroid in the wave train experiments. The legend indicates the period and amplitude of the incident wave trains

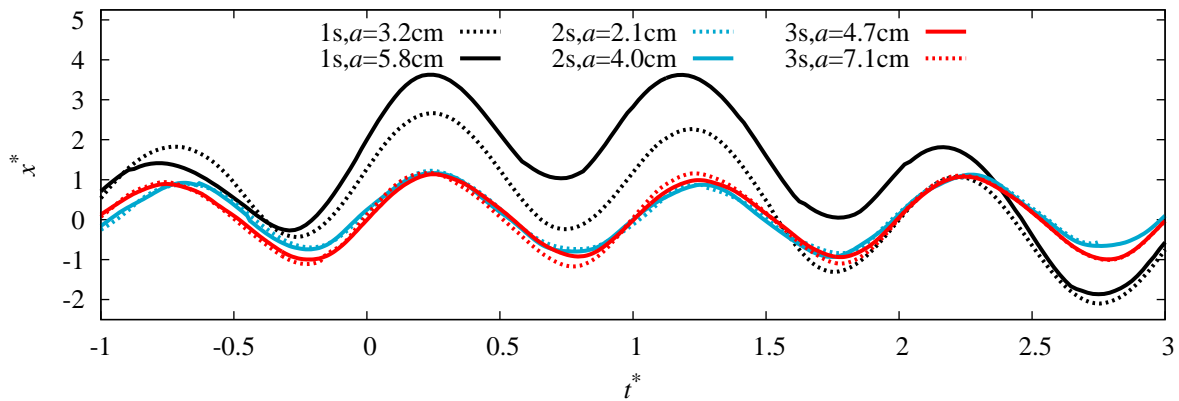
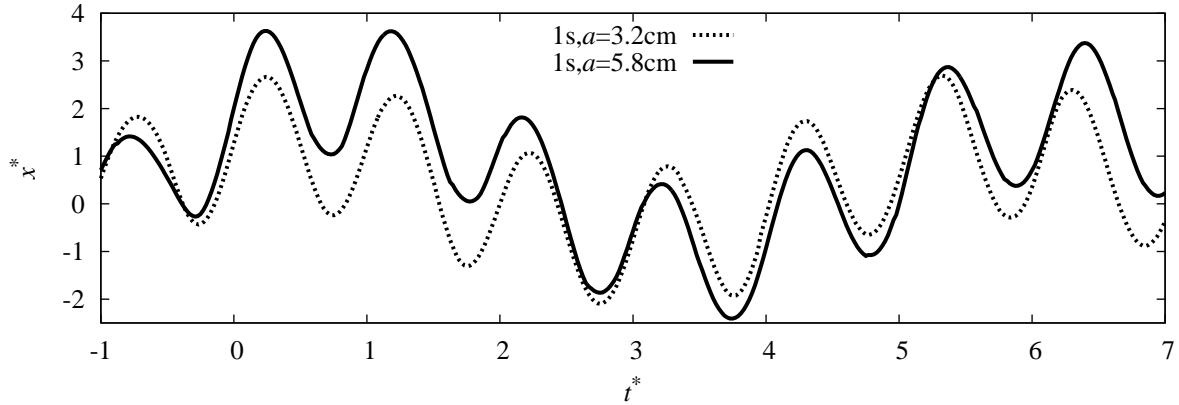


Figure 5.8: Non-dimensionalised surge trajectories of the buoy centroid in the wave train experiments. The legend indicates the period and amplitude of the incident wave trains.

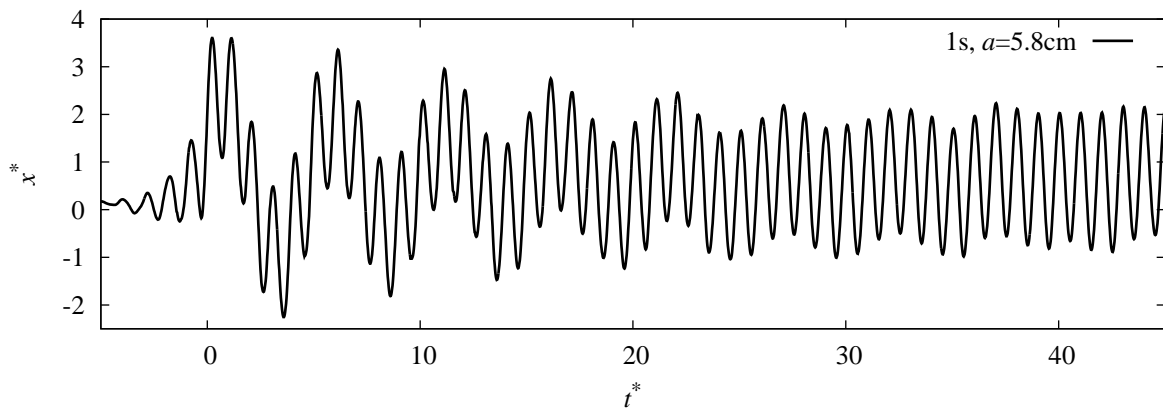
## 5.2.2 Experimental trajectories of the buoy

Figure 5.7 shows the non-dimensionalised heave ( $y^*$ ) trajectories of the sphere under the influence of each of the wave trains. The trajectories for different periods match reasonably well in the time domain, and this was expected due to the time scaling in Eq. (5.3). After time 0 (where all of the waves were at their first full-sized peak), the amplitude of the buoy trajectories were within 10% of each other, indicating that the non-dimensionalised heave motion was insensitive to the period and amplitude of the waves. However, the troughs of the 3 second period experiment with 7.1 cm amplitude have some disturbances. This may have been due to the larger displacement of the buoy resulting in the spring becoming unloaded and allowing the cable to become slack.

The corresponding non-dimensionalised surge ( $x^*$ ) trajectories for the sphere are shown in Figure 5.8. The non-dimensionalised trajectories in the 2 and 3 second period waves were in close



(a) Both amplitude wave trains for a full period of the large amplitude modulation.



(b) The full non-dimensionalised time series of the wave train case with 1 s period and 5.8 cm amplitude.

Figure 5.9: Surge trajectories of the sphere centroid in the 1 second wave train experiments for (a) both amplitudes over an extended time period, and (b) the 5.8 cm amplitude case for the entire recorded time.

agreement with each other, however, the 1 second period cases revealed a large offset motion that resulted in poorly matched amplitudes compared to those of the 2 and 3 second period cases, especially for the 5.8 cm higher amplitude. Figure 5.9a shows the 1 second cases over a longer time frame, indicating that the offset motion was due to a low frequency modulation. To understand the cause of this motion, the full time series of the 5.8 cm amplitude case, shown in Figure 5.9b, was analysed. The buoy trajectory showed that this modulation significantly reduces in amplitude after a few oscillations, indicating that the modulation was a transient start-up effect, or initial transient motion.

In addition to the modulation, the surge position of the buoy did not average to zero. Since  $x^* = 0$  corresponds to when the buoy was at the resting position, this indicates that there was a mean constant force on the buoy that was offsetting it. For the 5.8 cm amplitude wave case, the buoy's mean position was located at  $x^* = 0.5$ , which corresponded to a net displacement of 8.86 cm and a cable angle of approximately  $7^\circ$  from the vertical. The tension in the cable at this

position was 4.535 N with 0.566 N in the horizontal component. Since the buoy typically moves in the direction of the wave when ascending up the front of an incoming wave, and opposite to the wave when descending down the back, it experiences the frontal slope of the wave for the majority of the interaction. This slope causes the buoyancy force on the buoy to not be just vertical, and since the buoy endures the front slope more than the back slope there will be a net horizontal buoyancy force on the buoy. Given that the vertical buoyancy force on the buoy was 21.48 N, a net horizontal buoyancy of 0.566 N was reasonable.

This offset was only significant for the 1 s period case, and was negligible or not present in the 2 and 3 s cases. This was most likely due to two factors. First, the waves in the 2 and 3 s cases were not as steep as in the 1 s case, thus the buoyancy force on the buoy will have a smaller horizontal component. Secondly, while the buoy may still endure the frontal slope of the wave for the majority of the time, proportionally it endures the frontal slope for a smaller amount of time than in the 1 s case.

A frequency analysis of the 1 second period case with 5.8 cm amplitude was performed over the full time series and is shown in Figure 5.10. The surge frequency spectra, shown in Figure 5.10a, shows a large peak at 1 Hz, corresponding to the frequency of the incident wave train. There was also a peak at approximately 0.19 Hz, which was the natural frequency of oscillation that was observed in the horizontal oscillation tests that were performed earlier (shown as the vertical dashed blue line in the figure). This result indicates that the modulation was an initial transient motion of the buoy, caused by the initial few waves displacing the buoy horizontally, and then the motion came from the buoy attempting to return to equilibrium. The heave frequency spectra, in Figure 5.10b, shows the same large peak at the wave train frequency, however, there was no peak at the natural frequency of oscillation. Small peaks were also observed at 2 and 3 Hz in both frequency spectra, however, these are resonance frequencies of the wave train.

### **5.2.3 Simulated buoy interactions with a wave train**

The wave train and buoy interactions were replicated using SPH. As discussed in Section 4.2, the SPH domain needed to be reduced so that a feasible number of particles were used and the non-critical regions of the domain located far from the buoy are not modelled. Earlier, it was recommended that the length of the wave-making region should be as long as possible. For a period of 1 second, the buoy was observed to have a maximum displacement of 0.45 m in the 5.8 cm amplitude experiment. So, to ensure that the simulated buoy did not cross the periodic boundary, nor did it enter the forcing region, its centroid must be located at least 0.6 m from both (accounting for the radius of the buoy). As the tank length needed to be an integer multiple of the wavelength, 1.56 m for a 1 s period, the tank length was set to 4.67 m to ensure that a long enough wave maker could be included, while also leaving sufficient length of space for the

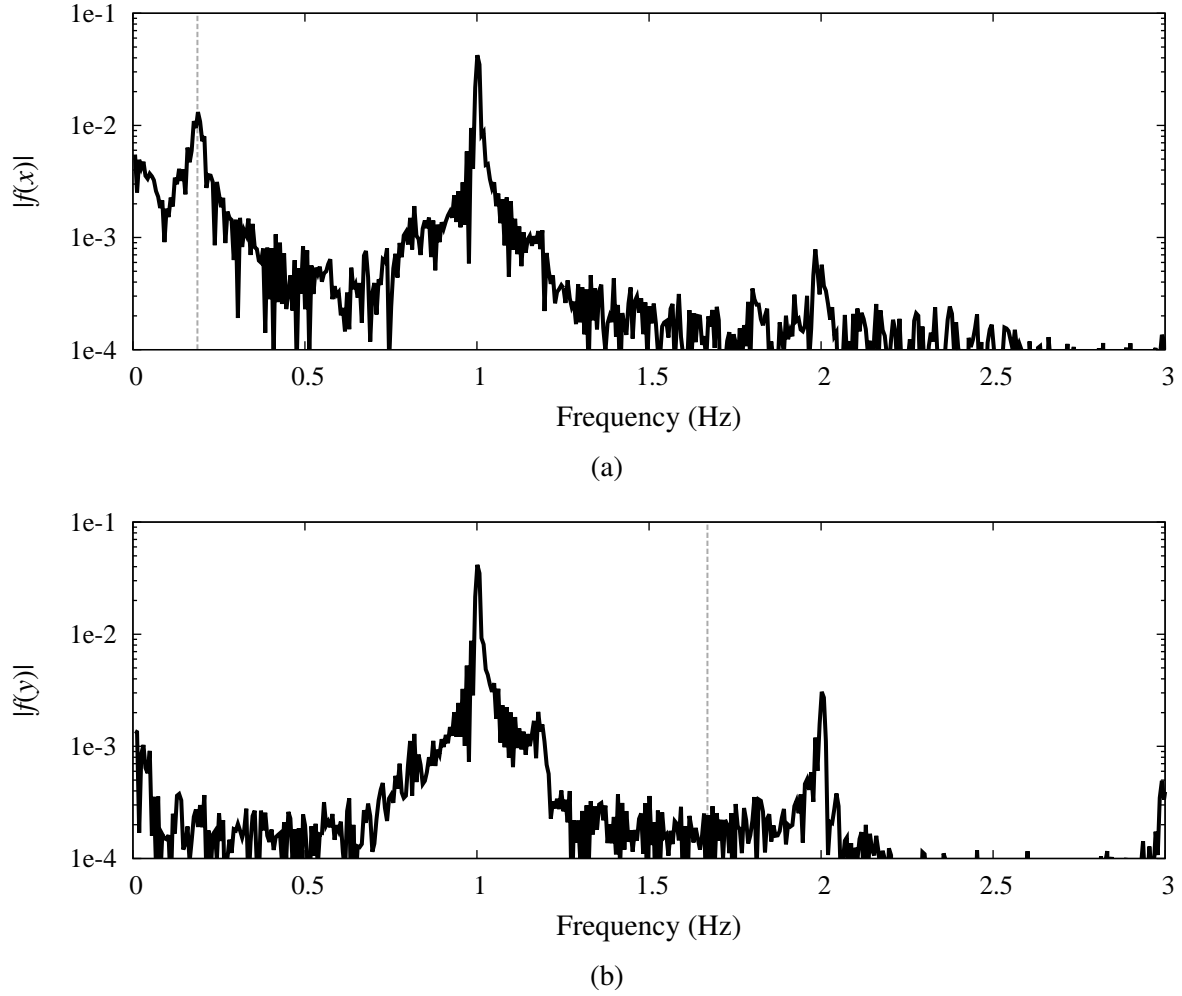


Figure 5.10: Frequency spectra of the 1s wavetrain case with amplitude 5.8 cm in the (a) surge direction and (b) heave direction. The vertical dashed blue lines indicates the respective natural frequency obtained from the oscillation tests performed in Section 5.1.

buoy to oscillate in without interfering with the wave maker.

For the 1s wave period case, the buoy was placed at  $x = 3.8$  m and the wave maker length was set to 3 m allowing 1.6 m for the buoy to oscillate. The SPH domains for the 2 and 3 second cases were determined similarly, but the tank length was set to be a single wavelength long. The lengths used are summarised in Table 5.1. In all of the simulations performed in this section, the forcing factor used in the wave maker region,  $\kappa$ , was set to 7.0 (refer to Section 4.2.3).

The first wave train case discussed here is the 1 second period case, where a simulated amplitude

Table 5.1: Wave maker lengths used

Period (s)	Tank Length/ $\lambda$	Tank Length (m)	Wave maker length (m)
1	3	4.67	3.0
2	1	4.85	3.5
3	1	7.90	6.0

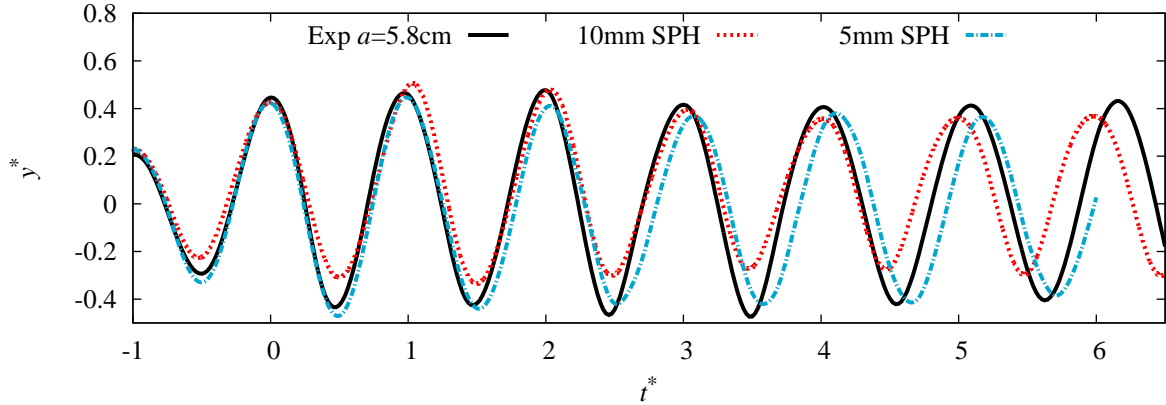


Figure 5.11: Non-dimensionalised heave motion of the buoy in the experiments and simulations with a 1 second period wave train.

of 5.8 cm was specified and compared to the 5.8 cm amplitude experiment. Two numerical wavetanks of length 4.669 m, width 1 m, and depth 0.8 m were set up for a mean particle spacing of 10 mm (requiring 3.87 million particles), and for a mean particle spacing of 5 mm (approximately 30 million particles).

Figures 5.11 and 5.12 show the heave and surge motion comparisons respectively. The amplitude parameter in the wave maker region was set to 5.8 cm, and the resulting waves had amplitudes of approximately 5.5 cm. The non-dimensionalisation in Eq. (5.3) used the actual amplitude of the waves and not the specified amplitude.

For the heave motion in Figure 5.11, the amplitude of the simulated motion with 10 mm particle spacing was under-predicted by 15% over the first two periods, increasing to 25% afterwards. Additionally, after  $t^* \approx 4$  there was a phase error of 16% introduced. For the 5 mm simulation, the amplitude of motion was in better agreement with the experiments.

In the surge motion, the initial transient motion was present in both simulations though its amplitude in the 10 mm simulation was about half that of the experiment. This transient motion was more heavily damped in the SPH simulations, and this was consistent with the excessive damping observed in the horizontal oscillation cases. In the 5 mm simulations, the damping of these motions was less, and as shown in Figure 5.12, the transient motion was in better agreement with the experiments, with an error of approximately 10%.

Consequently, the differences between SPH and experimental results is believed to be due to the damping that was observed earlier. A visualisation of the simulation with 10 mm particle spacing is shown in Figure 5.13, with the fluid particles coloured by  $v_x$  and pressure. The buoy is shown at times  $t^* = 0.1, 0.9$  s, and 1.5.

Since there is only a single period of the transient motion available, a traditional Fourier analysis of the data is not feasible. Instead, a short time Fourier transform (STFT) was used to perform a

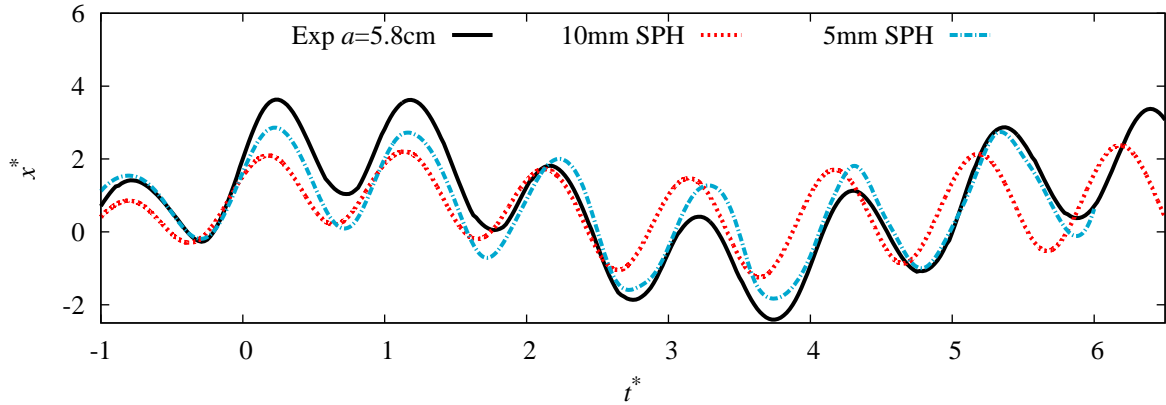


Figure 5.12: Non-dimensionalised surge motion of the buoy in the experiments and simulations with a 1 second period wave train.

frequency analysis of the 10 mm simulation, using the *spectrogram* function available in MATLAB specifically. The 5 mm simulation was not included as there was not enough data for the STFT to provide meaningful results. Although the small amount of time data limited the resolution of the analysis, the surge frequencies in Figure 5.14 clearly revealed two peaks that almost matched the wave frequency and the natural frequency of oscillation. The heave frequencies in Figure 5.15 show that, like in the experiments, the only peak was near the frequency of the waves.

The wave trains with periods of 2 seconds were similarly simulated using a mean particle spacing of 10 mm. Due to the excessive number of particles required in the 5 mm case, an excessive wall time was required, so this resolution was not used for wave train of this period or longer. The amplitude was set at 4 cm to match the amplitude of the larger experimental case, but the simulated waves were approximately 3.8 cm in amplitude. Figures 5.16 and 5.17 show the surge and heave motion of the buoy in response to this simulated wave in comparison to the experimentally measured trajectories. The amplitude of the surge motion was under-predicted by 25% with a 5% phase error, while the heave motion was in closer agreement with the experiments having an amplitude error of 15% and a phase error of 2%.

Finally, waves with a period of 3 seconds were simulated by SPH and compared to the experimental results. An amplitude of 7.1 cm was specified in the wave maker region, and the resulting waves had an amplitude of 6.8 cm. The amplitude of the surge motion, shown in Figure 5.18, was under-predicted by 21%, and the trajectory was out of phase by 12%. Conversely, the heave motion, shown in Figure 5.19, was more accurately predicted, with an error of 12% in amplitude and less than 1% error in phase.

The simulated wave train interactions with the spherical buoy indicated that the buoy's heave trajectory was more accurately predicted by SPH than the surge trajectory. The primary force that determines the vertical position is the buoyancy and weight of the buoy, which, as seen in

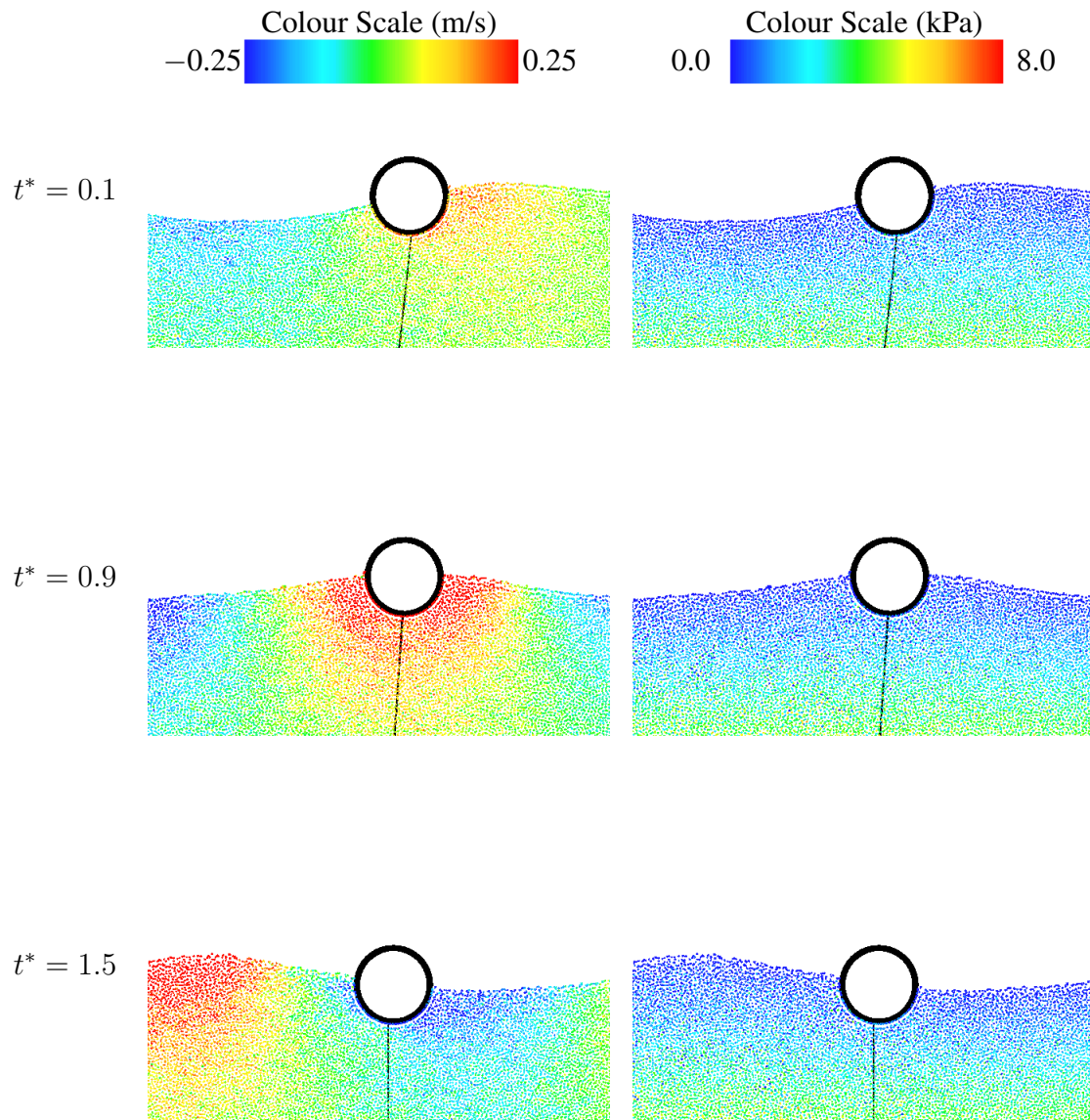


Figure 5.13: Visualisation of the simulated buoy in a 1 s wave train with 10 mm particle spacing. The figures show a slice through the midplane of the tank. The particles on the left have been coloured by their speed in the  $x$ -direction, and the particles on the right have been coloured by their pressure.

Section 4.1, can be accurately modelled using SPH. In the surge motion, the force on the buoy is the drag from the fluid particles. The first wave that interacts with the buoy imposes a transient response from the buoy as it is offset from the equilibrium position. The horizontal oscillation case showed that SPH does not accurately predict the transient motion at coarse particle spacings, and the surge trajectories of the buoy responding to the 2 and 3 second period waves also shows that the first peak is smaller than the following oscillations. For the 1 second period case, the initial transient motion is more accurately predicted when a finer resolution of 5 mm particle spacing is used although the transient motion is under-predicted. Consequently, it can be concluded that the particle spacing in SPH plays an important role in accurately predicting

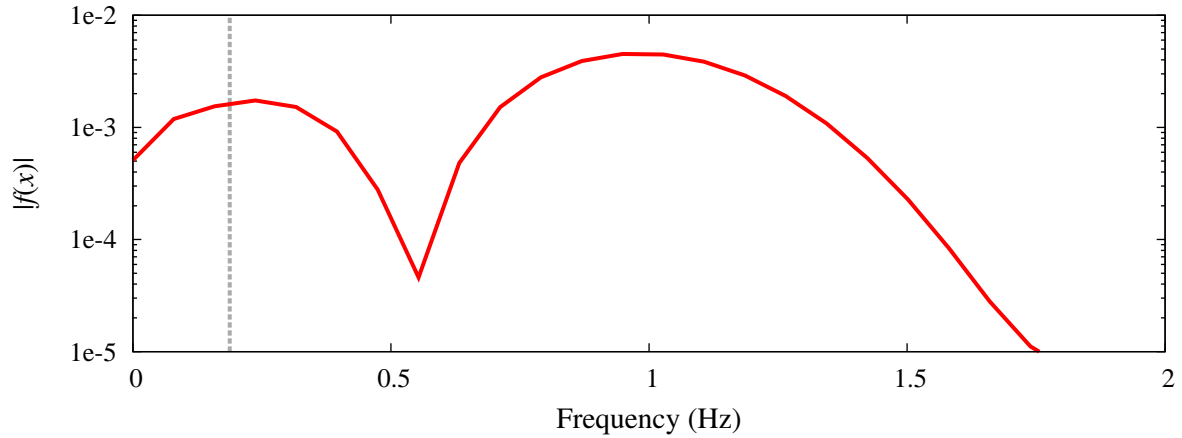


Figure 5.14: Short time frequency spectrum of the surge motion of the simulation with 1 second period and 10 mm particle spacing. The vertical grey line indicates the horizontal natural frequency obtained from the oscillation tests performed in Section 5.1.

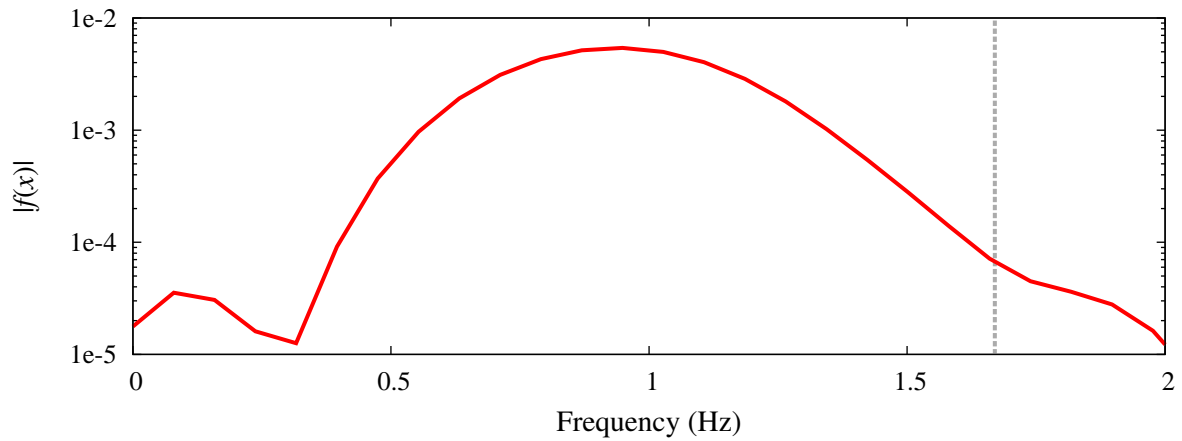


Figure 5.15: Short time frequency spectrum of the heave motion of the simulation with 1 second period and 10 mm particle spacing. The vertical grey line indicates the vertical natural frequency obtained from the oscillation tests performed in Section 5.1.

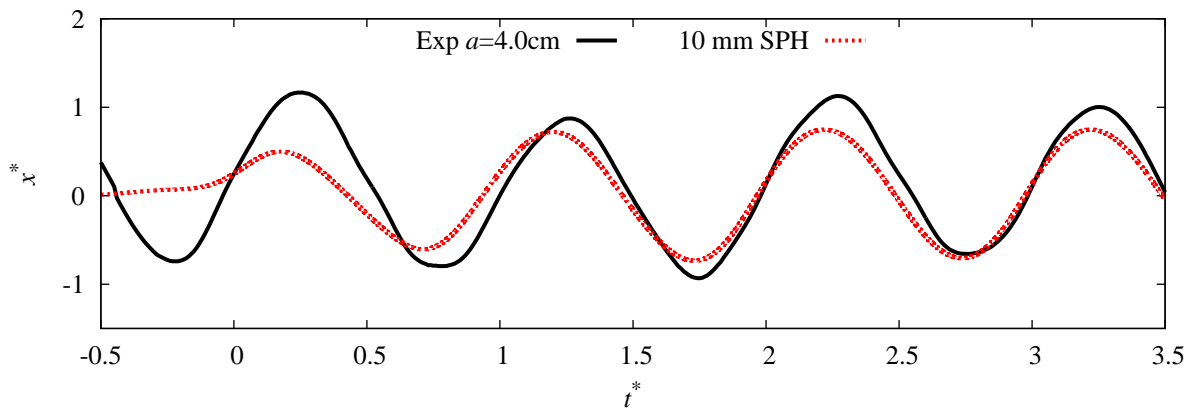


Figure 5.16: Non-dimensionalised surge motion of the buoy in the experiments and simulations with a 2 second period wave train.

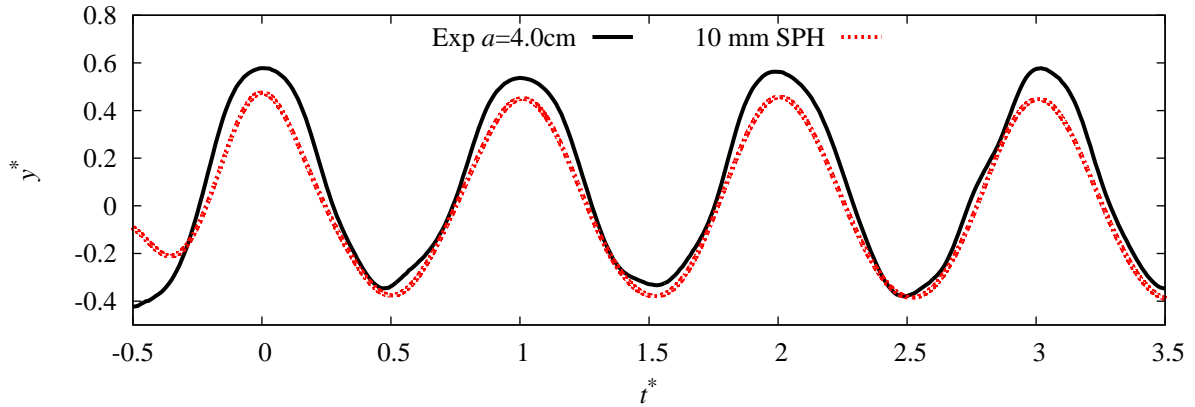


Figure 5.17: Non-dimensionalised heave motion of the buoy in the experiments and simulations with a 2 second period wave train.

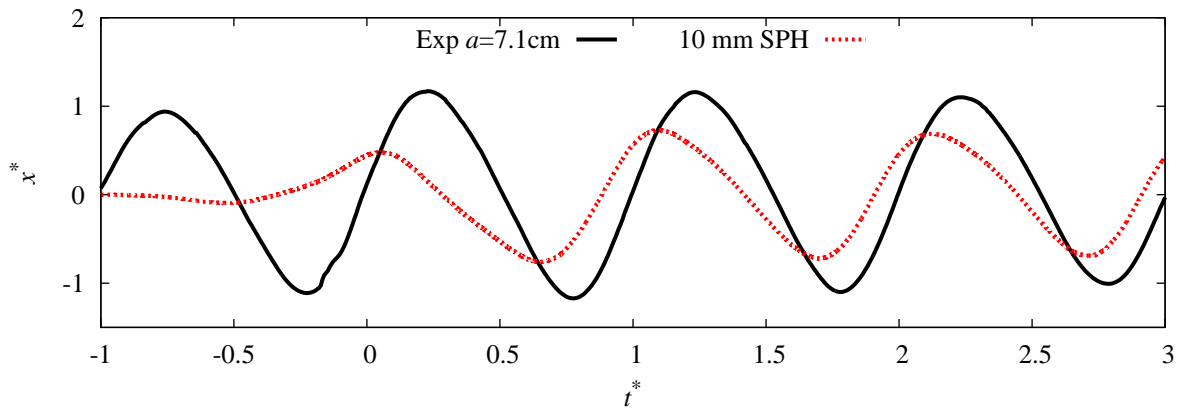


Figure 5.18: Non-dimensionalised surge motion of the buoy in the experiments and simulations with a 3 second period wave train.

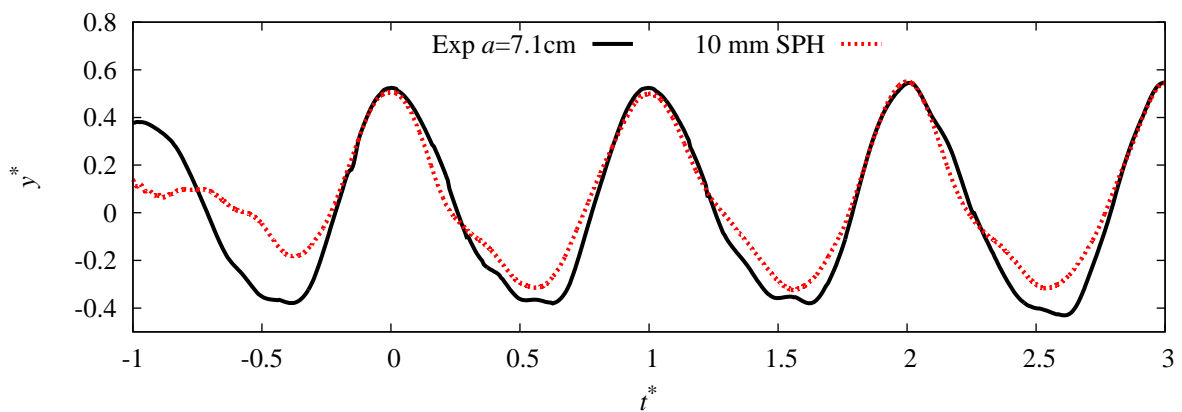


Figure 5.19: Non-dimensionalised heave motion of the buoy in the experiments and simulations with a 3 second period wave train.

the initial transience of the buoy. At a particle spacing of 5 mm, or  $1/40^{\text{th}}$  of the buoy diameter, the transient motion is reasonably predicted (within 10% error); however, if a coarser particle spacing of 10 mm, or  $1/20^{\text{th}}$  of the buoy diameter must be used then errors of up to 35% can be expected in the transient motion of the buoy.

#### **5.2.4 Cause of the heavy damping**

Throughout the wave train cases, the transient motion of the buoy in the horizontal direction has been under-predicted by SPH. The surge oscillation case revealed that the surge motion was heavily damped, however, the heave motion was not subjected to such severe damping (although it was still present). As discussed earlier, energy was significantly dissipated in the vicinity of an oscillating object.

A key difference between these cases was the forces that were driving the motion, and restoring it to the equilibrium position. In the heave motion, the buoyancy was the primary force on the buoy (21 N at equilibrium), followed by the buoy's weight (17 N), and finally the tension in the cable (4 N). However, in the surge motion, the only force restoring it to equilibrium was the tension force in the cable, which had a maximum horizontal component of approximately 1 N. The energy dissipation discussed earlier effectively applied a drag force on the object. When the buoy was oscillating vertically, the dissipation was competing with an average net restoring force of approximately 17 N, while for the horizontally oscillating buoy it was competing with a maximum restoring force of 1 N. Consequently, the heave motion was less susceptible to the energy dissipation since the restoring forces in that direction were an order of magnitude greater than in the surge direction.

#### **5.2.5 Stokes wave theory**

To improve the accuracy of the motion predicted by SPH, refining the particle resolution was the most effective means of improving results. However, refining the particle spacing resulted in an excessively large number of particles that required infeasibly large computational resources to resolve. If the wave maker region generated waves with velocity fields that have higher order of accuracy, then the coarser resolution simulations could provide more accurate results. The waves simulated earlier were generated using Airy linear wave theory, but other theories (such as Stokes 2<sup>nd</sup> or 3<sup>rd</sup> order, cnoidal theory, or stream function theory) could potentially be more appropriate for generating the desired waves.

Figure 5.20 shows a plot of regions of wave theory validity for nondimensionalised depths and wave heights, based on data reported by Le Méhauté (1976). Crosses have been added to the plot to indicate the positions of the six wave train experiments discussed earlier, and are

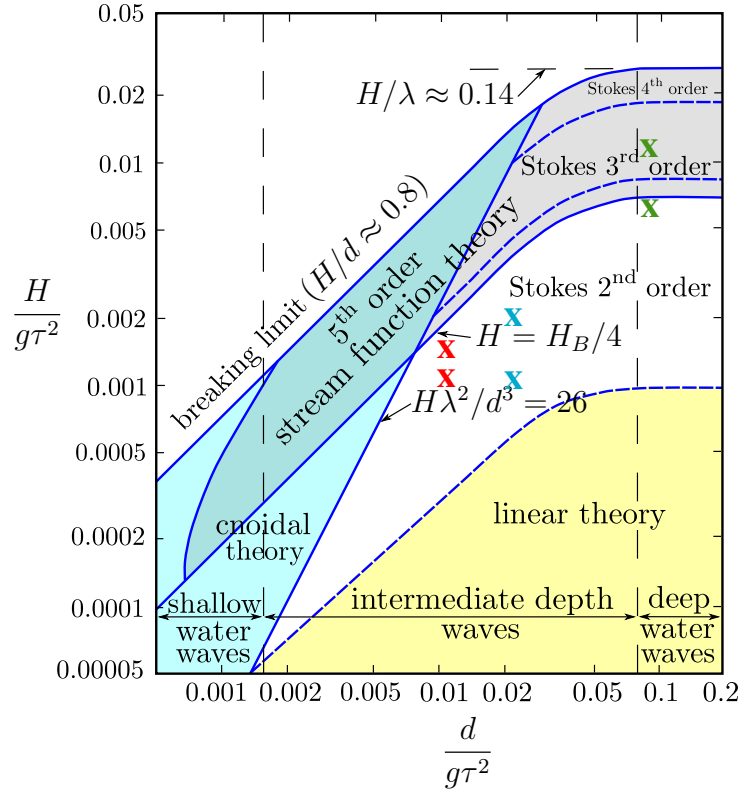


Figure 5.20: Regions where different theories of periodic waves apply. The crosses indicate the waves used in the experiments (green for 1 s period, blue 2 s, and red 3 s). (The figure is adapted under the Creative Commons Attribution-Share Alike 3.0 Unported license from Kraainest (2012), which was based on a similar diagram from Le Méhauté (1976))

coloured based on the period used. The 1 s period waves are indicated by green crosses, 2 s by blue crosses, and 3 s by red crosses. All of the waves fall outside the region where linear wave theory was theoretically valid. This indicated that the waves produced for the simulations may not be sufficiently representative. The waves fell within the region where Stokes 2<sup>nd</sup> order wave theory was most appropriate, except for the 1 second period waves with the largest amplitudes, where 3<sup>rd</sup> order would be the appropriate theory.

In Stokes 2<sup>nd</sup> order wave theory, the velocity field is given by:

$$v_x = \frac{agk \cosh ky}{\omega \cosh kd} \cos \psi + \frac{3a^2k\omega \cosh 2ky}{4 \sinh^4 kd} \cos 2\psi \quad (5.4a)$$

$$v_y = \frac{agk \sinh ky}{\omega \cosh kd} \sin \psi + \frac{3a^2k\omega \sinh 2ky}{4 \sinh^4 kd} \sin 2\psi \quad (5.4b)$$

Comparing these equations with those for the Airy linear wave theory in Equations (4.6), the 2<sup>nd</sup> order Stokes terms can be expressed as:

$$v_{x,2} = \frac{3a^2k\omega \cosh 2ky}{4 \sinh^4 kd} \cos 2\psi \quad \text{and} \quad v_{y,2} = \frac{3a^2k\omega \sinh 2ky}{4 \sinh^4 kd} \sin 2\psi \quad (5.5)$$

The 1<sup>st</sup> order terms  $v_{x,1}$  and  $v_{y,1}$  are the same as the velocity terms given in Equations (4.6).

By setting the cos and sin terms containing  $\psi$  be equal to 1, and  $y$  equal to the depth  $d$ , a comparison could be drawn about the influence of the 2<sup>nd</sup> order terms. Table 5.2 below shows a comparison between the magnitude of the coefficients of the cos and sin terms for the maximum amplitude wave for each period.

For the 3 second period waves, the magnitude of the 2<sup>nd</sup> order Stokes terms was approximately 1% of the magnitude of the linear terms in the vertical direction, and only 0.4% in the horizontal direction. For 2 second period waves, the 2<sup>nd</sup> order terms were smaller, 0.05% and 0.02% of the vertical and horizontal velocity terms respectively. The waves with a 1 second period, which from Figure 5.20 are theoretically meant to have significant 3<sup>rd</sup> order terms, have 2<sup>nd</sup> order terms that were  $2 \times 10^{-8}\%$  smaller than the linear velocity terms. The 3<sup>rd</sup> order terms were smaller in magnitude than the 2<sup>nd</sup> order terms, which were already negligible. Consequently, the Stokes terms could only be expected to have a small influence on the shape of the wave, and for the 1 second period case there was no noticeable effect of the higher order velocity terms.

The wave train simulations were repeated using the 2<sup>nd</sup> order Stokes wave velocity field, but only for the 2 and 3 second wave cases since the 2<sup>nd</sup> order terms of the 1 second period case were negligible. Figures 5.21 and 5.22 show the comparison of the  $x^*$  and  $y^*$  trajectories between the different wave generation schemes with a 2 second period wave. The amplitude of these waves was set to 4 cm to match the largest amplitude in the experiments. The range of oscillation is slightly improved by the Stokes waves, but the initial peak of the surge motion still indicated that the initial transient motion was not well predicted by SPH.

Figures 5.23 and 5.24 similarly show the comparison of the  $x^*$  and  $y^*$  trajectories for the 3 second waves. The amplitude of these waves was specified to be 0.071 m, matching the largest amplitude in the experiments. The differences here were slightly more pronounced than in the 2 second case, with the Stokes wave providing better agreement with the experiments (in particular the surge motions), as well as a smoother curve. This was due to the difference between the first and second order velocity terms being only 2 orders of magnitude (rather than 3 orders in the 2 second period case), and consequently, the forcing region with 2<sup>nd</sup> order terms generated more realistic waves.

The differences in the trajectories shown in Figures 5.21 to 5.24 indicate that the small differences in the velocity terms of the linear and 2<sup>nd</sup> order Stokes theories could cause some

Table 5.2: 1<sup>st</sup> and 2<sup>nd</sup> order velocity terms in the Stokes wave velocity fields for the largest amplitude waves performed in the experiments.

$\tau$ (s)	$a$ (cm)	$\lambda$ (m)	$\frac{v_{x,2}}{v_{x,1}}$ (%)	$\frac{v_{y,2}}{v_{y,1}}$ (%)
1	5.8	1.556	2.14E-08	2.30E-08
2	4.0	4.849	0.02	0.05
3	7.1	7.901	0.39	1.02

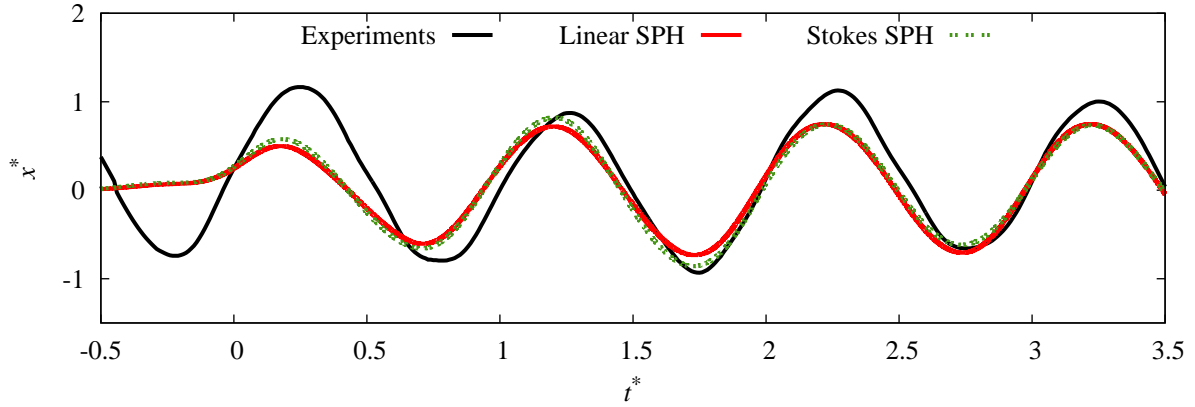


Figure 5.21: Non-dimensionalised surge motion of the buoy in the experiments and simulations with 2 second period wave trains generated by linear or 2<sup>nd</sup> order Stokes waves.

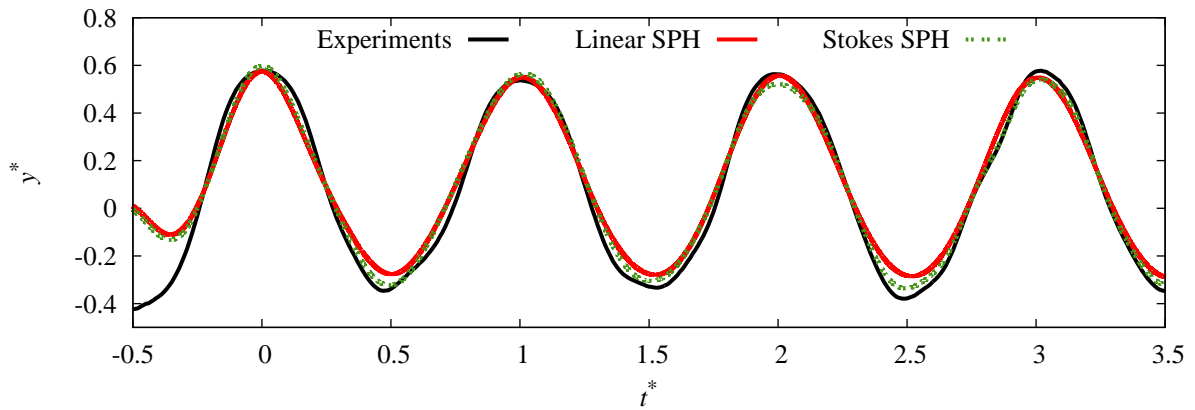


Figure 5.22: Non-dimensionalised heave motion of the buoy in the experiments and simulations with 2 second period wave trains generated by linear or 2<sup>nd</sup> order Stokes waves.

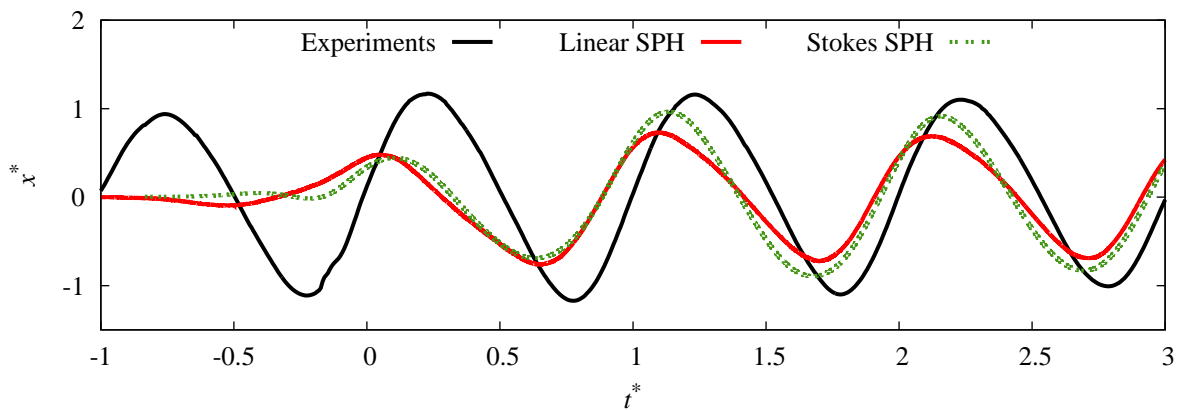


Figure 5.23: Non-dimensionalised surge motion of the buoy in the experiments and simulations with 3 second period wave trains generated by linear or 2<sup>nd</sup> order Stokes waves.

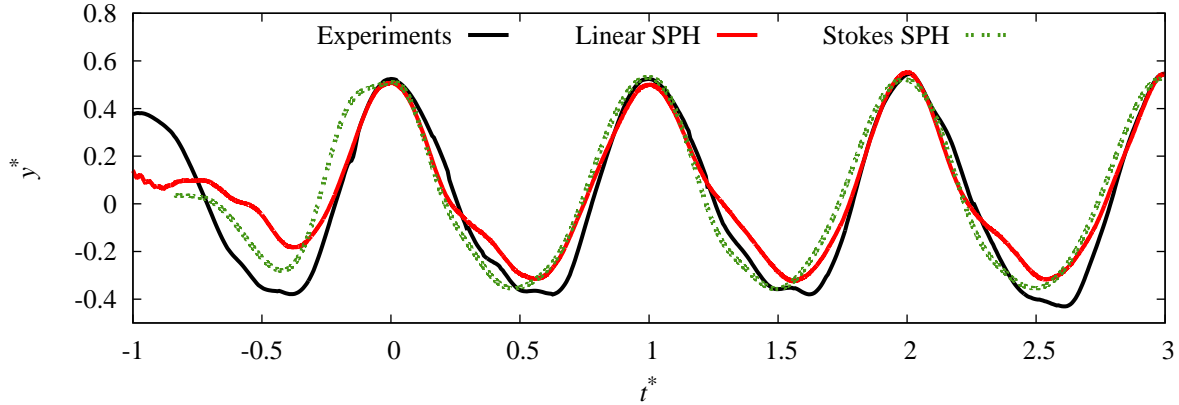


Figure 5.24: Non-dimensionalised heave motion of the buoy in the experiments and simulations with 3 second period wave trains generated by linear or 2<sup>nd</sup> order Stokes waves.

differences in the trajectory of the buoy. The difference in magnitude of the velocity fields in these cases was between 2 orders of magnitude (for the 3 second case) and 4 orders of magnitude (for the 2 second period case). For the later though, the difference in trajectory was small. For a 1 second period wave, it was shown in Table 5.2 that the difference between the 2<sup>nd</sup> order terms and the linear terms was nearly 10 orders of magnitude. Given that the trajectory differences were small when the velocity differences were 4 orders of magnitude, the trajectory differences were indistinguishable in the 1 second period case. Le Méhauté's wave theory plot (Figure 5.20) suggested that 3<sup>rd</sup> order Stokes wave theory was most appropriate for the 1 second period cases; however, the 3<sup>rd</sup> order terms were smaller in magnitude than the 2<sup>nd</sup> order ones, so their influence on the generated wave would also be insignificant.

### 5.3 Summary

The vertical and horizontal oscillation tests show that, with sufficient resolution (particle spacing of 1/80<sup>th</sup> of the buoy's diameter), SPH simulations can model the buoy's initial motion to within 2% error. However, the simulations were observed possess additional damping of the motion that was determined to be due to energy dissipation of the fluid particles around the buoy as it moved. At finer resolutions, the motion of the buoy was found to be more accurate and the energy dissipation was smaller, although still present.

When observing the buoy's response to a wave train, a large amplitude transient motion in the surge trajectory was observed for the 1 second period case, but not in the 2 or 3 second period cases. This transient motion was under-predicted by the SPH simulations that had particle spacings of 10 mm, but a finer 5 mm particle spacing simulation was able to better predict the transient motion. The smaller amplitude of the modulation in SPH simulations indicated that the simulations were insensitive to these initial transient motions, and this was apparent in the

2 and 3 second period cases, where the first surge peak was under-predicted. For the 2 and 3 second period cases, the amplitude of the surge motion was under-predicted by up to 25% and there was a phase error of up to 12%. In both cases, the heave motions were more accurate with a maximum error of 15%.

In an attempt to improve the SPH predictions without refining the particle spacing, the velocity field was modified to follow 2<sup>nd</sup> order Stokes theory. This change was observed to make small improvements to the amplitude of the predicted motion, particularly in the 3 second period case, but no significant improvement of the phase error was noticed. For the 2 second period case, the second order terms was 4 orders of magnitude smaller than the first order terms, and the observed predictions were only marginally closer to the experiments. The 1 second period cases had second order velocity terms 10 orders of magnitude smaller than the first order, so Stokes wave velocity theory makes no noticeable difference. Consequently, the 1 second period simulation cases were omitted from the study.

All of the simulations conducted in this chapter have indicated that the SPH predictions were within 20% error of the buoy's heave motion. As the heave motion was dominated by the weight and buoyancy forces on the buoy, the simulations indicated that SPH could almost accurately model the buoyancy forces. In contrast, the surge motion of the buoy was not as well predicted by SPH, with errors of up to 35% regarding the transient motion of the buoy when the particle spacing was 1/20<sup>th</sup> of the buoy's diameter. The horizontal motion in the oscillation tests, the under-predicted initial peaks in wave train cases, and the under-predicted modulation in the 1 second wave train case, all indicated that SPH had not predicted the transient motion of the buoy particularly well. At a finer resolution of 5 mm, or 1/40<sup>th</sup> of the buoy's diameter, the error in the surge motion of the buoy was reduced to approximately 10% in the wave train case.

The cause of the errors in the surge motion was primarily due to the energy dissipation of fluid particles near the object, which creates additional drag on the buoy. At finer particle spacings, the dissipation was lessened, but still present. It was found that a particle spacing of 1/40<sup>th</sup> of the object's diameter or width gives an error of the order of 10%. If a coarser resolution is required, a particle spacing of 1/20<sup>th</sup> of the diameter gives an error of approximately 35%.

# Chapter 6

## Modelling Peregrine breather rogue waves with SPH

Three studies have previously attempted to produce a rogue wave using SPH: Patel et al. (2009); Campbell and Vignjevic (2012); and Rudman and Cleary (2013, 2016). Although the first two of these studies claimed that an extreme wave was generated, no discussion on how it was modelled was offered. In Rudman<sup>13</sup> and Cleary's studies, a porous medium was dragged through the fluid domain, transferring momentum to the fluid to build up a large wave of water that then collided with a model Tension Leg Platform (TLP). This resulted in a bulk movement of water that impacted the TLP, which is not a realistic representation of a rogue wave.

The three studies also did not provide or refer to the validity of SPH in accurately modelling a rogue wave. This chapter sets out to do just that by experimentally generating a rogue wave and replicating the experiment using SPH, and investigating the accuracy of the simulation.

If SPH can be verified as a feasible methodology for simulating a rogue wave, then it could be confidently used to explore the impact of a rogue wave on a floating tethered object (i.e., a moored ship).

### 6.1 2D rogue wave simulation

The NLS model and Peregrine breather rogue waves were discussed in Section 2.1.3. These have been shown to be capable of experimentally modelling rogue waves. In this section, experimentally generated first and second order Peregrine breather type rogue waves are compared to equivalent waves simulated using SPH. The ability to accurately model rogue waves on a laboratory scale will provide greater confidence in results when simulations are later used to generate larger scale rogue waves.

Chabchoub et al. (2012b) described a carrier wave threshold steepness beyond which a rogue wave will break before it has reached its maximum height. This threshold steepness value,  $\varepsilon_b$ , is given by:

$$\varepsilon_b = a_0 k_0 \quad (6.1)$$

where  $a_0$  is the mean-to-peak amplitude of the carrier wave, and  $k_0$  is its wave number, (see Section 2.1.3 for further detail). For a first order wave, the threshold steepness is 0.12, and for a second order wave, it is 0.06. Consequently, the properties of the waves to be produced were determined by setting a desired  $a_0$  and steepness, and then  $k_0$  could be calculated from Eq. (6.1) and the angular frequency,  $\omega_0$ , from the deep water dispersion relationship:

$$\omega^2 = gk \quad (6.2)$$

However, the NLS assumes that the waves are classified as deep water waves (i.e.,  $k_0 d > \pi$ ). Thus, the values chosen for  $a_0$  and  $\varepsilon_b$  are such that the deep water wave condition is met. The values of these properties are provided in Table 6.1.

In the experiments we desire the rogue wave to be at a maximum height at the start of the testing region ( $x = 0$  in Figure 3.1), which corresponds to a distance of 6.24 m to the mean position of the piston wavemaker. As the transfer function between the input signal and the surface elevation of the water is linear, the input signal is generated by linearly scaling the desired surface elevation at the piston,  $\eta(-6.24, t)$ , described by Eq. (2.7). Since the flow is essentially two-dimensional, the SPH simulations can be performed in 2D without introducing significant error.

However, since the velocity field of the fluid under a Peregrine breather wave is not explicitly known, the methodology of Rudman and Cleary (2016) cannot be used to model the rogue waves. Instead, the piston will need to be modelled with a damping region at the end of the tank to prevent reflections from interfering with the results. The motion of this piston is taken from the time history of the experimental piston, and interpolated using a cubic spline method to ensure a smooth motion since the simulated time step is smaller than the measurement time steps.

Table 6.1: Properties of the rogue waves generated in experiments

Order of the wave ( $j$ )	$a_0$ (m)	steepness	$k_0$ ( $\text{m}^{-1}$ )	$\omega_0$ ( $\text{s}^{-1}$ )	$k_0 d$
1	0.01	0.06	6	7.6720	4.8
2	0.01	0.05	5	7.0036	4.0

### 6.1.1 1<sup>st</sup> order rogue waves

The simulations for the first and second order rogue waves include the piston, the development region and 9 m of the testing region. To reduce the number of particles in the simulation, the depth of the wave tank was set to 0.6 m, which is still sufficient to satisfy the deep water wave conditions required ( $kd > \pi$ ). With these parameters, the simulations required a total of 414,528 particles when using a mean particle spacing of 5 mm, and would require 8 days of wall-time on 12 cores. At this resolution the carrier wave has a wave height of just four particles (peak-to-peak). The final 5 m of the testing region consisted of a region that damped the horizontal motion of the fluid particles, and served to damp out the waves and reduce reflections from the vertical wall at the end of the domain.

Figure 6.1 shows the surface elevation of the experimental and simulated rogue waves at a distance of 6.24 m from the mean position of the piston. The surface elevations were measured as a difference from the still water level in centimetres. The time axis is shifted so that the first large crest (the crest that is more than twice the wave height of the background wave) occurs at time  $t = 0$ . Considering that the background wave was just four particles in height, the simulation matches the experiment reasonably well, although the amplitude of the rogue wave event was smaller than the experimental one. In the physical experiment, the rogue wave had an amplitude of a factor of 3 larger than the carrier wave, yet the simulation only produced an amplitude a factor of 2 larger; a 33% error. Despite this, the specific phase-shift dynamics that characterised the breather evolution appeared to be well represented.

Figure 6.2 shows the surface elevation at the other three measurement points at times close to the rogue wave event. These plots used the same zero-time reference as Figure 6.1 (that is,  $t = 0$  corresponded to the first large peak at 6.24 m from the piston). The plots show a clear progression of the rogue wave; however, at more distant positions from the wave maker, it is clear that the simulated waves arrived at the measurement points earlier than in the experiments, indicating that the waves simulated by SPH are travelling faster than the experiments. Knowing the distance between measurement points, the SPH waves were calculated to be travelling at approximately 0.71 m/s; 11% faster than the experimental waves of 0.64 m/s. Despite this, the phase shift dynamics at each position appeared to still be well predicted. Furthermore, the amplitude of the carrier wave did not decrease over the length of the tank in either the physical experiment or simulation, indicating that there was little or no dissipation of the waves.

The simulation results can be expected to be improved by refining the mean particle spacing, but modifications to the simulation domain are required to use fewer particles so the computational time is not infeasible. The same piston is considered in a smaller domain with the water depth reduced to 35 cm, length to 7.5 m, and the lower boundary set to allow free slip. The final 3 m of this domain is set as the damping region to reduce the wave reflections from the end wall. The piston is located 2 m from the peak rogue wave location and the start-up time is reduced to

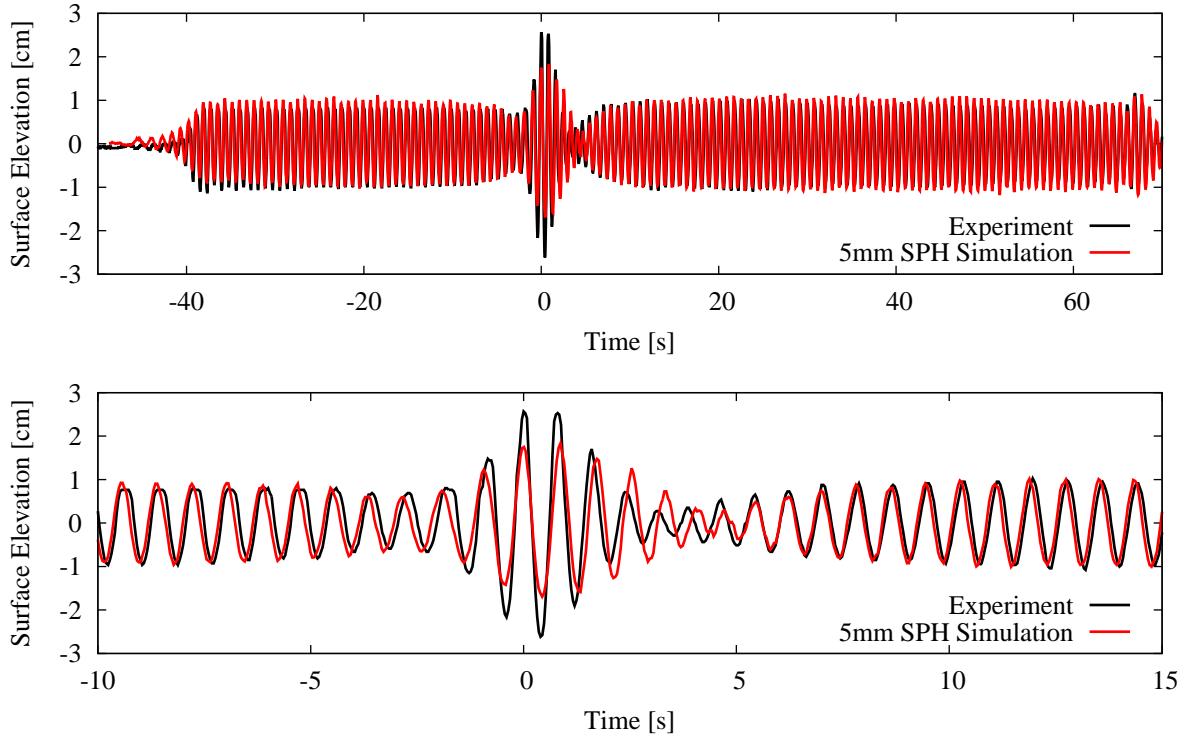


Figure 6.1: Comparison of the experimental (black line) and simulated (red line) surface elevations for the 1st order rogue wave at a distance of 6.24 m from the wave maker. The bottom plot is a magnified view of the top.

20 s before the rogue wave event. Since the location of the piston has changed relative to the rogue wave location, a different piston motion is required. The piston motion used is instead a scalar multiple of  $\eta(-2, t)$ .

However, the reduced depth meant that the waves were no longer classified as deep water waves, so the breather solution was theoretically no longer valid. To ensure that the results were not adversely affected (such as a decreased rogue wave or background wave height), the reduced domain was tested using the same particle spacing as previously. At this particle spacing, only 110,087 particles were required, and the simulation was completed within 2 days of wall-time on 4 cores.

Figure 6.3 compared the surface elevations of the simulations at the peak rogue wave location (2 m from the piston in the reduced domain). The resulting rogue wave in the reduced domain was shown to not be adversely affected despite the reduction in domain. The background waves were equal in height, but the rogue wave itself appeared to possess a larger height in the reduced domain case. This indicated that the reduced domain was acceptable for modelling the rogue waves, despite the breather solutions no longer being theoretically valid.

Using the reduced domain, a rogue wave could be simulated with a refined particle spacing of 2 mm. The 2 mm resolution domain used 705,453 particles, and the rogue wave event could be produced within 2 weeks of wall-time using 12 cores. Figure 6.4 shows the comparison

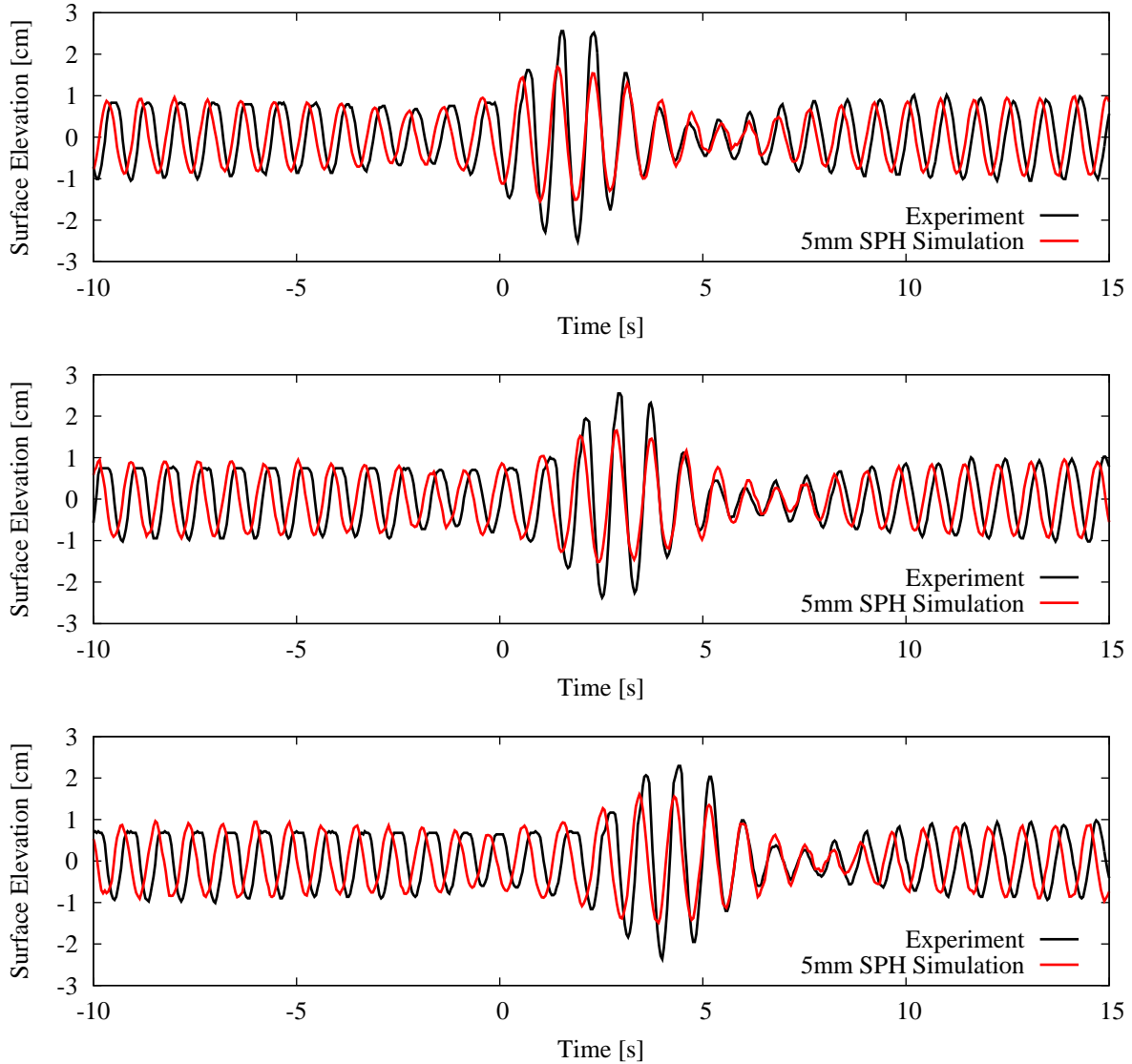


Figure 6.2: 1st Order Rogue Wave at various distances form the wavemaker. Top 7.10 m from the piston, middle 7.94 m, and bottom 8.79 m.

between the experiments and the 2 mm resolution cases. Again, the amplitude of the waves immediately before the rogue wave event was smaller than in the physical experiments; however, the amplitude of the rogue wave event itself was in much better agreement with the experiments than the 5 mm case. As in the 5 mm case, the complex phase characteristics of the rogue wave were again well predicted by SPH. Additionally, the wave speeds of the 2 mm simulation were calculated to be 0.645 m/s, only 1% faster than in the experiments.

The simulations here indicate that a Peregrine breather rogue wave of first order can be accurately modelled using SPH, provided that the amplitude of the carrier waves is equal to or greater than 5 times the mean particle spacing. At coarser resolutions, the height of the simulated rogue waves is not only under-predicted, but the wave speed is predicted to be faster than in reality.

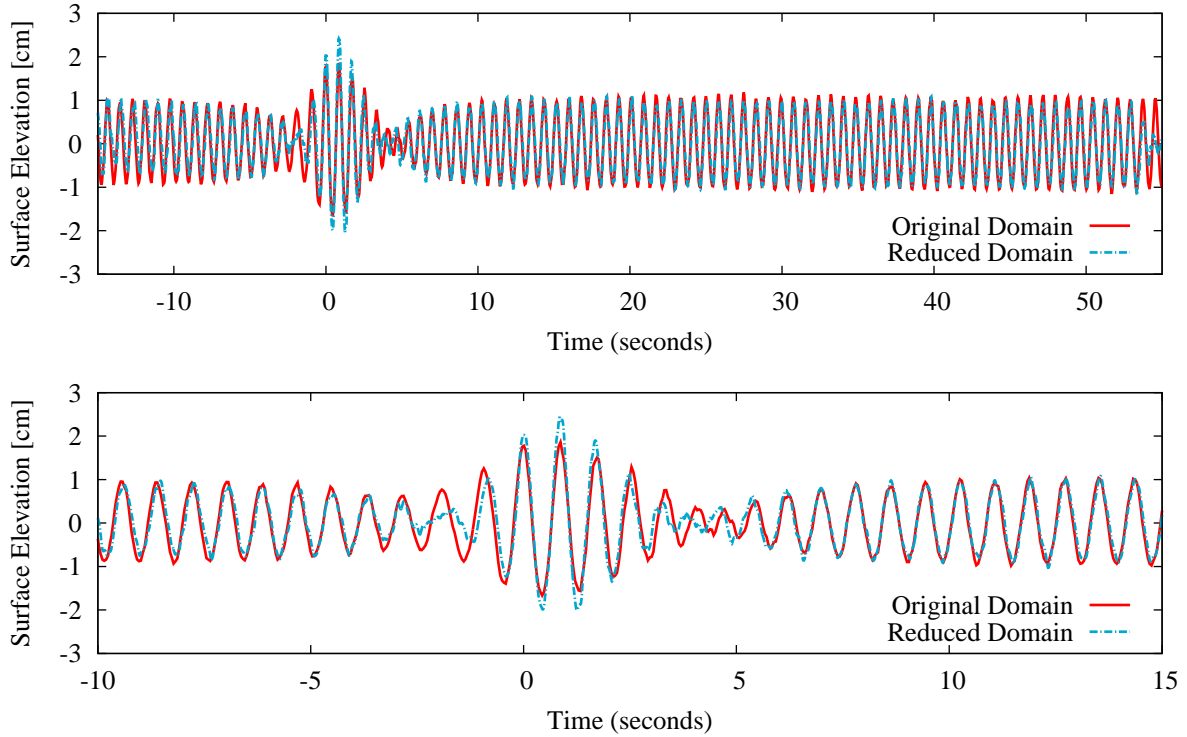


Figure 6.3: Using a refined domain with 5 mm particle separation to produce a 1st order rogue wave.

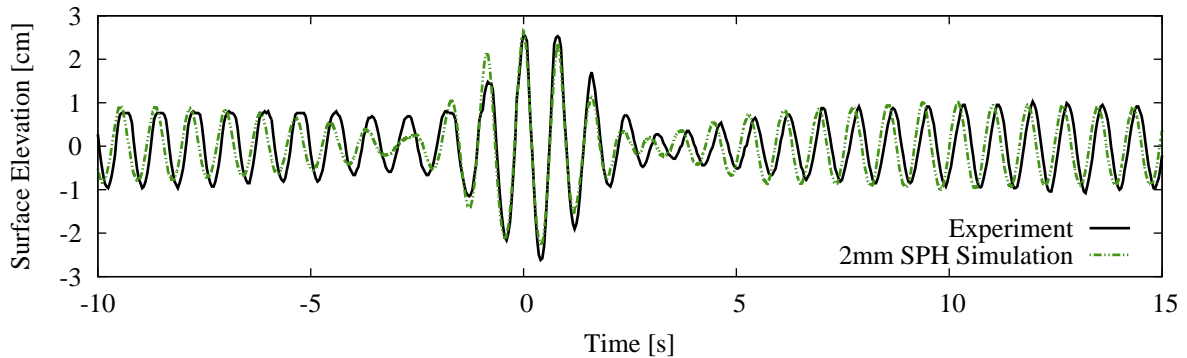


Figure 6.4: Comparison of the surface elevations for the 1st order rogue wave at a distance of 6.24 m from the wave maker for the experiments (black line) and 2 mm resolution simulation in a refined domain (green dashed line).

The velocity field of the water has been represented visually for the 2 mm simulation in Figure 6.5, with  $v_x$  shown in the top and  $v_y$  in the bottom of each subfigure. Previous studies observing these types of waves have only looked at the surface elevation of the wave, and have not considered the velocity field of the water. This velocity field data was simple to obtain from SPH, whereas in physical experiments Particle Image Velocimetry or another imaging technique would be required and thus may not be as simple to obtain.

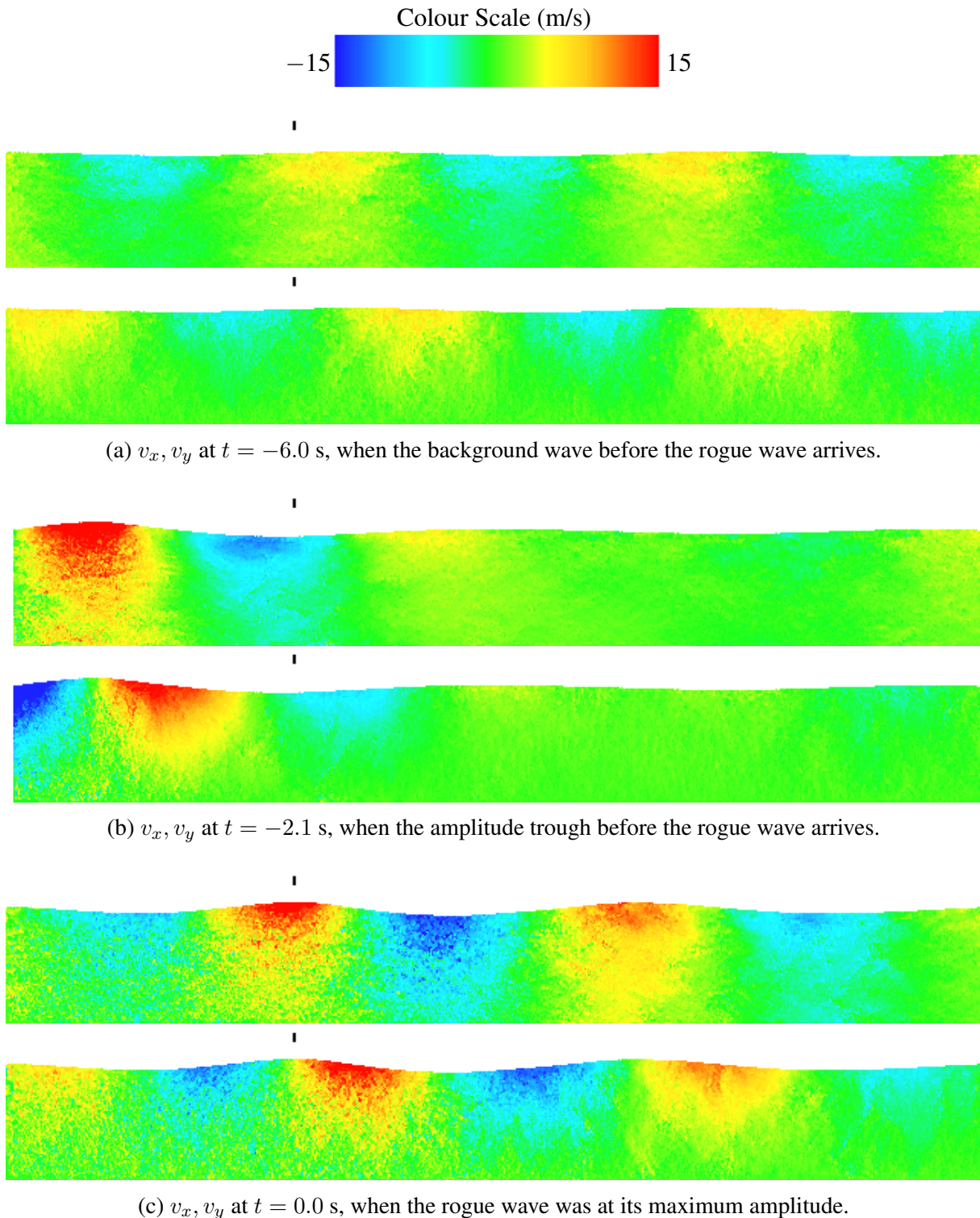


Figure 6.5: Velocity contours of the simulated first order rogue wave with 2 mm particle spacing. The top contour in each subfigure shows  $v_x$  and the bottom figure shows  $v_y$ . Red particles have a velocity of 0.15 m/s or greater, and the blue particles have a velocity of -0.15 m/s. The positive directions are right (for  $v_x$ ) and up (for  $v_y$ ). The black marks above the waves indicate the location of  $x = 0$ , or where the rogue wave was at its maximum.

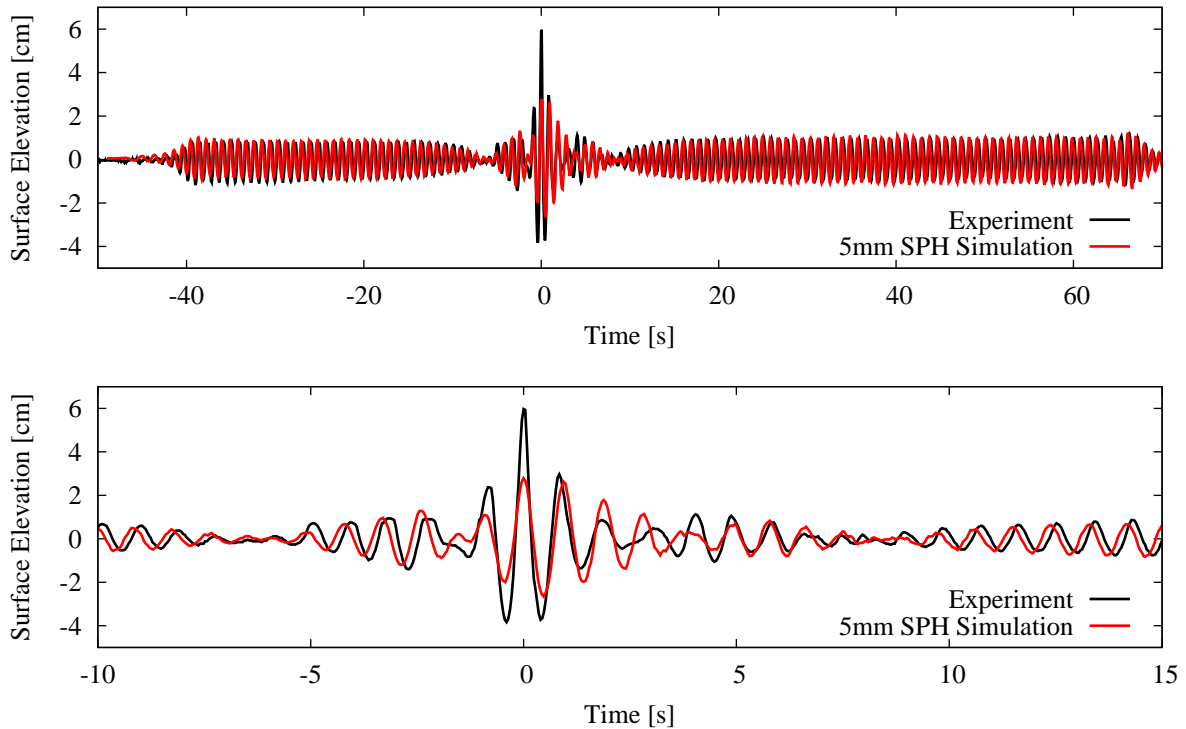


Figure 6.6: Comparison of the experimental (black line) and simulated (red line) surface elevations for the 2nd order rogue wave at a distance of 6.24 m from the wave maker. The bottom plot is a magnified view of the top

### 6.1.2 2<sup>nd</sup> order rogue wave

This section investigates the efficacy of SPH in modelling a second order rogue wave. This wave has an amplitude five times larger than the background wave. The full numerical values and setup of the wave tank from the first test were used; however, the depth was increased to 0.7 m to ensure the waves were in deep water. A particle spacing of 5 mm was again used (total of 474,548 particles), resulting in a background wave of just 4 particles peak-to-peak. This simulation was able to generate the rogue wave within 10 days of wall-time on 12 cores.

Figure 6.6 shows the surface elevation at a distance of 6.24 m from the piston. Similar to the previous test, the simulation predicted the shape of the wave reasonably well and the period between the simulated crests and troughs closely matched those of the physical experiments. However, the amplitude of the rogue wave was again under-predicted. The experiments produced a rogue wave height 5 times larger than the background wave, but the simulation only predicted an amplification factor of approximately 3 (40% error). The phase dynamics of the rogue wave again appeared to be well represented. At positions farther from the wave maker, the background waves were noticed to be more out of phase with the experiments, similar to the 1st order case, and are shown in Figure 6.7. However, the peaks of the rogue wave remained in phase with the experiments, suggesting the group velocity of the rogue wave is accurate for this order solution, although the phase speeds were not. The background waves were calculated

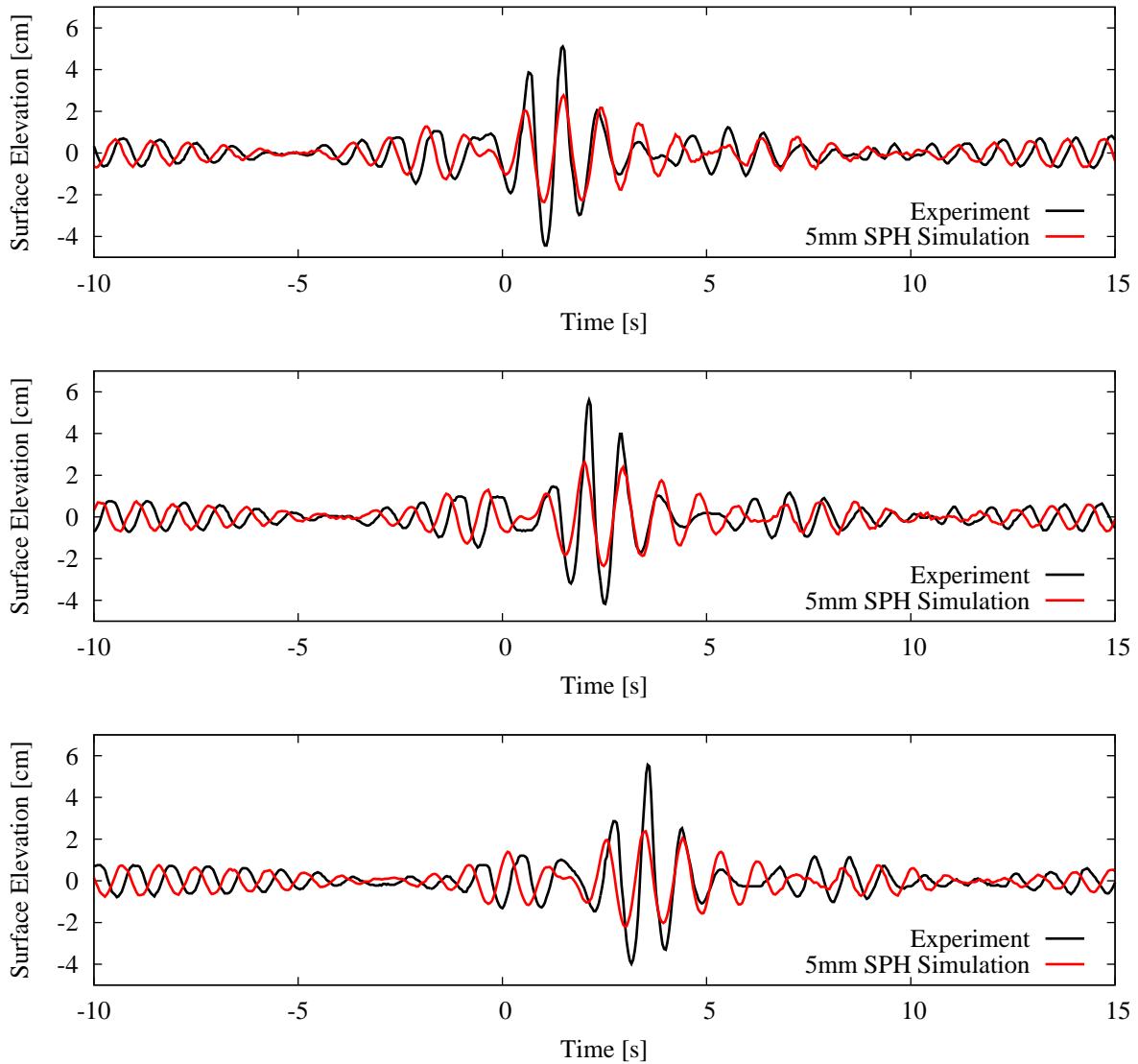


Figure 6.7: 2<sup>nd</sup> order rogue wave at various distances from the wave maker. Top 7.10 m from the piston, middle 7.94 m, and bottom 8.79 m.

to be travelling at approximately 0.77 m/s in the experiments, and 0.82 m/s in the simulations (approximately 6% faster).

In the first order case, the reduced domain with 2 mm particle spacing provided significantly improved predictions of the rogue wave, so the same reduced domain was used to model the second order rogue wave. Figure 6.8 shows the comparison between the experiments and the 2 mm resolution simulations. The agreement with the background wave was similar to the 5 mm case, but the amplitude of the rogue wave event was closer to the experimental values. Additionally, the complex phase dynamics were well modelled and the wave speeds had less than 1% error, as in the first order case. Again, a particle spacing 1/5<sup>th</sup> of the carrier wave amplitude appeared to provide good agreement with the experiments.

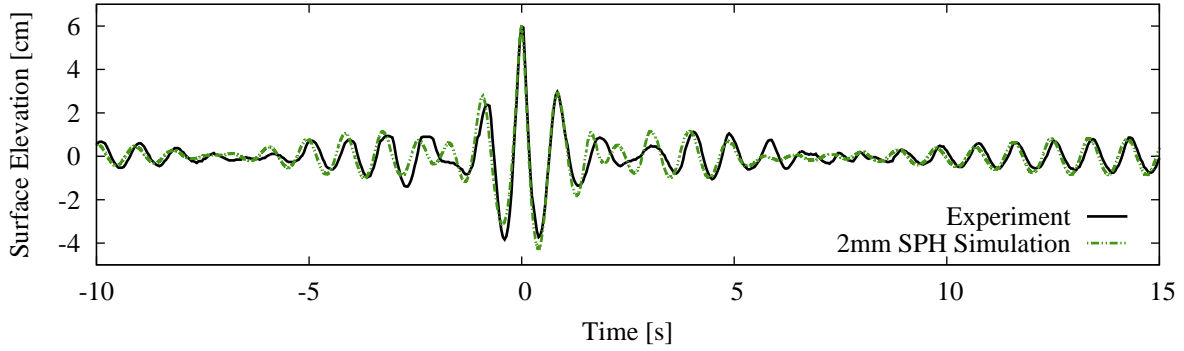


Figure 6.8: Comparison of the surface elevations for the 2<sup>nd</sup> order rogue wave at a distance of 6.24 m from the wave maker for the experiments (black line) and 2 mm resolution simulation in a refined domain (green dashed line).

### 6.1.3 Summary

Two Peregrine breather-type rogue waves, orders 1 and 2, were generated experimentally and replicated using SPH in 2D. For each order wave, an SPH simulation at a coarse resolution (1/2 of the background wave amplitude) and a fine resolution (1/5 of the background wave amplitude) were performed. It was found that at a coarse resolution the rogue wave height had an error of up to 40% and wave speed errors of up to 11%, but SPH was still able to model the complex phase shifts of the waves reasonably well. A reduced domain with depth of 0.35 m and free slip boundaries was tested to allow finer resolution simulations to be performed. The reduced domain had no detrimental influence on the quality of the generated rogue wave, despite the solution no longer being theoretically valid. Using the reduced domain, an improved resolution simulation was able to be performed, finding that the height of the predicted rogue wave matched the experimental values very well, with a wave speed error of only 1%.

From these studies, it can be concluded that SPH is able to accurately model the generation of a Peregrine breather type rogue wave, including the complex phase dynamics that are inherent to these types of rogue waves. To do this, the particle spacing should be 1/5<sup>th</sup> of the carrier wave amplitude,  $a_0$ , or finer. Additionally, the number of particles can be reduced by using a depth satisfying  $kd = 1.75$ . This was equivalent to a depth of 175 particle spacings. Although this depth makes the deep water conditions required by the Peregrine breather waves theoretically no longer valid, it was found that there was no negative effect on the rogue wave produced.

## 6.2 Ocean Scale Rogue Wave Impacts

The ultimate goal of this study is to explore the efficacy of using SPH for modelling the impact of a rogue wave on a floating tethered body. In so doing, the capabilities of SPH can be validated.

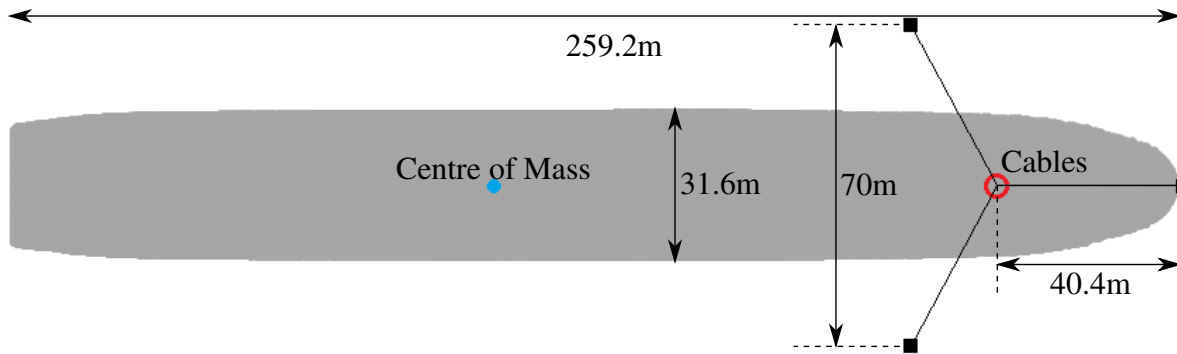


Figure 6.9: Arrangement of the three tethering cables on the ship model. The bow of the ship is located on the right of the image.

This section presents the findings and analysis of using SPH to model a variety of impacts between rogue waves and a full scale moored ship. Since not all rogue wave impacts are identical, a number of different scenarios are modelled. These investigated the effect that the mooring cable stiffness, ship mass, wavelength, and rogue wave height have on the impact.

A theoretical ship, measuring 259.2 m in length and 31.6 m in width, was used. The ship had a moulded depth of 23.5 m, and has a draught of 12.0 m when sitting in still water. It had a mass of 52,196 tonnes, and its centre of mass was located on the mid-plane, 12.6 m from the hull and 152.1 m from the bow. It was tethered by three cables attached to the midline of the hull, 40 m from the bow, and reached to the ocean floor, 175 m below the free surface. The mooring points of the cables on the floor formed an equilateral triangle with side-length of 70 m (see Figure 6.9). The cables have a spring-stiffness of  $1.7 \times 10^6$  N/m and an un-tensioned length of 157.1 m. When the ship is at equilibrium, the cables have a tension of approximately 13.6 MN.

A 3D numerical wave tank was simulated. It was 700 m in length and 72 m wide with periodic lateral boundaries, as shown in Figure 6.10. A piston (not shown in the figure) was located at the front-left end of the tank and a vertical wall was at the far end. Numerical damping was applied in front of the wall to reduce wave reflections. The centre of mass of the ship was located 330 m from the piston, with the bow of the ship pointing toward the piston. Although the ship's width was 44% of the width of the tank, the overall blockage ratio was below 5%. The ship does not adhere to the periodic boundaries, so ideally a wider domain should be used to ensure that the ship does not cross the boundaries. However, due to the already significant computational expense of these simulations, a wider tank was not a viable option. Also, due to the symmetry of the ship, any net side force or torque about the  $y$ -axis would be minimal and should not impart sway or yaw motion.

The piston motion was chosen to generate a 9 m background sea state, with the Peregrine breather rogue wave appearing at 200 m from the piston (shown in Figure 6.10 by the transparent yellow plane) 300 seconds after the start of the simulation to provide sufficient build up time. The wave elevation was 150 m from the piston, or 27.9 m in front of the bow of the ship - this is

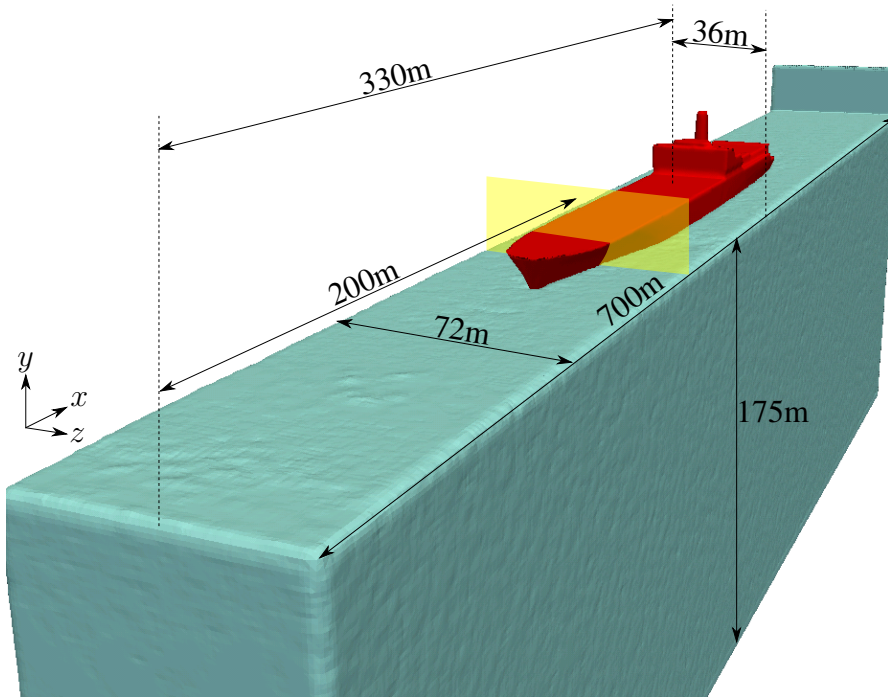


Figure 6.10: The domain used for the large scale rogue wave impacts. The transparent yellow plane is located where the rogue wave will be at its maximum amplitude. Note that the coordinate axes is not centred at the origin.

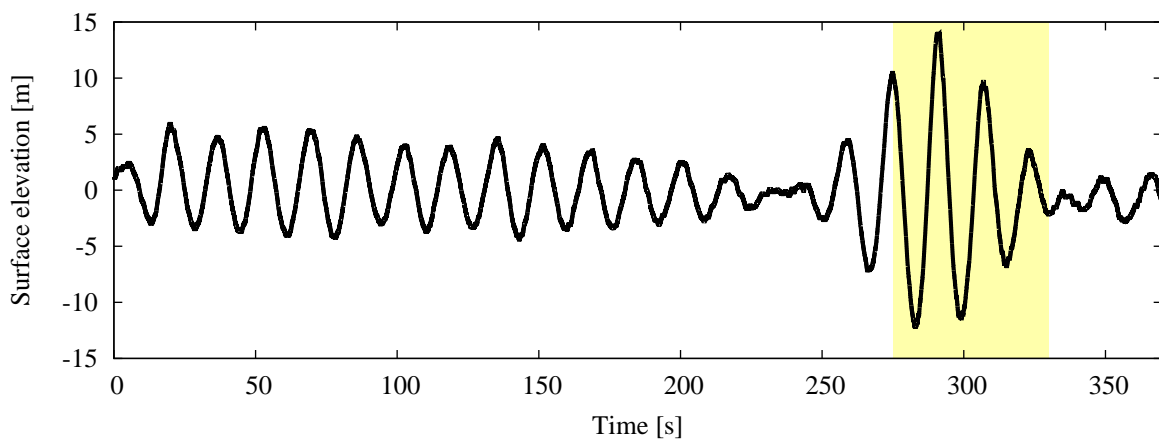


Figure 6.11: Elevation of the wave heights relative to the still water height

shown in Figure 6.11. The background waves were approximately 9 m in height and the rogue wave height was 26.1 m. Since the surface elevation in this figure was measured ahead of the ship, it has not yet reached the peak rogue wave location, so the rogue wave would be greater when it interacts with the ship. The yellow highlighted times represents the region of impact time (or, more simply, when the ship interacts with the largest waves in the simulation).

The ship model had a boundary particle spacing of 1 m, and this value was also used as the mean particle spacing for these simulations. At this particle spacing, the background wave had an amplitude of 4.5 particle spacings, which was close to the ratio of 1:5 that was recommended

in Section 6.1 for accurately modelling rogue waves. Additionally, this particle spacing has a  $\delta x:d$  ratio of 1:175 that ensured the deep water wave conditions were approximated correctly. The simulation used 8.3 million particles and required over 8 weeks of wall-time to complete the simulation. The ratio of the particle spacing to the width of the object was 1:31.6, which was less than the 1:40 ratio that was recommended in Chapter 5. Therefore, errors of the order of 15 to 20% could be expected.

It must be noted that no special consideration was given to any turbulence modelling in these simulations. Studies have been performed showing that turbulence modelling can be done with SPH (Shao and Gotoh, 2005; Violeau and Issa, 2007), although no validated turbulence model was available for this study. Despite this, Khayyer et al. (2008) suggested that “the effect of turbulence in macroscopic behaviour of hydrodynamic flows does not seem to be significant (Gotoh et al., 2005)” (p. 22), so the overall results obtained here were unlikely to be significantly altered by the introduction of a turbulence model.

### **6.2.1 1<sup>st</sup> order rogue wave impact**

The first rogue wave impact to be studied will be used as the base case, against which, all of the following cases will be compared. The ship will face into the wave, so the rogue wave will directly impact the ship’s bow. The key aspects of the impact that will be calculated are:

- the trajectory of the ship’s centre of mass (CoM);
- the pressures at points on the surface of the ship along the bow; and,
- the total tension in each cable.

#### **6.2.1.1 Ship motion**

A visualisation of the ship’s motion is shown in Figure 6.12, showing the ship’s interaction with the waves at various times. In (a), the ship was interacting with the background wave in a regular motion, while in (b), the ship was ascending the first large wave in the impact time. The rogue wave was at its maximum in (c), where the bow of the ship can be seen to nearly be completely out of the water, and in (d) the bow is almost completely submerged.

The trajectories of the ship’s CoM are shown in Figure 6.13. The range of the heave motion was only a few metres in the background waves, but it peaked at 13 m during the rogue wave impact time. The surge motion, however, had an initial transient motion similar to what was observed with the buoy in sinusoidal waves in Section 5.2. Two transient motions were observed in the surge motion of the ship; when the background waves first interacted with the ship, and when the rogue wave impacted the ship. The first of these transient motions had a small amplitude and

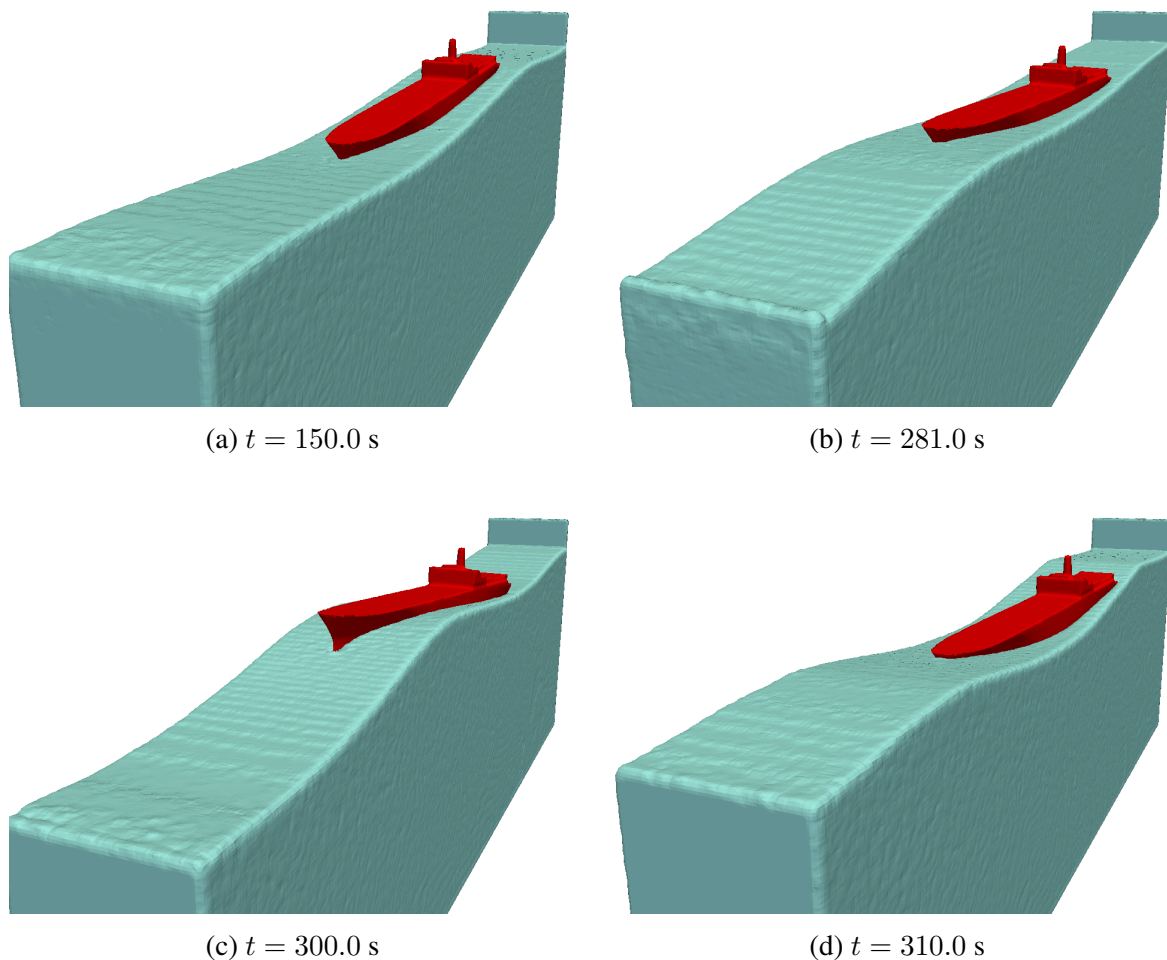


Figure 6.12: The ship in a rogue wave. (a) The ship at its lowest point in the background wave. (b) The ship is climbing the wave that precedes the rogue wave. (c) The rogue wave is at its peak amplitude. (d) The ship plunging into the wave following the rogue wave, where the risk of green water on deck is greatest.

had almost completely dissipated when the rogue wave impacted the ship. This was due to the long time frame for the motion to dissipate, and also due to the waves having small amplitudes shortly before the rogue wave impact. The amplitude of the transient motion from the rogue wave was larger than that in the previous transient motion; however, there was insufficient data to determine the long term behaviour of the motion after the rogue wave impact.

The pitch of the ship was also analysed in Figure 6.14. During the impact time, the pitch of the ship achieved a maximum of  $6^\circ$ . As the ship was 260 m long, even small pitch angles could cause the bow and stern to move significantly. The effect this had on the heights of the top of the bow and stern is shown in Figure 6.15. In the background waves, the bow and stern of the ship have a range of motion of approximately 10 m; however, when the rogue wave impacted the ship the largest height change was 24.9 m for the bow and 28.8 m for the stern, both of which occurred over a time period of approximately 7.5 seconds.

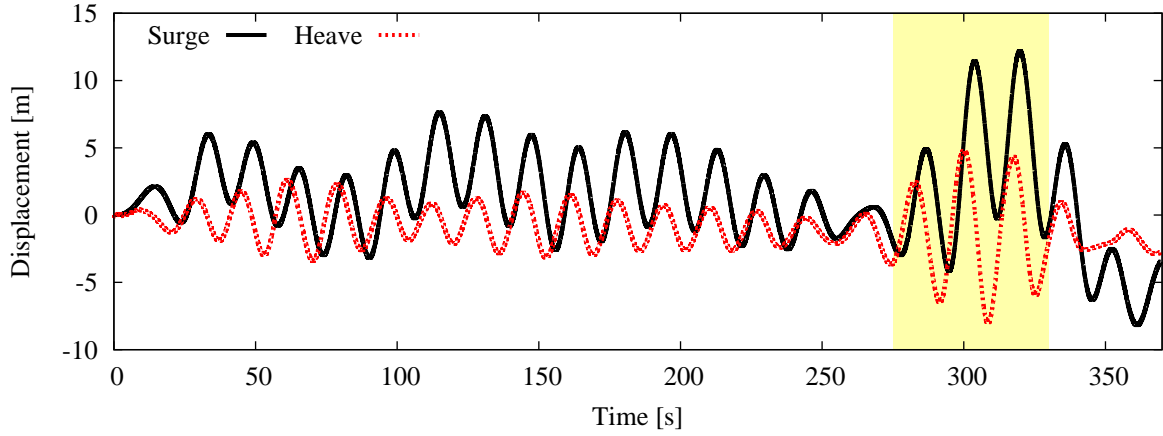


Figure 6.13: Displacement of the ship in the surge ( $x$ ) and heave ( $y$ ) directions.

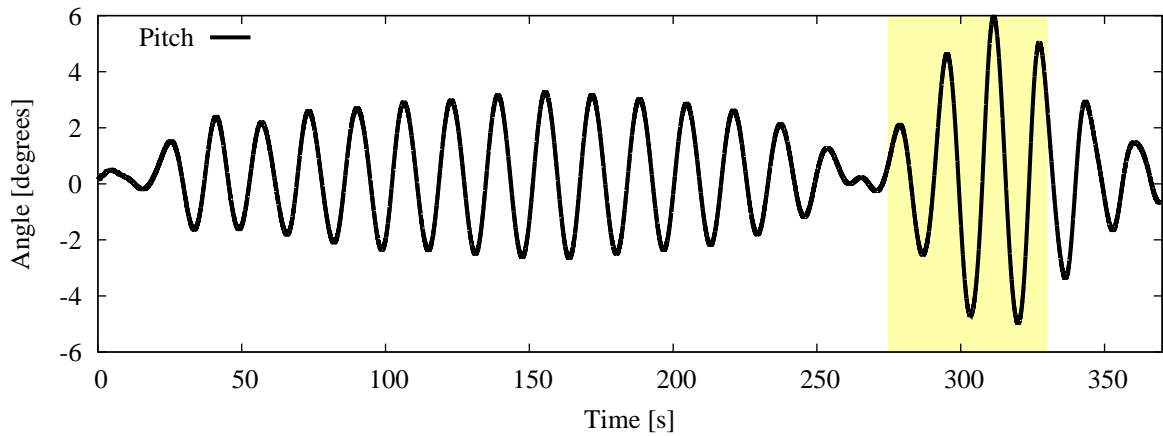


Figure 6.14: Trajectory of the ship's roll and pitch motions.

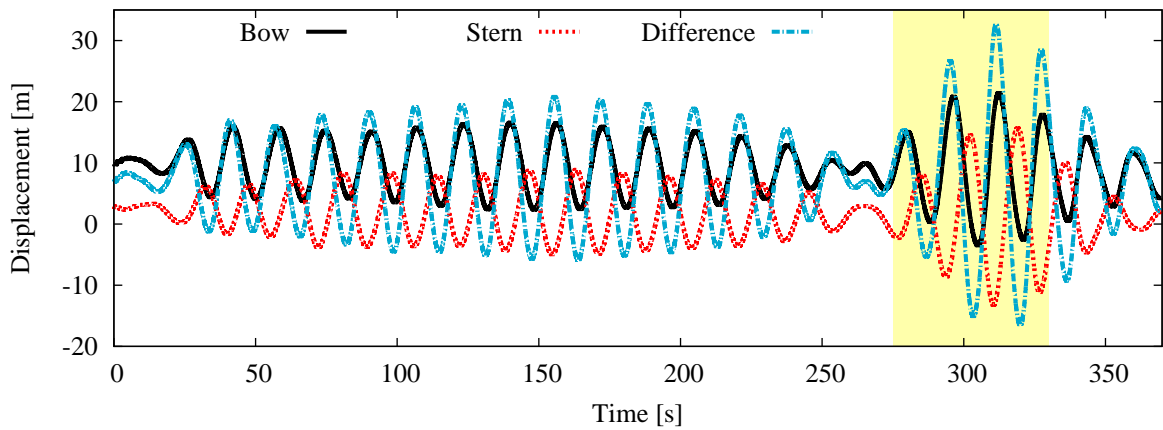


Figure 6.15: Trajectory of the ship's bow and stern vertical motions, relative to the still water height.

### 6.2.1.2 Pressure readings

The impact forces on any vessel are of significant importance for its safe design. Previous studies (Cummins et al., 2012; Rafiee et al., 2012) have shown that the SPH method was capable of

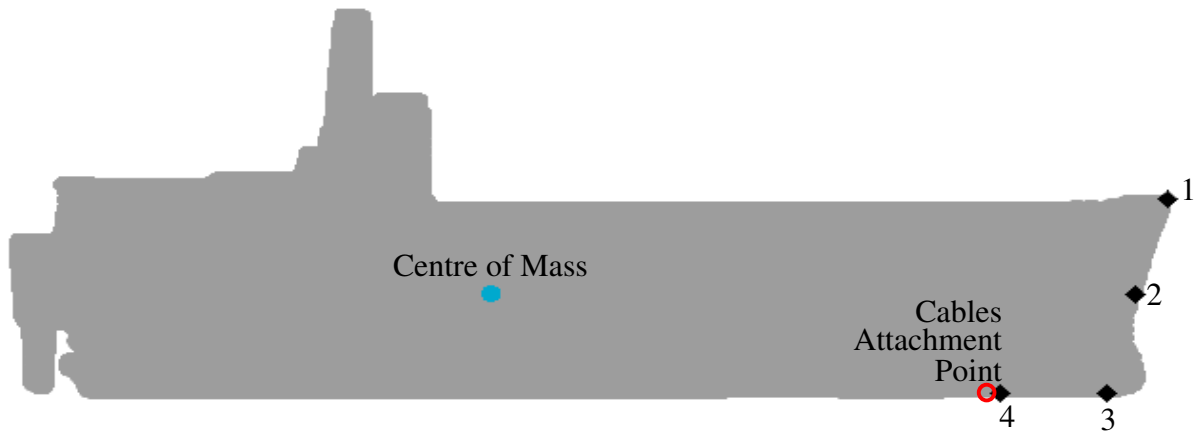


Figure 6.16: Locations of the pressure sensors on the ship.

modelling these impact forces if the high frequency fluctuations were removed. Consequently, the pressure on the ship could be calculated using the equation of state, Eq. (2.17), with confidence that realistic results would be obtained if the high frequency fluctuations are addressed.

A number of locations on the midplane near the bow of the ship were chosen to measure the pressure. These are shown in Figure 6.16. Other locations farther along the hull of the ship were measured, but they did not reveal any additional information than what was measured by the four points shown. Table 6.2 shows the exact locations of the sensors, relative to the centre of mass of the ship (with positive  $x$  towards the bow of the ship).

Pressure readings are shown in Figure 6.17. To remove the high frequency fluctuations in pressure, the data has been smoothed using the mean of the surrounding 0.3 seconds of data. Müller et al. (2005) claimed that vessels were typically designed for a maximum pressure of 150 kPa, and pressures exceeding 300 kPa may cause them to be compromised. The pressure plots show that the peak pressure was 274.4 kPa, and this is within the limit set by Müller et al.

The pressures at point 1 are constantly 0, indicating that this point was never submerged. This was supported in Figure 6.12d, showing that the bow was not submerged when the ship entered the trough after the rogue wave passed. Thus, the ship in this case avoided any green water on the deck. If the amplitude of the waves were larger, or the ship was heavier, then the ship may dip into the following wave and be subjected to green water effects. It can be observed that the pressures at points 2 and 4 have larger peaks during the rogue wave impact than they

Table 6.2: Locations of the pressure sensors

Sensor number	$x$ (m)	$y$ (m)
1	152.1	11.9
2	144.5	0.0
3	138.3	-12.4
4	114.2	-12.3

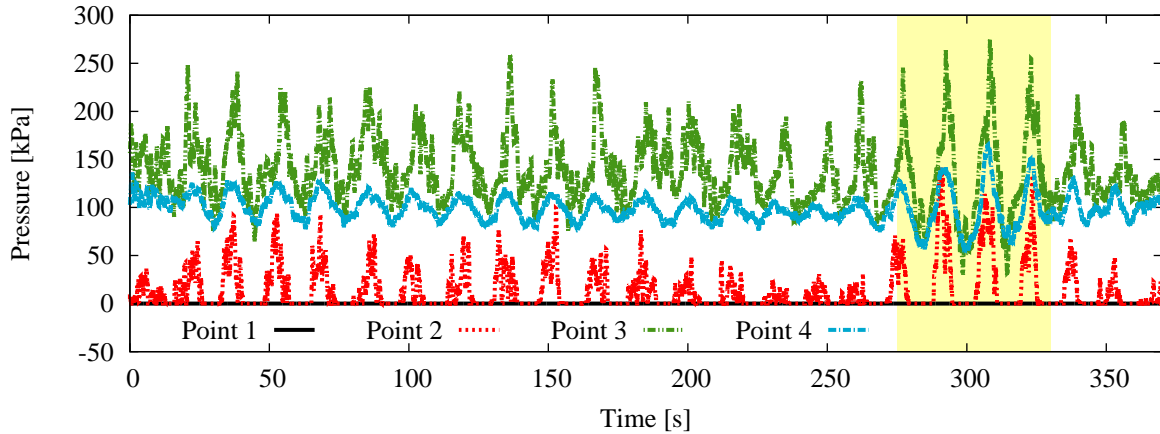


Figure 6.17: Pressures at each of the sensor locations

do during the background wave. However, the pressure at point 3 had larger peaks which were of similar size throughout the entire simulation, and they were only marginally larger during the rogue wave impact. This may have been due to the main source of the pressure at this point coming from the constant interaction of the ship's bow with the oncoming waves (this was not as significant or present for points 2 and 4). The larger rogue wave appeared to have only a small influence on the magnitude of these pressures. During the impact, the pressures at point 3 were also observed to be at their lowest, particularly just after the peak rogue wave and following wave had passed the bow. This low pressure was due to the bow of the ship rising to nearly be completely out of the water (see Figure 6.12c), and thus the hydrostatic pressure on it was low. It could be expected that slamming loads at point 3 would be larger after interacting with the larger rogue wave, but these were not shown in the simulations. This was likely to be due to the lack of resolution needed to model the mechanics of such violent impacts that could produce the large impulse pressures (such as cavitation and air entrainment). However, the already costly nature of the simulations prohibited further refinement of the simulations which would be required to study slamming loads.

### 6.2.1.3 Cable Tensions

The cable tensions are shown in Figure 6.18. Due to the symmetry of forcing, there was negligible motion of the attachment point in the  $z$  direction, so the tensions in the two side cables were nearly identical at all times, and therefore only one is shown in the figure. During the impact, it was observed that the side cables had 0 tension, or the cables had become slack. The maximum tension in the cables while in the carrier wave was 23.3 MN, but when the rogue wave impacted the maximum tension reached 30.0 MN.

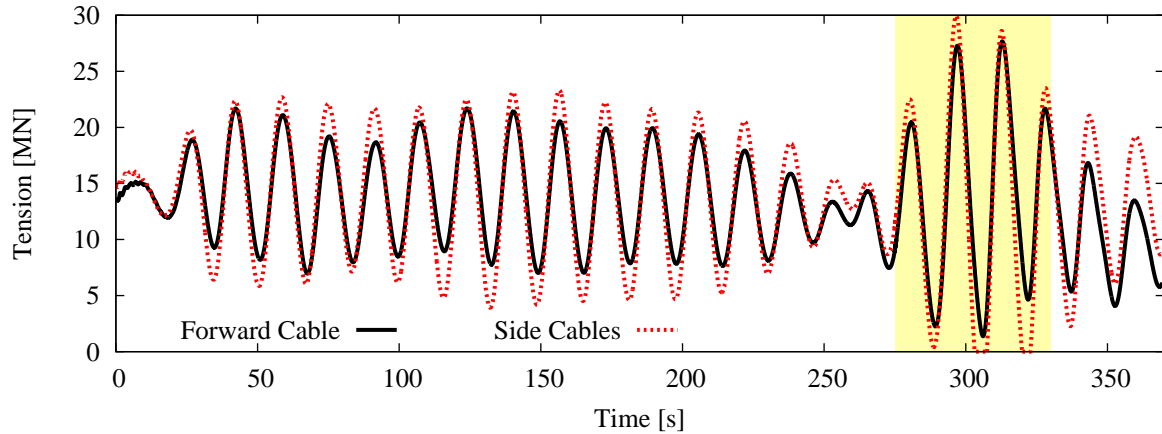


Figure 6.18: Tensions in the ship's cables during a rogue wave impact.

#### 6.2.1.4 Summary

SPH was used to model the impact of a 27 m high rogue wave on a ship - a scenario for which experimental data is unavailable. In this study, there was found to be no green water on the deck of the ship as the heave and pitch of the ship allowed the deck to remain above water. However, the bow and stern of the ship both had large vertical displacements during the rogue wave. The stern moved nearly 29 m over 7.5 seconds. During the rogue wave impact, a maximum pressure of approximately 275 kPa was predicted on the hull of the ship, near the bow. Allowing for a safety factor of 1.1 in the model, this pressure was greater than the 300 kPa limit that was suggested by Müller et al.

While the pressure was measured only at four points on the ship, it is possible for the pressure to be measured at many locations. Doing so would allow a pressure map on the ship to be generated that could then be used in a Finite Element Analysis to determine the effect those pressures would have on the hull. However, the coarse resolution used in this study meant that the phenomena that cause high impulse pressures during slamming could not be well modelled. Therefore, the peak pressures may be much higher than what was observed in the simulations. Unfortunately, the already high costs of performing the simulations prevent finer resolutions being used to more accurately model slamming loads at the present time.

The scenario modelled here is just one of many possible scenarios that are likely to occur in reality. How the ship is tethered can influence the results, as can the mass (or load) of the ship. Additionally, the rogue wave that was generated is just one of many possible waves. Waves with larger amplitudes or with longer or shorter wavelengths are possible, and the effects of which are unknown. It is important to understand how the ship responds to many different conditions. Some of these difference scenarios were investigated, and this work is reported in the following sections.

## 6.2.2 Effect of using a higher cable stiffness

In the previous simulation, the ship was observed to have a range of motion large enough for it to avoid any green water effects. For some vessels, such as drilling vessels, this range of motion may be too large and thus stiffer cables are desired to limit the range of motion. In these cases it is important to understand the effects that the different cable stiffnesses have on the impact of a rogue wave, and particularly if there is any green water on deck.

To determine these effects, the ship in a 1<sup>st</sup> order rogue wave is modelled with the cable stiffnesses increased to  $3 \times 10^6$  N/m (a 76% increase), and the untensioned length increased so that the tension at equilibrium is unchanged. In order to reduce computational time, a snapshot taken 10 seconds before the rogue wave impact (i.e., at  $t = 265$  s) is saved and commenced from then with the modifications to the cables made.

The comparison between the overall tension in the cables are shown in Figure 6.19. The stiffer cables were observed to have larger peak tensions, with the maximum tension being 36 MN in the side cables. Despite the increase in tension, the motion of the ship in response to the rogue wave impact was nearly identical to the base case. The only difference was a marginally smaller period of oscillation for the transient motion in the surge direction due to an increase in natural frequency. As a result of the motion remaining the same, there was no difference in the pressures at the four measured points.

Finding that the spring stiffness had an insignificant effect on the overall motion of the ship was not surprising when the overall buoyancy forces were considered. Figure 6.20 shows the peak buoyancy force was approximately 600 MN, a factor of 17 times larger than the maximum tension in the cable, indicating that the influence of the cable stiffness was small unless significantly stiffer cables were used.

## 6.2.3 Effect of additional load

The original simulation was performed using the ship without any cargo, which, if the ship were an FPSO, would be equivalent to when the vessel had been unloaded or had yet to commence production. Heavier ships are more at risk of green water effects as they have higher draughts. Consequently, two additional simulations were performed that model a ship that was carrying cargo equal to 30% and 100% of the ship's gross tonnage. As with the higher stiffness simulation, the simulations were restarted from a snapshot at  $t = 265$  s.

The ship with 30% additional mass was observed to typically sit approximately 2 m lower in the water in Figure 6.21a, while the ship with 100% additional mass sat 7 m lower. The relationship between additional mass and the change in heave position was approximately linear, with the ship sitting 0.137 m lower in the water for each 1,000 tonnes of cargo. This linear relationship

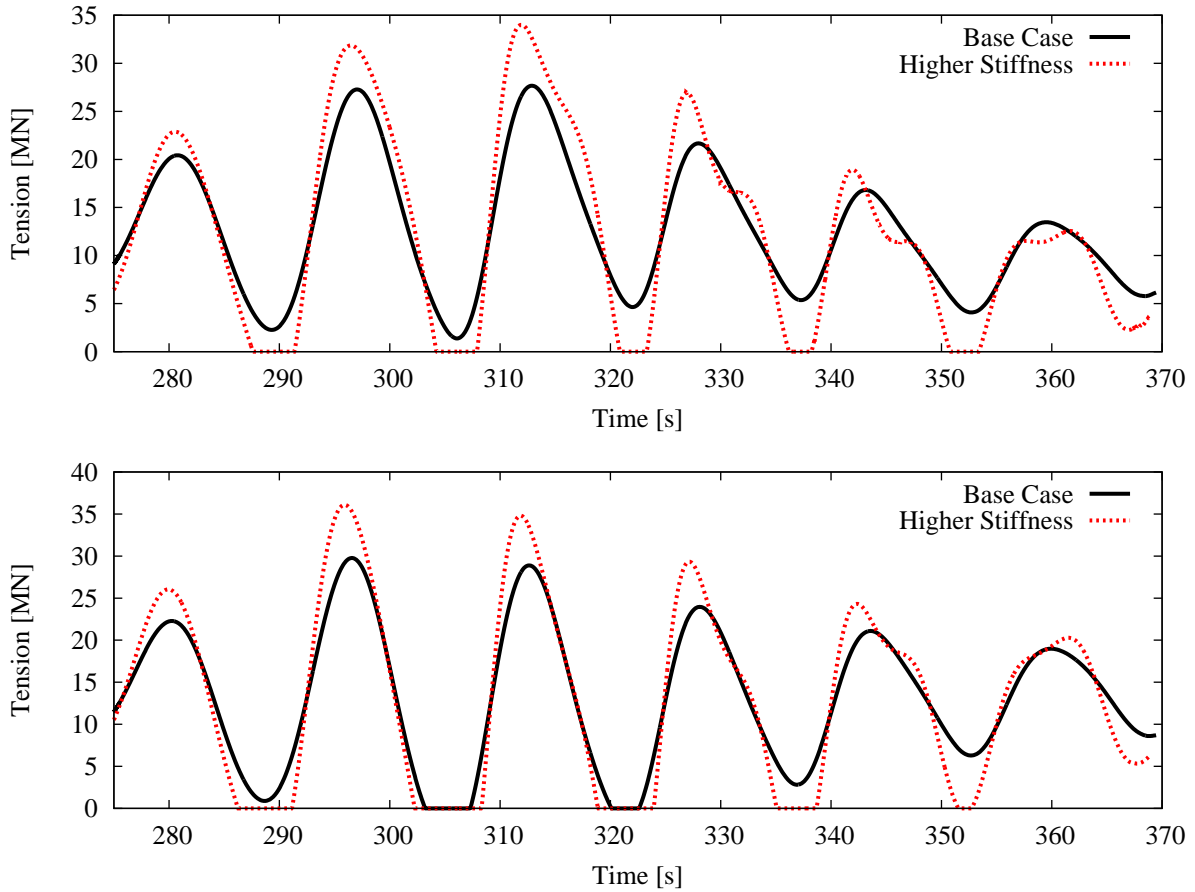


Figure 6.19: Tensions in the forward pointing cable (top figure) and side cables (bottom figure) for the case with higher stiffness cables attached to the ship.

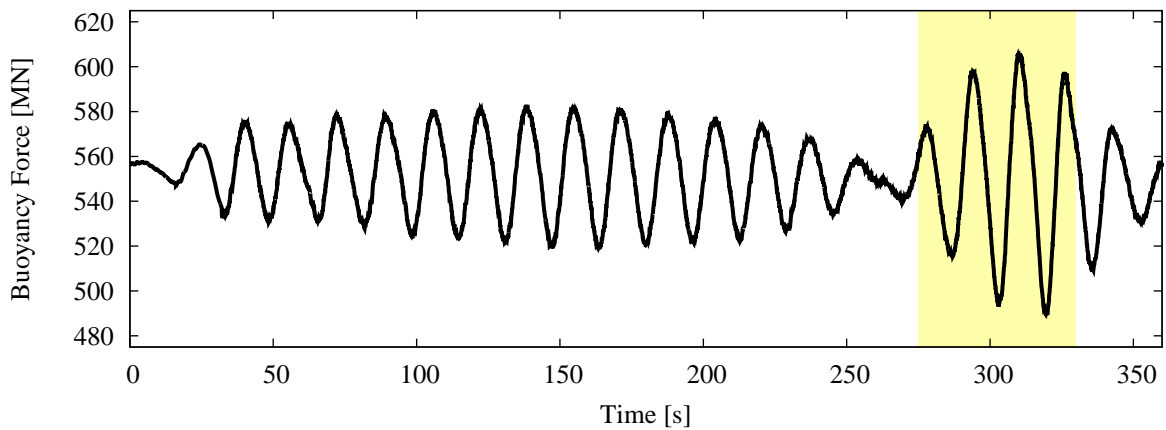
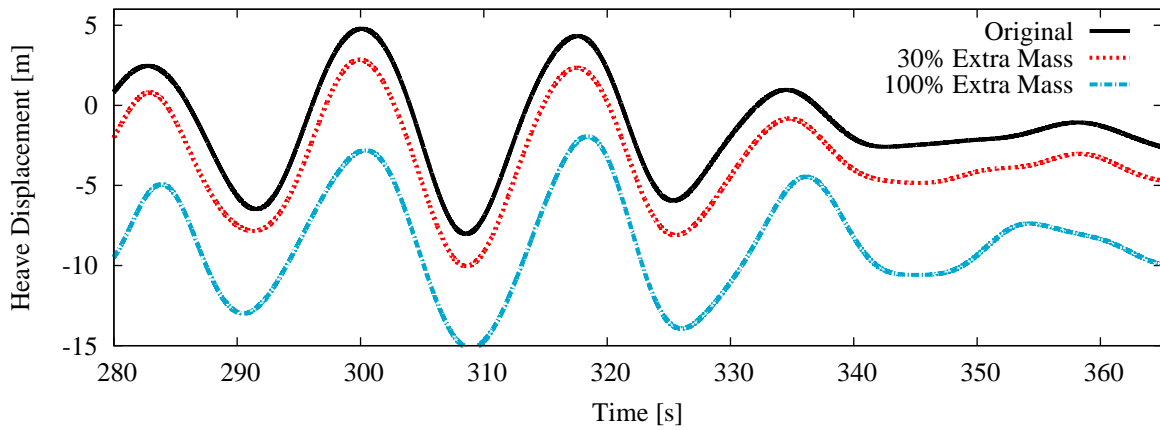


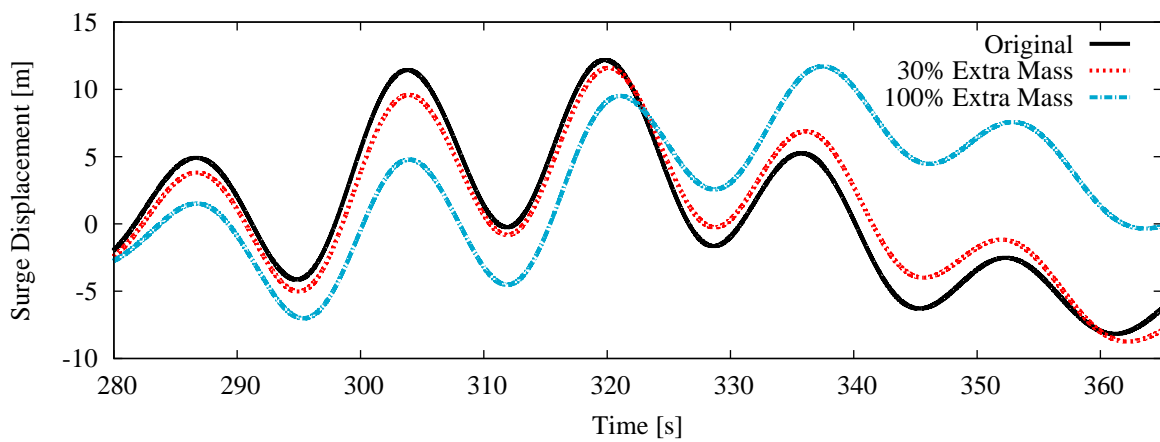
Figure 6.20: Buoyancy forces on the ship during a rogue wave impact.

was expected as the cross-sectional area of the ship remained approximately constant from the original waterline up to the ship deck.

Given the increase of inertia, the heavier ships' surge motions has slightly smaller amplitudes, as shown in Figure 6.21b. For the ship with 100% extra mass, the transient motion was also shown to have a longer period of oscillation, and the ship with 30% extra mass only had a slightly



(a) Heave motion.



(b) Surge motion.

Figure 6.21: Heave and surge motion of the heavier ships during the rogue wave impact.

longer period of oscillation. Since this oscillation was previously determined to oscillate at the natural frequency of the system, these results indicated that the mass of the ship can have a significant influence on the natural frequency of oscillation.

The pressures on the ships increased by approximately 20 kPa and 70 kPa for the 30% and 100% additional mass cargo cases. This corresponded to the change in hydrostatic pressures that the points were expected to observe. However, the pressure at point 1 (at the top of the bow) in Figure 6.22 showed that the 100% additional mass ship experienced significant non-zero pressures, indicating that the waves were impacting the deck and causing green water events. The 30% additional mass ship also showed some non-zero pressures at 308 seconds. These pressures are small in magnitude, which indicated that the surface of the water was very close to the bow and may be subject to green water if additional cargo were to be carried.

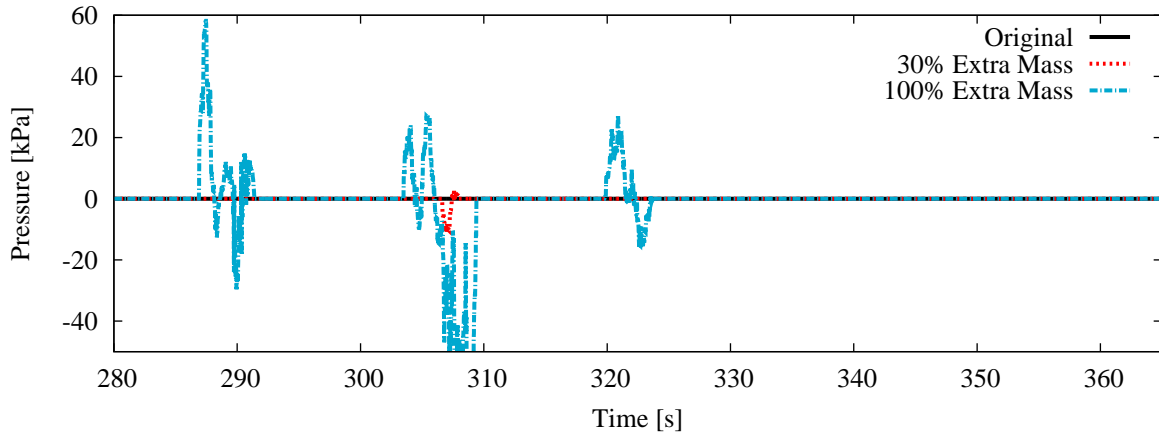


Figure 6.22: Pressure at point 1 (top of the bow) on the heavier ships during a rogue wave.

## 6.2.4 Coarser resolution

Computational resource constraints meant that not all of the simulations could be restarted from  $t = 0$  s at a particle spacing of 1 m. Although some simulations could be restarted from a snapshot at  $t = 265$  s, such as the higher stiffness or increased mass simulations, changes to the nature of the wave could not since the fluid particles in the snapshot would not have the correct waveform, and therefore these simulations must be started at  $t = 0$  s. To allow for these simulations to be performed within the resource constraints, a coarser particle spacing of 2 m was used.

This section quantifies the discrepancies between the original simulation and a new simulation with a coarser resolution. For a particle spacing of 2 m, the time taken for the simulations to resolve was a factor of 7 less than with a 1 m particle spacing.

In this comparative case, a particle spacing of 2 m corresponded to a background wave that is slightly larger than 2 particles in amplitude. This was shown in Section 6.1 to result in a rogue wave that was smaller in amplitude than expected. Figure 6.23 showed that the surface elevation of the rogue wave with the coarser resolution was surprisingly similar to the original 1 m particle spacing case. This consistency between the 1 m and 2 m particle spacings indicated that a 2 m particle spacing was adequate for modelling this rogue wave.

The heave and pitch motions were not significantly influenced by the coarser resolution. The surge motion had some differences between the simulations, and these are shown in Figure 6.24. In particular, the transient motion in the 2 m particle spacing case was under-predicted. This was similar to the 1 second period wave train cases (see Section 5.2.3). The background wave oscillations were actually similar to the 1 m particle spacing simulation.

As a consequence of the small differences in the surge trajectories, some differences were observed in the cable tensions (see Figure 6.25). The peak tension was under-predicted by 10%

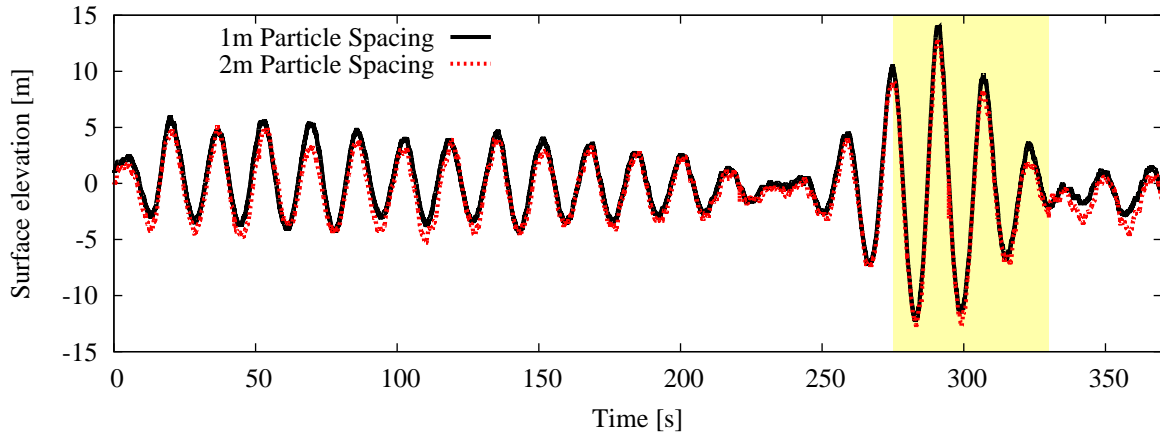


Figure 6.23: Surface elevation of the rogue wave with a mean particle spacing of 2 m.

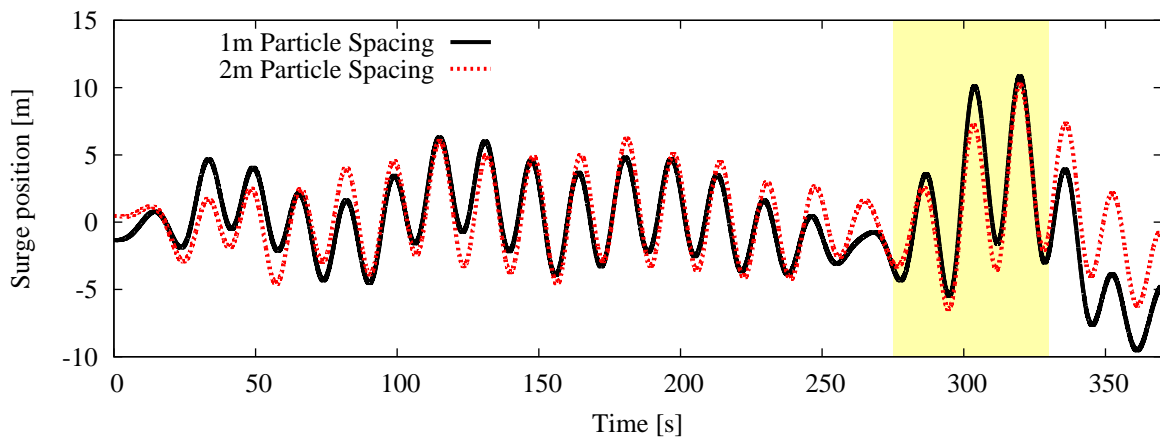


Figure 6.24: Surge trajectory of the ship in a rogue wave with a mean particle spacing of 2 m.

compared to the 1 m simulations, but the tensions when the ship was in the background sea state appeared to be slightly over-predicted.

Although the coarser resolution simulations cannot accurately model slamming pressures, the pressures at points 1, 2, and 4 were found to have approximately the same magnitude as the pressures at the same points in the 1 m case. However, the amplitude of the pressure oscillations at point 3 with a 2 m particle spacing was approximately half that of the 1 m case (see Figure 6.26). This suggested that the 1 m particle spacing case was modelling some slamming loads.

The magnitude of the pressures in the 2 m particle spacing case were approximately equivalent to the hydrostatic pressure expected at point 3's location at that time. Given that there was uncertainty about the accuracy of the slamming pressures in the 1 m particle spacing case, the coarser 2 m mean particle spacing was certainly inadequate for calculating the pressures on the front of the ship from slamming. However, since the cable tensions were predicted to be within 10% error for the coarser resolution, the 2 m particle spacing case can still be used for designing the cables and predicting the ship's trajectory.

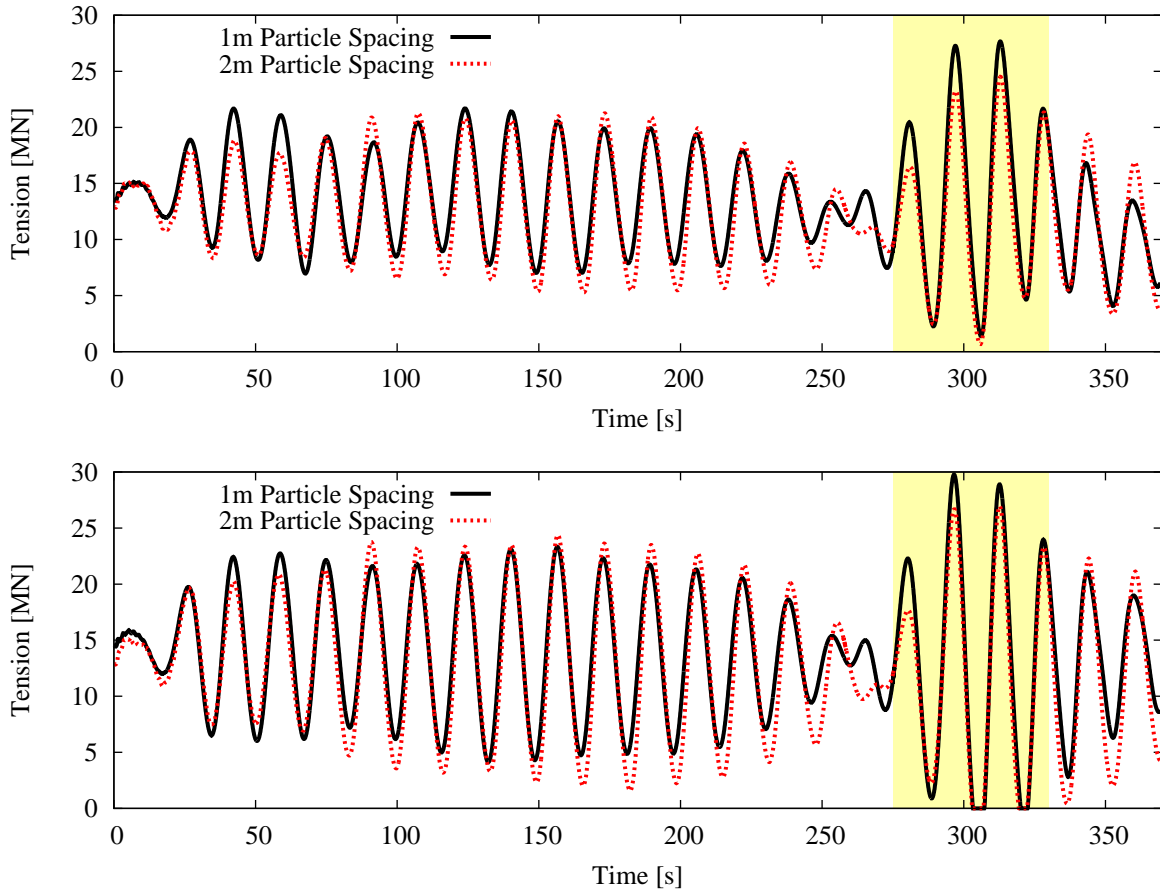


Figure 6.25: Tensions in the forward (top figure) and side (bottom figure) cables in a rogue wave impact for the simulation with 2 m mean particle spacing.

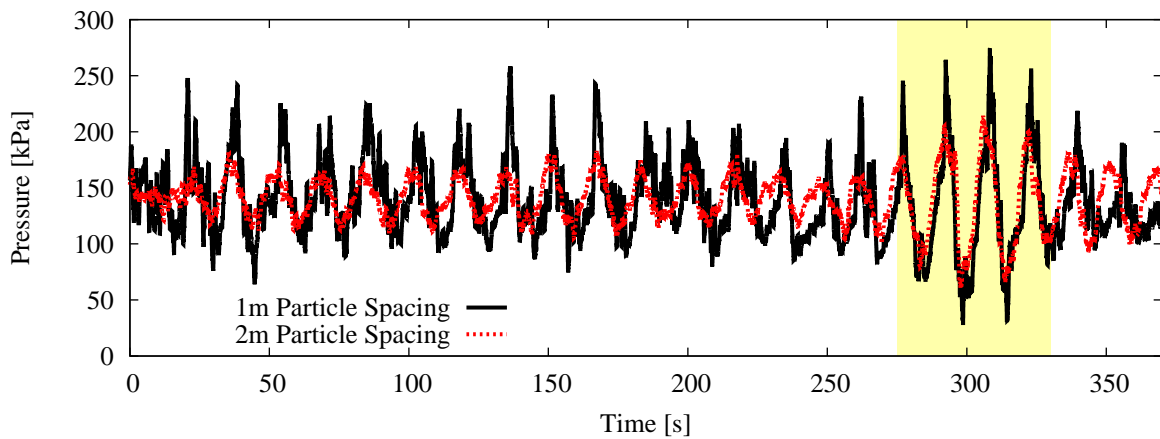


Figure 6.26: Comparison of pressures at sensor 3 for the 1 m and 2 m particle spacing cases.

### 6.2.5 Increasing the wavelength of the rogue wave

Many types of waves are possible in the ocean, not only with larger amplitudes, but also with longer wavelengths. To test the effect of this, a simulation was performed with an increased wavelength. Since this simulations was required to start at  $t = 0$  s, the coarser resolution of 2 m

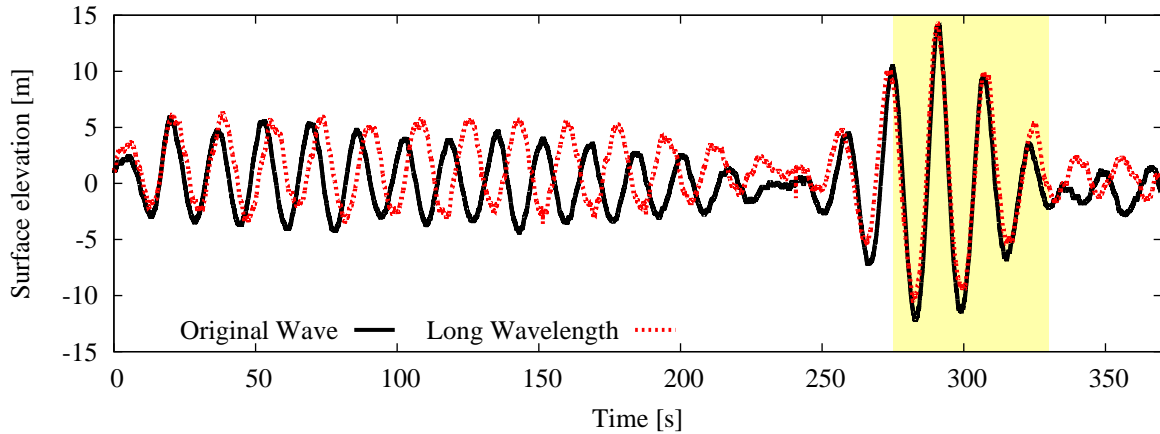


Figure 6.27: Surface elevation of a rogue wave with a longer wavelength.

particle spacing was used.

The wavelength of the background waves were doubled without changing their amplitude. This resulted in waves with half the steepness as was in the base case. The surface elevation of the longer wavelength rogue wave (see Figure 6.27) was shown to have a longer period between crests (due to the longer wavelength), but the overall amplitude of the waves was unchanged.

The heave response of the ship to the longer wavelength rogue wave (see Figure 6.28) was not significantly different, with the period of oscillation in the background wave different due to the changed wavelength. The surge motion, however, did differ with the change in wavelength. The transient motion in the background wave was damped, and this was due to the coarser particle spacing and increased period (as seen in Section 5.2.3). However, the transient motion in response to the rogue wave impact was seen to have a larger amplitude than the previous simulations.

Finally, the pressures on the ship were observed to remain reasonably similar to the original wave (with 2 m particle spacing). Since the pressures, when a particle spacing of 2 m was used, were known to incur an error, a direct comparison with the original 1 m particle spacing case was not useful. Instead, Figure 6.29 shows a comparison of the pressures between the longer wavelength rogue wave and the original test performed with 2 m particle spacing. The pressures were shown to fluctuate with similar amplitudes throughout the simulation, indicating that the change in wavelength had no effect on the pressures. Thus, if this simulation were to be performed with a particle spacing of 1 m, then pressures similar to the original case can be expected.

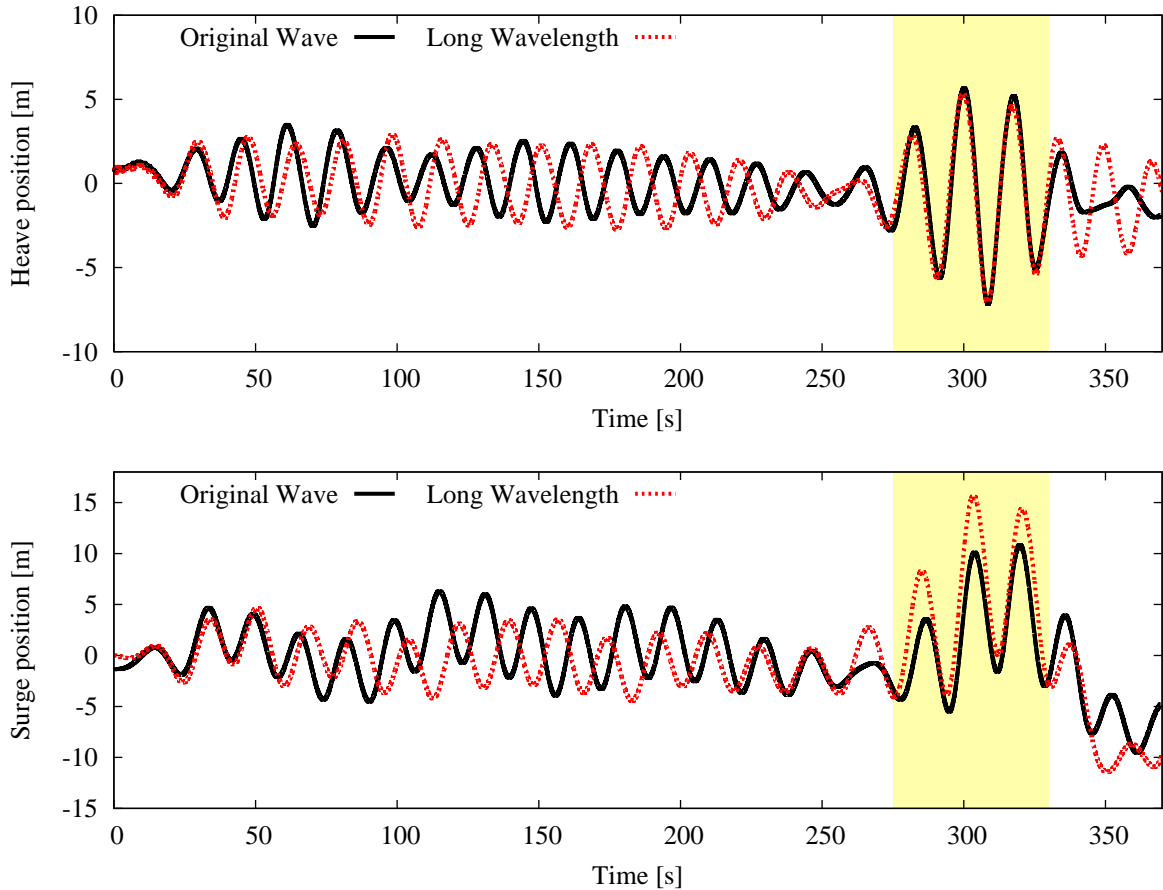


Figure 6.28: Trajectory of the ship in the heave (top figure) and surge (bottom figure) directions in response to the longer wavelength rogue wave impact.

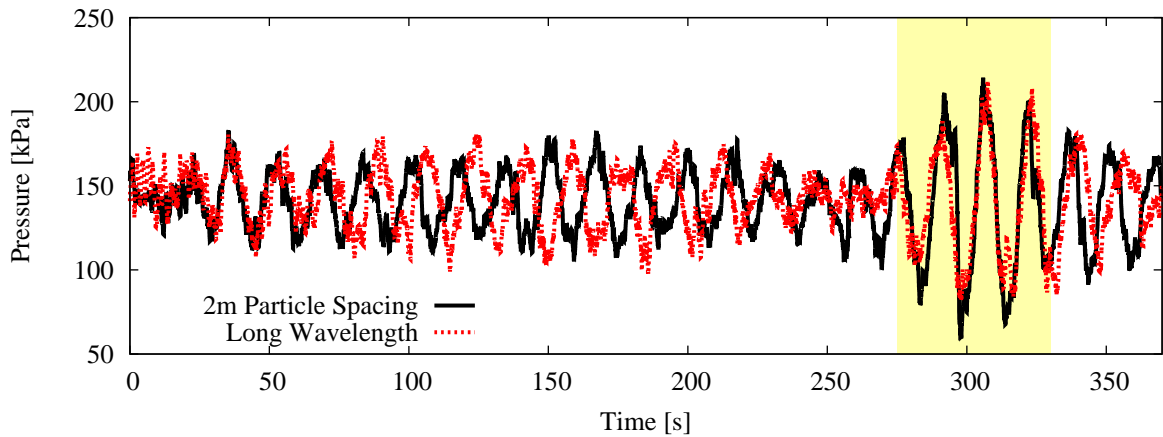


Figure 6.29: Pressure at sensor 3 during the longer wavelength rogue wave.

### 6.2.6 Simulating the impact of a 2<sup>nd</sup> order rogue wave

The first order rogue wave used in the previous cases measured at approximately 27 m wave height when it was at its maximum. However, the impact of a larger rogue wave will likely have more dire consequences. To investigate this, a second order rogue wave, with an amplification

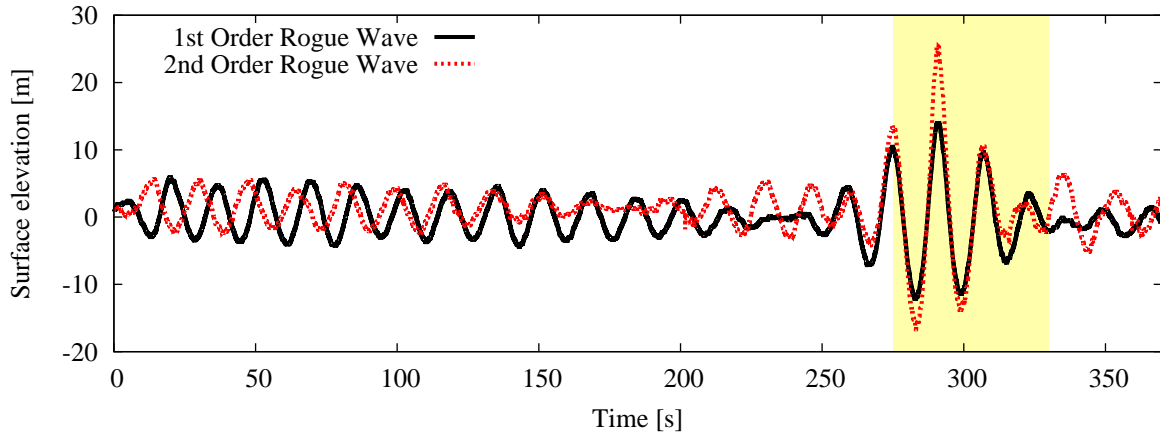


Figure 6.30: Surface elevation of the simulated first and second order rogue waves.

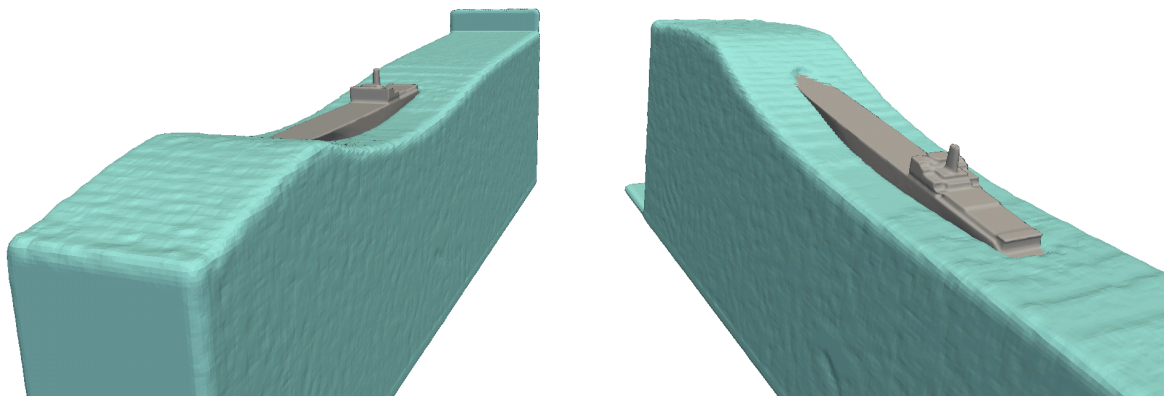
factor of 5, was simulated impacting the ship. This rogue wave had a height of nearly 45 m when the same background wave state was used. To simulate these waves, a 2 m particle spacing was used, and the wavelength was doubled compared to the base case in order to ensure that the maximum wave steepness ( $\varepsilon_b = 0.06$ ) for a second order wave was not exceeded.

Figure 6.30 shows the surface elevation of the second order rogue wave at a position of 27.9 m ahead of the bow of the ship, where the original simulation measured the surface elevation. It can be seen that the front face of the rogue wave has a height of 42 m, and the back face is 39.1 m high. This position was 50 m ahead of the rogue wave's theoretical peak height location, and the peak wave was expected to be larger than these heights.

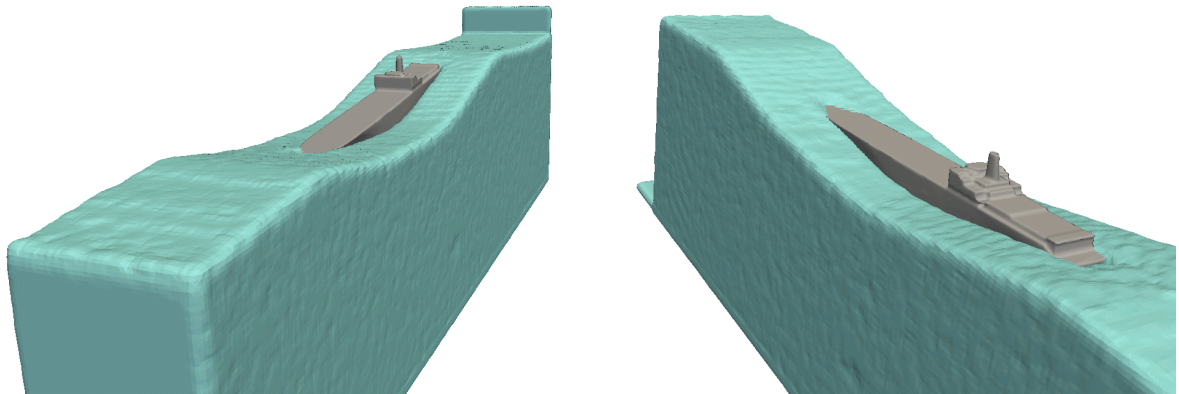
Despite the very large wave height of the second order rogue wave, the ship was not subjected to significant green water effects. A visualisation of the ship in the rogue wave is shown in Figure 6.31 at the times where the ship was most at risk of green water effects. Although the bow of this ship dips into the waves, the penetration was not deep enough for significant water to remain on the deck of the ship. Compared to Figure 6.12d, where the ship was at its greatest risk of green water on deck, it could be seen that for this second order wave the bow was closer to the surface of the waves. Consequently, the ship was at greater risk here than it was in the original simulation.

The motion of the ship in response to the impact of the second order rogue wave is shown in Figure 6.32. The range of the heave motion was larger during the rogue wave impact than it was in the base case, and this was expected as the rogue wave was much larger. The surge motion showed a small amount of transient motion in the background waves, but during the rogue wave impact the range of motion was approximately double that of the base case. This was due to the longer wavelength of the waves and the larger amplitude of the rogue wave providing a larger initial transient displacement.

Due to the reduced range of motion during the background wave, the tension in the mooring



(a)  $t = 294$  s



(b)  $t = 308$  s

Figure 6.31: Visualisation of the ship responding to a second order rogue wave.

cables did not have as large fluctuations as in the original case. This is shown for the side cables in Figure 6.33. The forward cable again did not have greater maximum tension than the side cables, so only the tensions of the side cables were considered. However, during the rogue wave the motion of the ship caused the maximum tension in the cables to exceed 40 MN.

The pressure at sensor point 3 is shown in Figure 6.34, compared with the first order case with a 2 m particle spacing. The magnitude of the pressure fluctuations were similar between the first and second order cases, only differing during the rogue wave impact where the waves were larger for the second order case. Previously, the 2 m particle spacing was shown to poorly model the slamming pressures, so the pressures observed here were primarily the hydrostatic pressures, hence the similarity between the two cases was not surprising. Since the amplitudes of motion were larger for the second order case, it could be expected that the slamming pressures would be larger. However, simulations at finer resolutions are required to determine these slamming loads.

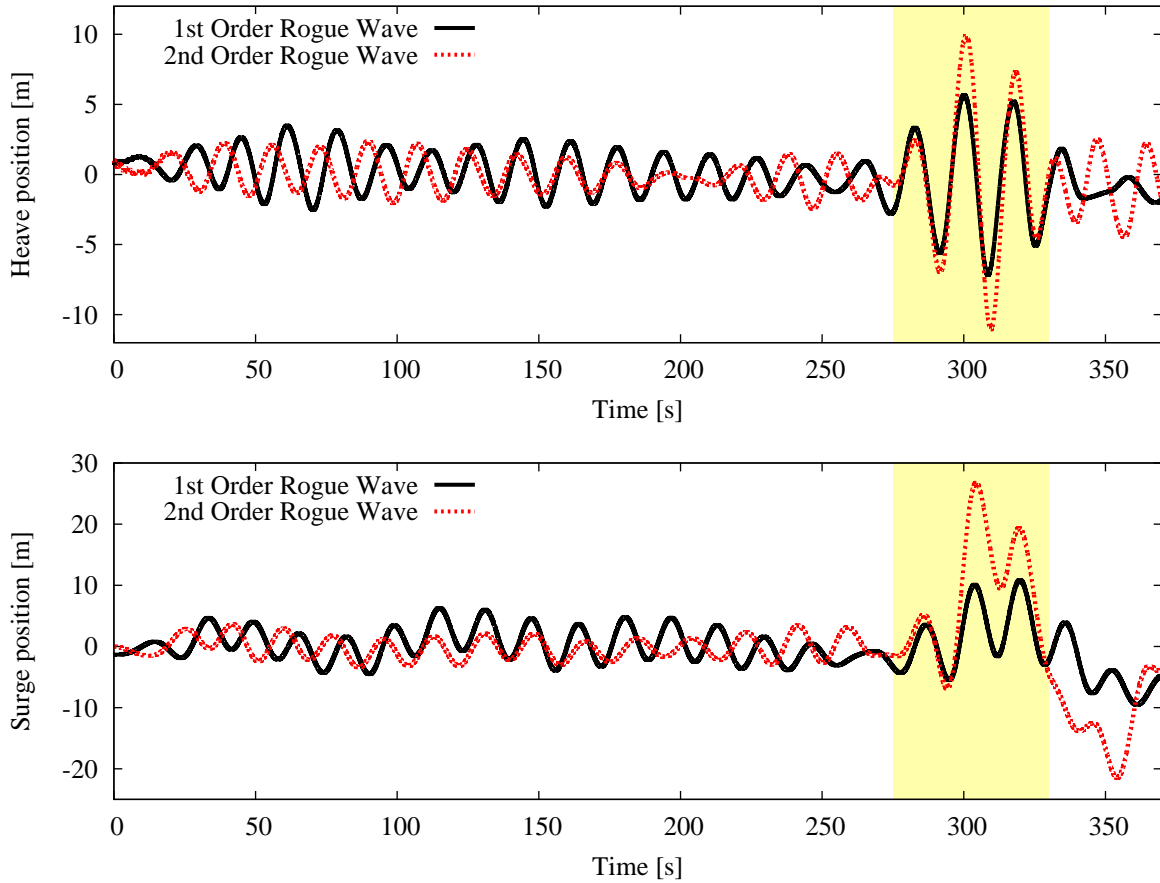


Figure 6.32: Trajectory of the ship in the heave (top figure) and surge (bottom figure) directions in response to the second order rogue wave impact.

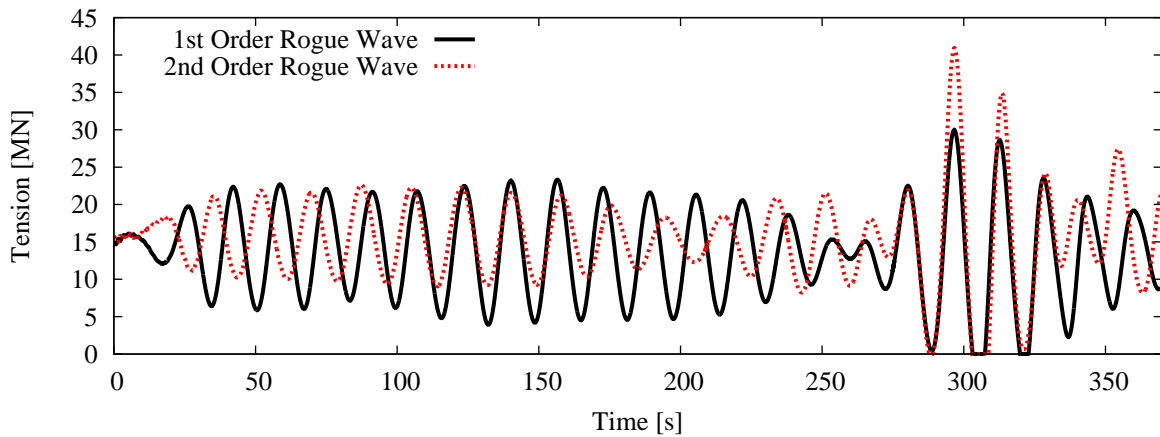


Figure 6.33: Tension of the side cables during the second order rogue wave impact, compared to the first order wave impact with particle spacing of 1 m

### 6.3 Summary

In this chapter, the efficacy of SPH was verified for modelling Peregrine breather type rogue waves of orders 1 and 2. Upon this verification, SPH was then used to simulate the impact of

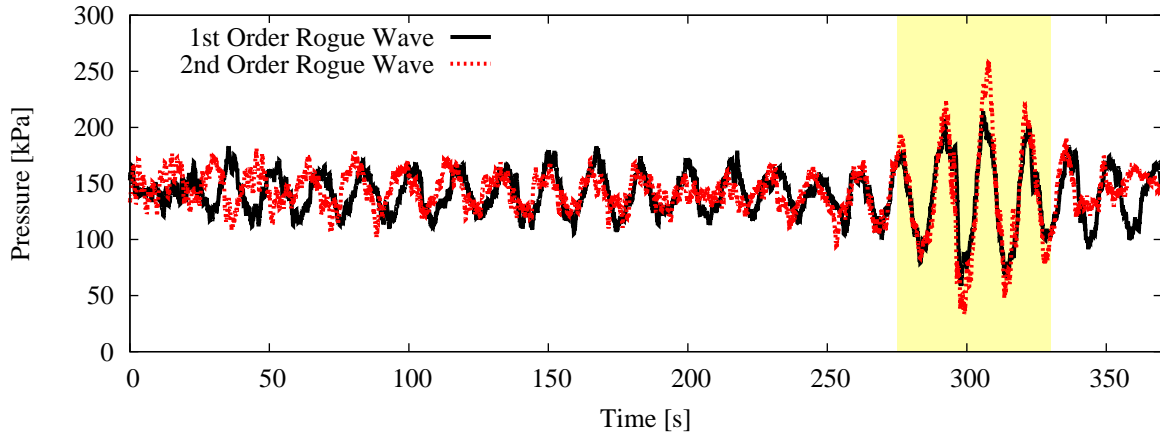


Figure 6.34: Pressure at sensor 3 during the second order rogue wave impact, compared to the first order wave impact with a particle spacing of 2 m.

these types of waves on a floating tethered body (i.e., a moored ship in this study) under varying conditions.

In the first section, Peregrine breather type rogue waves were experimentally generated and then replicated using 2D SPH simulations. This validated the efficacy of SPH to model these types of waves to a reasonable degree of accuracy. These simulations revealed that a minimum particle spacing to the background wave amplitude ratio of 1:5 was required for producing accurate breather waves. Furthermore, a simulated depth of at least 35 cm, equivalent to  $kd = 1.75$  in the second order rogue wave case, with free slip boundaries was required to ensure that the rogue waves were accurately modelled.

Simulations of a large scale rogue wave impacting on a tethered ship were then performed using 3D SPH. A particle spacing of 1 m was used in the simulation, and a rogue wave nearly 27 m in height was generated. The impact on the ship showed that the hull near the bow experienced large pressure peaks due to slamming into the waves, and the slamming pressures were smaller in amplitude the farther they were from the bow. Since the particle spacing was inadequate to model the typical mechanisms that caused large slamming pressures, there was uncertainty in the accuracy of the slamming pressures predicted. However, they were nevertheless present in the SPH simulations, suggesting that finer resolutions would be capable of accurately modelling those pressures.

A number of different tests were performed and compared to the base simulation to determine the effect of a different ship or wave properties. Firstly, the stiffness of the cables used to tether the ship was increased. It was found that increasing the stiffness had insignificant influence on the overall response of the ship to the rogue wave impact. This was likely due to the buoyancy forces on the ship being an order of magnitude greater than the tension forces in the cables. To obtain tension forces of the same order of magnitude as the buoyancy, then significantly higher stiffness values were required.

Next, the mass of the ship was increased. This had the effect of causing the ship to sit lower in the water, and the risk of green water effects was increased. Additionally, the amplitudes of motion were reduced as the ship's inertia was increased.

In order to reduce the computational effort required, the rogue wave impact was repeated using a coarser resolution of a 2 m mean particle spacing. It was found that the cable tensions were within 10% of the fine resolution case and the surface elevation was well modelled, however, the pressure predictions were poor along the front of the ship, and only modelling the hydrostatic pressures. Additionally, the transient surge motion of the ship was under-predicted, similar to the coarser resolution validation cases performed in earlier studies.

The wavelength of the waves was then doubled. It was found that the longer wavelength had little influence on the impact with the exception of inducing a larger amplitude transient motion in the surge direction. The order of the rogue wave was then increased, resulting in a wave that was over 42 m in height. Although this wave height is likely to be unrealistic, there was no significant green water effects observed on the ship. As was expected by the larger wave height, the ship's range of motion was increased in both the heave and surge directions.

# Chapter 7

## Conclusions

Designing an offshore vessel to survive a rogue wave impact is a difficult process as experimental data is difficult to obtain. To provide designers with a technique to assist in predicting the effect of a rogue wave impact, the aim of this research was to show the efficacy of Smoothed Particle Hydrodynamics in modelling such rogue wave impacts. To do this, this research covered a sequence of progressively more complex studies that validated SPH for modelling rogue waves and their interactions with a floating tethered body. Once validated, the SPH method was used to predict the effects of a rogue wave impact on a full scale moored ship.

In the first stage of the research, two preliminary studies were performed. The first of these aimed to determine the important parameters for calculating object boundaries and free surface locations using SPH. Due to the particle nature of SPH, exactly where the object and free surface boundaries were located was not clearly defined. In the boundary normal method, it was found that offsetting the boundaries by half a particle spacing yielded the most accurate representation for actual size of the buoy. However, when the object penetrated the surface of the fluid, the exact location of the free surface was needed to determine the correct proportion of the object that was submerged. The free surface location was estimated to be at the location where the particle density (or fraction of fluid in the vicinity) equalled a specific value,  $\xi_t$ . It was found that the free surface location was correct when the particle density was 80%, or  $\xi_t = 0.8$ .

Given the significant computational expense in running particular simulations, the second of the preliminary studies aimed to reduce computational cost. To do this, the number of particles required to perform the simulation was reduced. This was achieved by using a forcing region to generate the surface waves and periodic boundaries that allowed for the waves to re-enter the domain. In studying the forcing region method, it was found that the forcing factor,  $\kappa$ , was the most influential controlling parameter for generating waves of the desired amplitude, producing the most accurate wave amplitudes when  $\kappa = 0.7$ .

The next study in the research was to determine the accuracy of SPH when modelling the

interaction between surface waves and a floating tethered body in 3D. In a review of the SPH literature, there were few validation studies of SPH when modelling these scenarios. In addition, these studies considered only 2D SPH, or modelled untethered objects. To provide validation data for SPH for use in this research, experiments were performed in which measurements were made for the motion of a moored spherical buoy interacting with the free surface in a number of scenarios: oscillating vertically or horizontally across a still surface, or interacting with a sinusoidal wave train. The results of these experiments were then compared to predictions from the SPH method to determine the accuracy of SPH when modelling the moored buoy. It was found that a particle spacing equal to approximately  $1/40^{\text{th}}$  of the width or diameter of the object resulted in errors in the trajectory of less than 10% when compared to the experimental data. When a coarser particle spacing of 10 mm, or  $1/20^{\text{th}}$  of the buoy diameter was used, the error in the buoy motion increased to as high as approximately 35%. From these studies, it was determined that SPH could be used to accurately model the interaction of a floating tethered body on a free surface, provided that a particle spacing of order  $1/40^{\text{th}}$  of the width of the object is used.

The ability of SPH to model a rogue wave was then investigated by generating a rogue wave in experiments and using the experimental results to verify SPH simulations. Experimental studies had previously shown that Peregrine breather type waves could generate a rogue wave. However, a common criticism of using the Peregrine breather solution to model a rogue wave is that the fundamental generation mechanism (the Benjamin-Fier instability) does not occur in the ocean. Despite this, the resulting rogue wave is considered satisfactory, and these types of waves have not previously been modelled using SPH. Furthermore, the other proposed generation mechanisms are difficult or impossible to implement in SPH. Two Peregrine breather type rogue waves were generated experimentally in this study: a first order rogue wave that was three times larger than the background waves, and a second order rogue wave that was five times larger than the background wave. SPH was then used to model these two waves.

It was found that SPH was capable of accurately modelling these rogue waves when sufficient particle spacing was used. Unsurprisingly, the prediction of the rogue wave was poor when the particle spacing was  $1/2$  of the wave amplitude; however, refining the particle spacing to  $1/5^{\text{th}}$  of the amplitude gave a rogue wave height prediction that was within 5% error when compared to experimentally measured rogue waves. To reduce the number of particles required to simulate the wave, the depth of the water was varied, and it was found that using a depth condition of  $kd = 1.75$  or greater allowed the deep water conditions to be approximated closely enough to have no negative effect on the generated rogue wave. Thus, the SPH method has been shown to be capable of modelling a rogue wave to reasonable accuracy.

Finally, SPH was used to model a variety of impacts between rogue waves and a moored ship. A 27 m high Peregrine breather rogue wave was generated and its impact on an ocean scale moored floating ship was analysed. From the previously conducted studies in this research, the

magnitude of the errors was known and no experimental comparison was required. The tension in the mooring cables, the pressure at four points along the bow and hull, and the trajectory of the ship were all calculated in the simulation. It was found that SPH was capable of predicting the effect of the impact of a rogue wave on the ship. For this wave, the cable tension was found to be greater in the side cables, with a maximum tension of 30.0 MN. Additionally, a peak pressure on the hull of the ship of 275 kPa was observed. Although only 4 pressure measurement points were included in the simulation, using many more points would allow for a pressure map to be generated that can be used for Finite Element Analysis on the ship. It must be noted, however, that the particle spacing was too coarse to properly model the pressures during slamming, although some slamming events were predicted. Further refinement of the particle spacing is needed to obtain an accurate slamming model, but these simulations are currently too expensive to perform. Methods of reducing the computational time, such as variable resolution or more efficient computational resources, are an important area of research that will enable the use of SPH to predict the slamming loads on large scale vessels.

Additional simulations were then performed to investigate the effect of stiffer mooring cables, and the effect of additional mass (or additional cargo) on the ship when impacted by a rogue wave. The tension forces were found to have little influence on the motion of the ship since the buoyancy forces were an order of magnitude greater than the tension forces. For the heavier ship simulations, it was found that with 30% increased mass there were no green water effects, but when the mass was increased to double the original mass, then green water effects were observed. This result is unsurprising as heavier ships will sit lower in the water and so larger waves are more likely to crash onto the deck.

The original SPH simulation of the 27 m high Peregrine breather rogue wave had a long runtime. To reduce the computation expense, a coarser particle spacing was tested where the particle spacing was doubled, reducing the runtime by a factor of 8. It was found that the rogue wave was still well modelled (despite the particle spacing only being 1/2 of the carrier wave amplitude) and that the response of the ship was similar. However, the pressures on the ship were detrimentally affected by the resolution change, appearing only to capture the hydrostatic pressure and not any additional pressure from the waves crashing into the ship. Overall, the coarser resolution is acceptable, provided that the pressure measurements be treated with caution.

The coarser resolution was then used to model the impact of two different rogue waves: a first order rogue wave of 27 m height but with a longer wavelength, and a second order rogue wave with a maximum height of 42 m. Increasing the wavelength of the waves was found not to introduce green water effects since reduced steepness decreased the risk of the bow plunging into the waves. The second order wave was also found not to introduce any green water effects. This result was unexpected since the wave height was large. However, a visualisation of the impact showed that the bow of the ship was closer to the surface and thus the ship was more at risk of green water on deck than the original simulation. In both simulations, no conclusions

could be drawn about the effect on the pressures due to the reduced accuracy at this resolution.

From this research, it can be concluded that the efficacy of SPH has been established and that it is a viable method for modelling a rogue wave impact on a floating tethered body in the ocean. Coarser resolution studies can be used to model some aspects of the impact on the ship design, such as the tensions in the cable, but finer resolutions are required to accurately model the impact pressures on the ship. Furthermore, the validation work performed provided experimental data that will be useful in future studies to verify other simulation methods that attempt to simulate either the motion of a buoy interacting with a free surface, or the generation of a Peregrine breather rogue wave.

During this research, it was evident that to obtain very accurate simulations, fine resolution and long runtimes were required. While perhaps acceptable for research purposes, for industrial applications the lengthy runtimes are likely to be too expensive or time-consuming. Reducing the runtimes of the simulations would be a valuable improvement on the implementation of SPH that was used in this research. This can be done by performing the simulations on computational nodes with the capability for more massive parallel simulations, depending on the hardware used for the simulations. An alternative option is to enable the SPH simulations to be performed on GPUs, which are capable of significantly greater parallelisation per node than traditional CPUs.

If these long runtimes can be improved, the SPH method will become a valuable technique for industrial design applications in oceanography.

# Appendix A

## Motion capture algorithm

### A.1 Determining a ray of solutions

The coordinate transformation matrix given in Eq. (3.2) written as a set of equations is:

$$uw = c_{11}x + c_{12}y + c_{13}z + c_{14} \quad (\text{A.1})$$

$$uw = c_{21}x + c_{22}y + c_{23}z + c_{24} \quad (\text{A.2})$$

$$w = c_{31}x + c_{32}y + c_{33}z + c_{34} \quad (\text{A.3})$$

where the transformation matrix  $C$  is

$$C = \begin{bmatrix} c_{11} & c_{12} & c_{13} & c_{14} \\ c_{21} & c_{22} & c_{23} & c_{24} \\ c_{31} & c_{32} & c_{33} & c_{34} \end{bmatrix} \quad (\text{A.4})$$

substituting  $w$  into equations A.1 and A.2 gives:

$$u(c_{31}x + c_{32}y + c_{33}z + c_{34}) = c_{11}x + c_{12}y + c_{13}z + c_{14} \quad (\text{A.5})$$

$$v(c_{31}x + c_{32}y + c_{33}z + c_{34}) = c_{21}x + c_{22}y + c_{23}z + c_{24} \quad (\text{A.6})$$

which simplify to

$$(uc_{31} - c_{11})x + (uc_{32} - c_{12})y + (uc_{33} - c_{13})z = c_{14} - uc_{34} \quad (\text{A.7})$$

$$(vc_{31} - c_{21})x + (vc_{32} - c_{22})y + (vc_{33} - c_{23})z = c_{24} - vc_{34} \quad (\text{A.8})$$

or in matrix form:

$$\underbrace{\begin{bmatrix} uC_{31} - c_{11} & uC_{32} - c_{12} & uC_{33} - c_{13} \\ vC_{31} - c_{21} & vC_{32} - c_{22} & vC_{33} - c_{23} \end{bmatrix}}_B \underbrace{\begin{bmatrix} x \\ y \\ z \end{bmatrix}}_X = \underbrace{\begin{bmatrix} c_{14} - uC_{34} \\ c_{24} - vC_{34} \end{bmatrix}}_b \quad (\text{A.9})$$

This is an underdetermined system with two equations and three unknowns, so there are infinite solutions. The general solution is given by:

$$\mathbf{X} = \mathbf{X}_{homogeneous} + \mathbf{X}_{particular} \quad (\text{A.10})$$

The homogeneous solution is found from solving:

$$B\mathbf{X}_{homogeneous} = 0 \quad (\text{A.11})$$

where  $\mathbf{X}_{homogeneous}$  is in the nullspace of  $B$ . Let a non-trivial vector associated with this nullspace be  $\mathbf{r} = (r_x, r_y, r_z)$ . The particular solution, which is re-labelled to  $\mathbf{p} = (p_x, p_y, p_z)$ , is any possible solution to Eq. (A.9). One solution can be found using the pseudo inverse method:

$$\mathbf{p} = B^T(BB^T)^{-1}b \quad (\text{A.12})$$

Thus the general solution of global coordinates is:

$$\mathbf{X} = t \cdot \mathbf{r} + \mathbf{p}, t \in \mathbb{R} \quad (\text{A.13})$$

## A.2 Determining a global coordinate from many rays

Due to the infinite number of solutions that can be obtained from a single camera view, a second view was required to obtain a single unique solution. Realistically, there will be some error in either the cameras, or the human identification of the pixel-coordinates of a point. Figure A.1 shows an example of a three camera view where the errors prevent a unique solution from forming. Consequently, a least squares method approach was adopted to determine the closest solution to the lines of solutions from the cameras, by minimising the distances from the point to the lines (see Figure A.2).

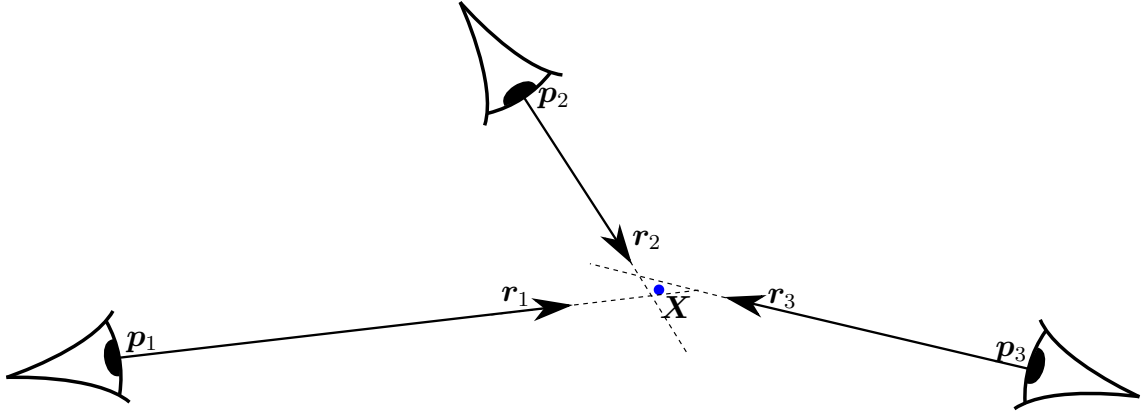


Figure A.1: The errors in the rays of the three camera view prevent a single global coordinate being agreed upon.

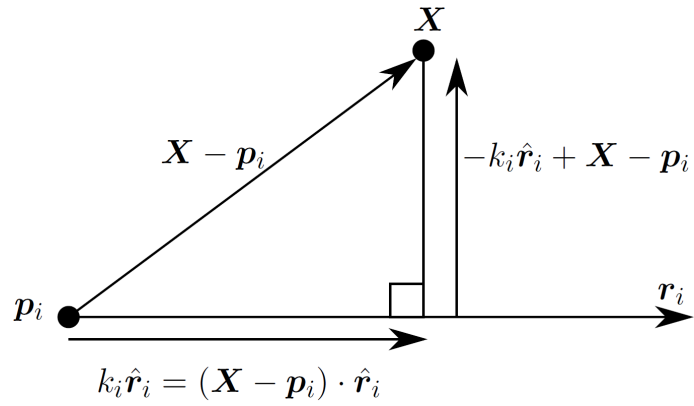


Figure A.2: Distance of a point to a line for camera  $i$ .

The shortest distance of the point to the line is given by:

$$d_i = |\mathbf{X} - \mathbf{p}_i - k_i \hat{\mathbf{r}}_i| \quad (\text{A.14})$$

$$= |\mathbf{X} - \mathbf{p}_i| |(\mathbf{X} - \mathbf{p}_i) \cdot \hat{\mathbf{r}}_i| \quad (\text{A.15})$$

$$d_i^2 = (x - p_{ix} - ((\mathbf{X} - \mathbf{p}_i) \cdot \hat{\mathbf{r}}_i) \hat{r}_{ix})^2 + (y - p_{iy} - ((\mathbf{X} - \mathbf{p}_i) \cdot \hat{\mathbf{r}}_i) \hat{r}_{iy})^2 + (z - p_{iz} - ((\mathbf{X} - \mathbf{p}_i) \cdot \hat{\mathbf{r}}_i) \hat{r}_{iz})^2 \quad (\text{A.16})$$

The total error is then defined as:

$$E = \sum_i d_i^2 \quad (\text{A.17})$$

$$= \sum_i (x - p_{ix} - ((\mathbf{X} - \mathbf{p}_i) \cdot \hat{\mathbf{r}}_i) \hat{r}_{ix})^2 + (y - p_{iy} - ((\mathbf{X} - \mathbf{p}_i) \cdot \hat{\mathbf{r}}_i) \hat{r}_{iy})^2 \quad (\text{A.18})$$

$$+ (z - p_{iz} - ((\mathbf{X} - \mathbf{p}_i) \cdot \hat{\mathbf{r}}_i) \hat{r}_{iz})^2$$

$$= \sum_i (x - p_{ix} + (\mathbf{p}_i \cdot \hat{\mathbf{r}}_i) \hat{r}_{ix} - (x \hat{r}_{ix} + y \hat{r}_{iy} + z \hat{r}_{iz}) \hat{r}_{ix})^2 \quad (\text{A.19})$$

$$+ (y - p_{iy} + (\mathbf{p}_i \cdot \hat{\mathbf{r}}_i) \hat{r}_{iy} - (x \hat{r}_{ix} + y \hat{r}_{iy} + z \hat{r}_{iz}) \hat{r}_{iy})^2$$

$$+ (z - p_{iz} + (\mathbf{p}_i \cdot \hat{\mathbf{r}}_i) \hat{r}_{iz} - (x \hat{r}_{ix} + y \hat{r}_{iy} + z \hat{r}_{iz}) \hat{r}_{iz})^2$$

$$= \sum_i (x(1 - \hat{r}_{ix} \hat{r}_{ix}) + y(-\hat{r}_{ix} \hat{r}_{iy}) + z(-\hat{r}_{ix} \hat{r}_{iz}) + (-p_{ix} + (\mathbf{p} \cdot \hat{\mathbf{r}}_i) \hat{r}_{ix}))^2 \quad (\text{A.20})$$

$$+ (x(\hat{r}_{ix} \hat{r}_{iy}) + y(1 - \hat{r}_{iy} \hat{r}_{iy}) + z(-\hat{r}_{iy} \hat{r}_{iz}) + (-p_{iy} + (\mathbf{p} \cdot \hat{\mathbf{r}}_i) \hat{r}_{iy}))^2$$

$$+ (x(\hat{r}_{ix} \hat{r}_{iz}) + y(-\hat{r}_{iy} \hat{r}_{iz}) + z(1 - \hat{r}_{iz} \hat{r}_{iz}) + (-p_{iz} + (\mathbf{p} \cdot \hat{\mathbf{r}}_i) \hat{r}_{iz}))^2$$

The optimisation of  $E$  has a solution when the derivatives of  $E$  are 0. The derivatives are given by:

$$\frac{\partial E}{\partial x} = \sum_i x [(1 - \hat{r}_{ix} \hat{r}_{ix})(1 - \hat{r}_{ix} \hat{r}_{ix}) + (-\hat{r}_{ix} \hat{r}_{iy})(-\hat{r}_{ix} \hat{r}_{iy}) + (-\hat{r}_{ix} \hat{r}_{iz})(-\hat{r}_{ix} \hat{r}_{iz})] \quad (\text{A.21})$$

$$+ y [(-\hat{r}_{ix} \hat{r}_{iy})(1 - \hat{r}_{ix} \hat{r}_{ix}) + (1 - \hat{r}_{iy} \hat{r}_{iy})(-\hat{r}_{ix} \hat{r}_{iy}) + (-\hat{r}_{iy} \hat{r}_{iz})(-\hat{r}_{ix} \hat{r}_{iz})]$$

$$+ z [(-\hat{r}_{ix} \hat{r}_{iz})(1 - \hat{r}_{ix} \hat{r}_{ix}) + (-\hat{r}_{iy} \hat{r}_{iz})(-\hat{r}_{ix} \hat{r}_{iy}) + (1 - \hat{r}_{iz} \hat{r}_{iz})(-\hat{r}_{ix} \hat{r}_{iz})]$$

$$+ [(-p_{ix} + (\mathbf{p}_i \cdot \hat{\mathbf{r}}_i) \hat{r}_{ix})(1 - \hat{r}_{ix} \hat{r}_{ix}) + (-p_{iy} + (\mathbf{p}_i \cdot \hat{\mathbf{r}}_i) \hat{r}_{iy})(-\hat{r}_{ix} \hat{r}_{iy})$$

$$+ (-p_{iz} + (\mathbf{p}_i \cdot \hat{\mathbf{r}}_i) \hat{r}_{iz})(-\hat{r}_{ix} \hat{r}_{iz})]$$

$$\frac{\partial E}{\partial y} = \sum_i x [(1 - \hat{r}_{ix} \hat{r}_{ix})(-\hat{r}_{ix} \hat{r}_{iy}) + (-\hat{r}_{ix} \hat{r}_{iy})(1 - \hat{r}_{iy} \hat{r}_{iy}) + (-\hat{r}_{ix} \hat{r}_{iz})(-\hat{r}_{iy} \hat{r}_{iz})] \quad (\text{A.22})$$

$$+ y [(-\hat{r}_{ix} \hat{r}_{iy})(-\hat{r}_{ix} \hat{r}_{iy}) + (1 - \hat{r}_{iy} \hat{r}_{iy})(1 - \hat{r}_{iy} \hat{r}_{iy}) + (-\hat{r}_{iy} \hat{r}_{iz})(-\hat{r}_{iy} \hat{r}_{iz})]$$

$$+ z [(-\hat{r}_{ix} \hat{r}_{iy})(-\hat{r}_{ix} \hat{r}_{iy}) + (-\hat{r}_{iy} \hat{r}_{iz})(1 - \hat{r}_{iy} \hat{r}_{iy}) + (1 - \hat{r}_{iz} \hat{r}_{iz})(-\hat{r}_{iy} \hat{r}_{iz})]$$

$$+ [(-p_{ix} + (\mathbf{p}_i \cdot \hat{\mathbf{r}}_i) \hat{r}_{ix})(-\hat{r}_{ix} \hat{r}_{iy}) + (-p_{iy} + (\mathbf{p}_i \cdot \hat{\mathbf{r}}_i) \hat{r}_{iy})(1 - \hat{r}_{iy} \hat{r}_{iy})$$

$$+ (-p_{iz} + (\mathbf{p}_i \cdot \hat{\mathbf{r}}_i) \hat{r}_{iz})(-\hat{r}_{ix} \hat{r}_{iz})]$$

$$\begin{aligned}
\frac{\partial E}{\partial z} = \sum_i x & [(1 - \hat{r}_{ix}\hat{r}_{ix})(-\hat{r}_{ix}\hat{r}_{iz}) + (-\hat{r}_{ix}\hat{r}_{iy})(-\hat{r}_{iy}\hat{r}_{iz}) + (-\hat{r}_{ix}\hat{r}_{iz})(1 - \hat{r}_{iz}\hat{r}_{iz})] \quad (\text{A.23}) \\
& + y [(-\hat{r}_{ix}\hat{r}_{iy})(-\hat{r}_{ix}\hat{r}_{iz}) + (1 - \hat{r}_{iy}\hat{r}_{iy})(-\hat{r}_{iy}\hat{r}_{iz}) + (-\hat{r}_{iy}\hat{r}_{iz})(1 - \hat{r}_{iz}\hat{r}_{iz})] \\
& + z [(-\hat{r}_{ix}\hat{r}_{iy})(-\hat{r}_{ix}\hat{r}_{iz}) + (-\hat{r}_{iy}\hat{r}_{iz})(-\hat{r}_{iy}\hat{r}_{iz}) + (1 - \hat{r}_{iz}\hat{r}_{iz})(1 - \hat{r}_{iz}\hat{r}_{iz})] \\
& + [(-p_{ix} + (\mathbf{p}_i \cdot \hat{\mathbf{r}}_i)\hat{r}_{ix})(-\hat{r}_{ix}\hat{r}_{iz}) + (-p_{iy} + (\mathbf{p}_i \cdot \hat{\mathbf{r}}_i)\hat{r}_{iy})(-\hat{r}_{iy}\hat{r}_{iz}) \\
& + (-p_{iz} + (\mathbf{p}_i \cdot \hat{\mathbf{r}}_i)\hat{r}_{iz})(1 - \hat{r}_{iz}\hat{r}_{iz})]
\end{aligned}$$

These derivatives can be simplified algebraically:

$$\frac{\partial E}{\partial x} = \sum_i \alpha_{ix}x + \beta_{ix}y + \gamma_{ix}z + b_{ix} \quad (\text{A.24})$$

$$\begin{aligned}
& = x \sum_i \alpha_{ix} + y \sum_i \beta_{ix} + z \sum_i \gamma_{ix} + \sum_i b_{ix} \\
& = \alpha_x x + \beta_x y + \gamma_x z + b_x = 0
\end{aligned}$$

$$\frac{\partial E}{\partial y} = \sum_i \alpha_{iy}x + \beta_{iy}y + \gamma_{iy}z + b_{iy} \quad (\text{A.25})$$

$$\begin{aligned}
& = x \sum_i \alpha_{iy} + y \sum_i \beta_{iy} + z \sum_i \gamma_{iy} + \sum_i b_{iy} \\
& = \alpha_y x + \beta_y y + \gamma_y z + b_y = 0
\end{aligned}$$

$$\frac{\partial E}{\partial z} = \sum_i \alpha_{iz}x + \beta_{iz}y + \gamma_{iz}z + b_{iz} \quad (\text{A.26})$$

$$\begin{aligned}
& = x \sum_i \alpha_{iz} + y \sum_i \beta_{iz} + z \sum_i \gamma_{iz} + \sum_i b_{iz} \\
& = \alpha_z x + \beta_z y + \gamma_z z + b_z = 0
\end{aligned}$$

which provides a linear system of equations,

$$\begin{bmatrix} \alpha_x & \beta_x & \gamma_x \\ \alpha_y & \beta_y & \gamma_y \\ \alpha_z & \beta_z & \gamma_z \end{bmatrix} \begin{bmatrix} x \\ y \\ z \end{bmatrix} = \begin{bmatrix} -b_x \\ -b_y \\ -b_z \end{bmatrix} \quad (\text{A.27})$$

that can be solved to obtain the global coordinates of the point, as required. However, if all of the rays are parallel, there will be an infinite number of solutions. With three or more well located cameras this scenario is highly unlikely to occur, and with two camera views it only occurs when the point being tracked is on or near the line between the two cameras.

# References

- N. Akhmedieva, V. Eleonskii, and N. Kulagin. Generation of a periodic sequence of picosecond pulses in an optical fiber-exact solutions. *Zhurnal Eksperimentalnoi i Teoreticheskoi Fiziki*, 89:1542–1551, 1985.
- T. E. Baldock and C. Swan. Numerical calculations of large transient water waves. *Applied Ocean Research*, 16(2):101–112, 1994.
- T. E. Baldock, C. Swan, and P. H. Taylor. A Laboratory Study of Nonlinear Surface Waves on Water. *Philosophical Transactions: Mathematical, Physical and Engineering Sciences*, 354 (1707):649–676, March 1996.
- J. Bašić, N. Degiuli, and A. Werner. Simulation of water entry and exit of a circular cylinder using the isph method. *Transactions of FAMENA*, 38(1):45–62, 2014.
- T. B. Benjamin and J. Feir. The disintegration of wave trains on deep water part 1. theory. *Journal of Fluid Mechanics*, 27(03):417–430, 1967.
- S. Birkholz, E. T. J. Nibbering, C. Brée, S. Skupin, A. Demircan, G. Genty, and G. Steinmeyer. Spatiotemporal rogue events in optical multiple filamentation. *Physical Review Letters*, 111: 243903, 2013.
- S. Birkholz, C. Brée, A. Demircan, and G. Steinmeyer. Predictability of rogue events. *Physical Review Letters*, 114:213901, May 2015. doi: 10.1103/PhysRevLett.114.213901. URL <http://link.aps.org/doi/10.1103/PhysRevLett.114.213901>.
- B. Bouscasse, A. Colagrossi, S. Marrone, and M. Antuono. Nonlinear water wave interaction with floating bodies in SPH. *Journal of Fluids and Structures*, 42:112–129, 2013.
- C. Brandini and S. Grilli. Modeling of freak wave generation in a 3d-nwt. In *The Eleventh International Offshore and Polar Engineering Conference*. International Society of Offshore and Polar Engineers, 2001.
- A. Calini and C. M. Schober. Homoclinic chaos increases the likelihood of rogue wave formation. *Physics Letters A*, 298(5):335–349, 2002.

- J. C. Campbell and R. Vignjevic. Simulating structural response to water impact. *International Journal of Impact Engineering*, 49:1–10, 2012.
- T. Capone, A. Panizzo, C. Cecioni, and R. A. Darlymple. Accuracy and stability of numerical schemes in SPH. In *2nd SPHERIC international workshop*, 2007.
- A. Chabchoub, N. Akhmediev, and N. P. Hoffmann. Experimental study of spatiotemporally localized surface gravity water waves. *Physical Review E*, 86(1):016311, 2012a.
- A. Chabchoub, N. P. Hoffmann, M. Onorato, A. Slunyaev, A. Sergeeva, E. Pelinovsky, and N. Akhmediev. Observation of a hierarchy of up to fifth-order rogue waves in a water tank. *Physical Review E*, 86(5):056601, 2012b.
- A. Chabchoub, B. Kibler, C. Finot, G. Millot, M. Onorato, J. M. Dudley, and A. V. Babanin. The nonlinear schrödinger equation and the propagation of weakly nonlinear waves in optical fibers and on the water surface. *Annals of Physics*, 361:490–500, 2015.
- A. Chabchoub, N. P. Hoffmann, and N. Akhmediev. Rogue Wave Observation in a Water Wave Tank. *Physical Review Letters*, 106(204502):1–4, May 2011.
- G. F. Clauss. Dramas of the sea: episodic waves and their impact on offshore structures. *Applied Ocean Research*, 24(3):147–161, Jun 2002.
- G. F. Clauss and C. E. Schmittner. Experimental Optimization of Extreme Wave Sequences for the Deterministic Analysis of Wave/Structure Interaction. *Journal of Offshore Mechanics and Arctic Engineering*, 129:61–67, February 2007.
- G. F. Clauss, C. E. Schmittner, and K. Stutz. Freak Wave Impact on Semisubmersibles — Time-domain Analysis of Motions and Forces. In *Proceedings of The Thirteenth (2003) International Offshore and Polar Engineering Conference*, pages 449–456, 2003. Honolulu, Hawaii, USA, May 25-30.
- P. W. Cleary. Modelling confined multi-material heat and mass flows using sph. *Applied Mathematical Modelling*, 22(12):981–993, 1998.
- C. Corte and S. T. Grilli. Numerical modeling of extreme wave slamming on cylindrical offshore support structures. In *The Sixteenth International Offshore and Polar Engineering Conference*. International Society of Offshore and Polar Engineers, 2006.
- S. J. Cummins and M. Rudman. An SPH projection Method. *journal of Computational Physics*, 152:584–607, 1999.
- S. J. Cummins, T. B. Silvester, and P. W. Cleary. Three-dimensional wave impact on a rigid structure using smoothed particle hydrodynamics. *International journal for numerical methods in fluids*, 68(12):1471–1496, 2012.

- T. A. I. de Vuyst. *Hydrocode modelling of water impact*. PhD thesis, Cranfield University, UK, 2003.
- D. G. Dommermuth and D. K. Yue. A high-order spectral method for the study of nonlinear gravity waves. *Journal of Fluid Mechanics*, 184:267–288, 1987.
- M. Doring, G. Oger, B. Alessandrini, and P. Ferrant. SPH Simulations of Floating Bodies in Waves. In *Proceedings of OMAE04, 23rd International Conference on Offshore Mechanics and Arctic Engineering*, 2004. Vancouver, British Columbia, Canada, June 20-25.
- L. Draper. ‘Freak’ Ocean Waves. *Oceanus*, 4:12–15, 1964.
- L. Draper. Severe wave conditions at sea. *J. Inst. Navig*, 24:273–277, 1971.
- G. Ducrozet, F. Bonnefoy, D. Le Touzé, and P. Ferrant. 3-D HOS simulations of extreme waves in open seas. *Natural Hazards and Earth System Science*, 7(1):109–122, 2007.
- O. El Moctar, A. Brehm, and T. E. Schellin. Prediction of slamming loads for ship structural design using potential flow and rrans codes. In *Proceedings of the 25th Symposium on Naval Hydrodynamics*, 2004. St. John’s.
- D. Faulkner. Rogue waves: Defining their characteristics for marine design, Rogue Waves 2000. In *Proceedings of a Workshop*, 2000.
- D. Faulkner and W. H. Buckley. Critical survival conditions for ship design. In *RINA International Conference: Design and Operation for Abnormal Conditions, Glasgow, Scotland*, 1997.
- F. Fedele, J. Brennan, S. P. De León, J. Dudley, and F. Dias. Real world ocean rogue waves explained without the modulational instability. *Scientific reports*, 6, 2016.
- G. Fekken. Numerical Simulation of Free-Surface Flow with Moving Rigid Bodies. Master’s thesis, University of Groningen, Groningen, Netherlands, 2004.
- L. Fernandez, M. Onorato, J. Monbaliu, and A. Toffoli. Occurrence of extreme waves in finite water depth. In *Extreme Ocean Waves*, pages 45–62. Springer, 2016.
- C. Fochesato, S. Grilli, and F. Dias. Numerical modeling of extreme rogue waves generated by directional energy focusing. *Wave Motion*, 44(5):395–416, 2007.
- N. Fonseca, R. Pascoal, C. Guedes Soares, G. F. Clauss, and C. Schmittner. Numerical and experimental analysis of extreme wave induced vertical bending moments on a FPSO. *Applied Ocean Research*, 32:374–390, 2010.
- G. Fouche and N. Adomaitis. North Sea Storm Forces Oil Platform Evacuations, Output Shutdown. REUTERS, December 2015. URL <http://www.reuters.com/article/us-weather-northsea-idUSKBN0UE00R20151231>. [accessed 23 May, 2016].

- R. A. Gingold and J. J. Monaghan. Smoothed particle hydrodynamics: theory and application to non-spherical stars. *Mon. Not. R. Astr. Soc.*, 181:375–389, 1977.
- H. Gotoh, H. Ikari, T. Memita, and T. Sakai. Lagrangian particle method for simulation of wave overtopping on a vertical seawall. *Coastal Engineering Journal*, 47(2 & 3):157–181, 2005.
- H. Gotoh, A. Khayyer, H. Ikari, T. Arikawa, and K. Shimosako. On enhancement of incompressible sph method for simulation of violent sloshing flows. *Applied Ocean Research*, 46: 104–115, 2014.
- S. T. Grilli, P. Guyenne, and F. Dias. A fully non-linear model for three-dimensional overturning waves over an arbitrary bottom. *International Journal for Numerical Methods in Fluids*, 35 (7):829–867, 2001.
- P.-M. Guilcher, N. Couty, L. Brosset, D. Le Touzé, et al. Simulations of breaking wave impacts on a rigid wall at two different scales with a two-phase fluid compressible sph model. *International Journal of Offshore and Polar Engineering*, 23(04):241–253, 2013.
- K. B. Haugen, F. Løvholt, and C. B. Harbitz. Fundamental mechanisms for tsunami generation by submarine mass flows in idealised geometries. *Marine and Petroleum Geology*, 22(1): 209–217, 2005.
- S. Haver. A possible freak wave event measured at the draupner jacket january 1 1995. *Rogue waves 2004*, pages 1–8, 2004.
- S. Haver and O. J. Andersen. Freak Waves: Rare Realizations of a Typical Population or Typical Realizations of a Rare Population? In *Proceedings of the Tenth (2000) International Offshore and Polar Engineering Conference*, 2000. Seattle, USA, May 28 - June 2.
- S. Haver and D. Karunakaran. Probabilistic description of crest heights of ocean waves. In *Proceedings of the Fifth International Workshop on Wave Hindcasting and Forecasting*, pages 26–30, 1998.
- K. L. Henderson, D. H. Peregrine, and J. W. Dold. Unsteady water wave modulations: fully nonlinear solutions and comparison with the nonlinear schrödinger equation. *Wave motion*, 29(4):341–361, 1999.
- M. J. Kaiser, Y. Yu, and C. J. Jablonowski. Modeling lost production from destroyed platforms in the 2004–2005 gulf of mexico hurricane seasons. *Energy*, 34(9):1156–1171, 2009.
- N. Karjanto. *Mathematical aspects of extreme water waves*. PhD thesis, University of Twente, 2006.
- N. Karjanto and E. Van Groesen. Qualitative comparisons of experimental results on deterministic freak wave generation based on modulational instability. *Journal of Hydro-Environment Research*, 3(4):186–192, 2010.

- C. Kharif and E. Pelinovsky. Physical mechanisms of the rogue wave phenomenon. *European Journal of Mechanics-B/Fluids*, 22(6):603–634, 2003.
- C. Kharif, E. Pelinovsky, and A. Slunyaev. *Rogue waves in the ocean*. Springer, 2009.
- A. Khayyer, H. Gotoh, and S. D. Shao. Corrected incompressible sph method for accurate water-surface tracking in breaking waves. *Coastal Engineering*, 55(3):236–250, 2008.
- A. Khayyer, H. Gotoh, and S. Shao. Enhanced predictions of wave impact pressure by improved incompressible sph methods. *Applied Ocean Research*, 31(2):111–131, 2009.
- B. Kibler, J. Fatome, C. Finot, G. Millot, F. Dias, G. Genty, N. Akhmediev, and J. M. Dudley. The peregrine soliton in nonlinear fibre optics. *Nature Physics*, 6(10):790–795, 2010.
- S. P. Kjeldsen. Examples of heavy weather damages caused by giant waves. *Bulletin of the Society of Naval Architects of Japan*, 820(10):24–28, 1997.
- Kraainnest, 2012. URL [https://commons.wikimedia.org/wiki/File:Water\\_wave\\_theories.svg](https://commons.wikimedia.org/wiki/File:Water_wave_theories.svg). [accessed 31 March, 2016].
- A. M. Laird. Observed Statistics of Extreme Waves. Master’s thesis, Naval Postgraduate School, Monterey, California, 2006.
- C. Landsea. NOAA Hurricane Research Division FAQ - How many hurricanes have there been in each month?. National Oceanic & Atmospheric Administration, May 2013. URL <http://www.aoml.noaa.gov/hrd/tcfaq/E17.html>. [accessed 6 February, 2014].
- B. Le Méhauté. *An Introduction to Hydrodynamics and Water Waves*. Springer Science & Business Media, 1976.
- D. Le Touzé, A. Colagrossi, G. Colicchio, and M. Greco. A critical investigation of smoothed particle hydrodynamics applied to problems with free-surfaces. *International Journal for Numerical Methods in Fluids*, 73(7):660–691, 2013.
- D. Le Touzé, A. Marsh, G. Oger, P. M. Guilcher, C. Khaddaj-Mallat, B. Alessandrini, and P. Ferrant. SPH simulation of green water and ship flooding scenarios. *Journal of Hydrodynamics, Ser. B*, 22(5, Supplement 1):231–236, 2010. ISSN 1001-6058.
- S. Lehner and W. Rosenthal. Investigation of Ship and Platform Accidents Due to Severe Weather Events: Results of the MAXWAVE Project. In *25th International Conference on Offshore Mechanics and Arctic Engineering*, volume 3. ASME, 2006. Hamburg, Germany.
- E. Y. M. Lo and S. Shao. Simulation of near-shore solitary wave mechanics by an incompressible SPH method. *Applied Ocean Research*, 24:275–286, 2002.
- J. J. Monaghan. Smoothed Particle Hydrodynamics. *Annu. Rev. Astron. Astrophys.*, 30:543–574, 1992.

- J. J. Monaghan. Simulating Free Surface Flows with SPH. *Journal of Computational Physics*, 110:399–406, 1994.
- J. J. Monaghan. Smoothed particle hydrodynamics. *Reports on Progress in Physics*, 68:1703–1759, 2005.
- P. Müller, C. Garrett, and A. Osborne. Rogue waves. *Oceanography*, 18(3):66, 2005.
- G. Oger, M. Doring, B. Alessandrini, and P. Ferrant. Two-dimensional SPH simulations of wedge water entries. *Journal of Computational Physics*, 213(2):803–822, 2006.
- M. Onorato, D. Proment, G. Clauss, and M. Klein. Rogue waves: From nonlinear schrödinger breather solutions to sea-keeping test. *PloS one*, 8(2):e54629, 2013a.
- M. Onorato, S. Residori, U. Bortolozzo, A. Montina, and F. Arecchi. Rogue waves and their generating mechanisms in different physical contexts. *Physics Reports*, 528(2):47–89, 2013b.
- A. R. Osborne, M. Onorato, and M. Serio. The nonlinear dynamics of rogue waves and holes in deep-water gravity wave trains. *Physics Letters A*, 275(5):386–393, 2000.
- M. H. Patel, R. Vignjevic, and J. C. Campbell. An SPH technique for evaluating the behaviour of ships in extreme ocean waves. *International Journal of Maritime Eng*, 151:39–47, 2009.
- D. H. Peregrine. Interaction of water waves and currents. *Advances in applied mechanics*, 16:9–117, 1976.
- D. H. Peregrine. Water waves, nonlinear Schrödinger equations and their solutions. *J. Austral. Math. Soc. Ser. B*, 25:16–43, 1983.
- R. Perić, N. Hoffmann, and A. Chabchoub. Initial wave breaking dynamics of peregrine-type rogue waves: A numerical and experimental study. *European Journal of Mechanics B/Fluids*, 49:71–76, 2015.
- A. Rafiee, S. Cummins, M. Rudman, and K. Thiagarajan. Comparative study on the accuracy and stability of sph schemes in simulating energetic free-surface flows. *European Journal of Mechanics-B/Fluids*, 36:1–16, 2012.
- M. Robinson. *Turbulence and Viscous Mixing using Smoothed Particle Hydrodynamics*. PhD thesis, Monash University, 2009.
- W. Rosenthal and S. Lehner. Results of the MAXWAVE project. In *Proceedings of the 14 th'Aha Huliko'a Hawaiian Winter Workshop*, pages 1–7, 2005.
- M. Rudman and P. W. Cleary. Rogue wave impact on a tension leg platform: The effect of wave incidence angle and mooring line tension. *Ocean Engineering*, 61:123–138, 2013.
- M. Rudman and P. W. Cleary. The influence of mooring system in rogue wave impact on an offshore platform. *Ocean Engineering*, 115:168–181, 2016.

- T. E. Schellin and O. El Moctar. Numerical prediction of impact-related wave loads on ships. *ASME J. Offshore Mech. Arct. Eng.*, 129:39–47, 2007.
- T. E. Schellin, M. Perić, and O. el Moctar. Wave-in-Deck Load Analysis for a Jack-Up Platform. *Journal of Offshore Mechanics and Arctic Engineering*, 133, May 2011.
- C. M. Schober. Melnikov analysis and inverse spectral analysis of rogue waves in deep water. *European Journal of Mechanics-B/Fluids*, 25(5):602–620, 2006.
- M. S. Shadloo, D. Le Touzé, G. Oger, et al. Mesh-free lagrangian modelling of fast flow dynamics. In *The Twenty-fifth International Ocean and Polar Engineering Conference*. International Society of Offshore and Polar Engineers, 2015.
- S. Shao and H. Gotoh. Turbulence particle models for tracking free surfaces. *Journal of Hydraulic Research*, 43(3):276–289, 2005.
- J. Smagorinsky. General circulation experiments with the primitive equations: I. the basic experiment\*. *Monthly weather review*, 91(3):99–164, 1963.
- S. Smith and C. Swan. Extreme two-dimensional water waves: an assessment of potential design solutions. *Ocean engineering*, 29(4):387–416, 2002.
- D. Solli, G. Herink, B. Jalali, and C. Ropers. Fluctuations and correlations in modulation instability. *Nature Photonics*, 6(7):463–468, 2012.
- A. Souto-Iglesias, L. Delorme, L. Péres-Rojas, and S. Abril-Pérez. Liquid moment amplitude assessment in sloshing type problems with smooth particle hydrodynamics. *Ocean Engineering*, 33(11–12):1462–1484, August 2006.
- I. Ten and H. Tomita. Simulation of the ocean waves and appearance of freak waves. In *Reports of RIAM Symposium*, number 17SP1-2, March 10–11 2006. Fukuoka, Japan.
- D. Violeau and R. Issa. Numerical modelling of complex turbulent free-surface flows with the sph method: an overview. *International Journal for Numerical Methods in Fluids*, 53(2): 277–304, 2007.
- H. Wendland. Piecewise polynomial, positive definite and compactly supported radial functions of minimal degree. *Advances in Computational Mathematics*, 4(1):389–396, 1995.
- B. J. West, K. A. Brueckner, R. S. Janda, D. M. Milder, and R. L. Milton. A new numerical method for surface hydrodynamics. *J. Geophys. Res.*, 92(11):803–824, 1987.
- J. Westphalen, D. M. Greaves, C. J. K. Williams, A. C. Hunt-Raby, and J. Zang. Focused waves and wave-structure interaction in a numerical wave tank. *Ocean Engineering*, 45:9–21, 2012.
- B. S. White and B. Fornberg. On the chance of freak waves at sea. *Journal of Fluid Mechanics*, 355:113–138, 1998.

- J. Wolfram, B. Linfoot, and P. Stansell. Long-and short-term extreme wave statistics in the north sea: 1994-1998. *Rogue Waves*, 2000.
- C. Yang, H. Lu, R. Löhner, X. Liang, and J. Yang. Numerical simulation of highly nonlinear wave-body interactions with experimental validation. In *Proceedings of the International Conference on Violent Flows, Fukuoka, Japan, 2007*.
- I. R. Young. *Wind Generated Ocean Waves*, volume 2. Elsevier, 1999.
- V. E. Zakharov. Stability of periodic waves of finite amplitude on the surface of a deep fluid. *Journal of Applied Mechanics and Technical Physics*, 9(2):190–194, 1968.
- X. Zhao and C. Hu. Numerical and experimental study on a 2-D floating body under extreme wave conditions. *Applied Ocean Research*, 35:1–13, 2012.
- X. Zhao, Z. Ye, Y. Fu, and F. Cao. A cip-based numerical simulation of freak wave impact on a floating body. *Ocean Engineering*, 87:50–63, 2014.